Investigation of the Performance of Microstrip Gas Detectors for X-rays and Evaluation of their Application to Mammography

Antonios Papanestis

Department of Physics and Astronomy

University College London

Submitted for the degree of

Doctor of Philosophy

July 1997

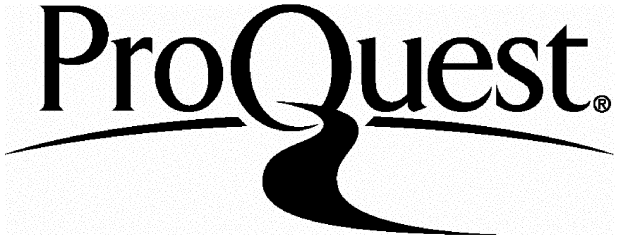

To my parents

Παυλο and Μεταξια

Acknowledgements

This thesis deals with many different concepts from Medical and Particle Physics, experiment and simulation. As a result the number of people that helped me throughout this work is large. Part of this work was sponsored by the European Atomic Energy Community.

First and foremost I would like to thank my supervisor Prof. David J. Miller for his help and support in all aspects of my work and for helping me get the EU grant.

Special thanks to Mike Esten for patiently answering all my questions on gas detectors, for giving me useful advice on both experiments and simulations and for allowing me to use the ATLAS MSGC assembly for my experiments.

Some of the experiments described in this thesis were done in Novosibirsk, Russia. Many thanks to Prof. Khabakhpashev and Lev Shekhtman for inviting me, paying for my stay and giving me the opportunity to visit Siberia. Talking to Lev considerably helped in furthering my understanding of MSGCs.

Many thanks to Robert Speller for finding the time to help with all the medical aspects of this study and to Arni Martínez and Lawrence Court, whose theses taught me so much about digital radiology.

Dominic Hayes, Brian Anderson, Mike Cresswell and Derek Attree all helped me with many aspects of the hardware during my experiments. Ron Kensek

of SANDIA Labs helped me understand the ITS code, while Gordon Crone was always there to solve software problems. Archana Sharma from CERN calculated diffusion coefficients for me. Thank you all.

I also want to thank Robert and Antonio, who were there to share problems on PAW, LaTeX or even real work during coffee, tea, lunch, beer and various other breaks. Thanks to Sanda for not interfering with my work.

Finally I would like to thank my parents and my uncle Theodore Xenos for their support. This thesis is dedicated to my parents who never complained about having to fund my studies since I was 18 and for being so understanding.

July 1997

Antonis Papanestis

PS As a final word before this thesis goes to "press" I would like to thank my examiners, Prof. R. Ott and Dr. I. Duerdoth, for the constructive suggestions on the final version of the text of this thesis.

October 1997

Antonis Papanestis

Abstract

The work presented is this thesis is an investigation of the spatial resolution of a Microstrip Gas Chamber (MSGC) as an imaging device for X-rays. Applications include digital radiology and experiments with synchrotron radiation. The investigation was done for X-ray energies around 20 keV, and the detector was evaluated for digital mammography.

Both experiments and simulations were used for the evaluation of MSGCs. A series of experiments was performed at the Budker Institute of Nuclear Physics in Novosibirsk, Russia, using a parallel strip MSGC. It was shown that MSGCs have the potential to be used as imaging devices for medical applications. A simulation model, based on the Monte-Carlo program ITS, was developed to simulate the properties of MSGCs. The results of the simulation were in good agreement with the experimental data form Novosibirsk. More experiments were performed at UCL to test the model under different conditions, and were also simulated successfully.

Having proved that the predictions of the simulation could be trusted the model was used to predict the performance of a keystone MSGC for digital mammography. The Line Spread Function (LSF) of the detector was simulated and the Modulation Transfer Function (MTF) was calculated.

Contents

List of Figures

List of Tables

Chapter 1

Introduction

Particle Physics is driven by the need of faster detectors with better resolution (both spatial and energy) to devise and develop new detector technologies. Some of these detectors find applications in other disciplines including medicine. Two examples are the scintillator-photomultiplier combination in the Anger camera, and the multiwire proportional chamber for Positron Emission Tomography.

However, this "technology transfer" is not automatic. The requirements for detector performance are usually different, and the detector needs "re-optimization" before it can be used in a different field. Also, researchers from different areas use different terms in their specifications, and communication of recent developments can be difficult.

This thesis tackles both tasks, to understand the demands of the new field and to re-optimize the technology to meet those demands. A promising detector technology, the Micro-Strip Gas Chamber (MSGC), was invented in 1987 by Oed [1]. Gas detectors, after the invention of the Multi-Wire Proportional Chamber (MWPC), had been used extensively in Particle Physics experiments, but it seemed they had reach their limits. New experiments require better accuracy in particle localisation, and the ability to perform under high particle fluxes.

Today, although research is still continuing, the technology is beginning to mature. MSGCs can be manufactured industrially in large quantities. The time to look for possible applications outside the Particle Physics community has come. Gas detectors are used to detect ionising radiation, either charged particles or photons. They have the right properties to detect X-rays so medicine is an obvious area to look for applications. There are other areas where detection of X-rays is also crucial, such as synchrotron radiation experiments. Although this work has been done mainly with Digital Radiography in mind, the results are valid for all other applications that involve detection of X-rays in the energy range up to a few tens of keV.

1.1 Digital Radiography

Digital Radiography (DR) is a growing branch of medicine. It generally deals with radiograms (pictures taken with the use of X-rays) in digital form. Traditional Radiography uses film to detect, store and display the image. DR separates these components so that each can be optimised independently. Although the separation can be accomplished by digitising film images, such an approach is time consuming and cannot produce digital images in real time. It also has the inherent limitations of film such as small dynamic range and film granularity, and the digitisation process increases the noise of the image.

Film is one of the oldest detectors ever used and has very good spatial resolution. It is very efficient when used to detect light but very inefficient for detecting X-rays. Film-screen combinations are used to improve efficiency using a high Z material, the screen, for the conversion of X-rays to visual light, which is then detected by the film. However, film/screen combinations have lower resolution because the light from the screen is emitted isotropically reducing the localization of the original X-ray photons.

The most important limitation of film is its limited dynamic range. The response of the film to radiation is expressed using the optical density D, a measure of the blackening of the film. It is defined as:

$$D = \log_{10}(I_0/I) \tag{1.1}$$

where I_0 and I are the intensities of a light beam before and after passage through the film [2].

Figure 1.1 shows a typical film response to radiation exposure X. For low exposures the film density increases very slowly and non-linearly with exposure to radiation. Very little information is recorded and the film is *under-exposed.* For high exposures the film density again increases very slowly; the film is *over-exposed* and turns completely black. The middle part of the curve is used in radiograms to maximize their diagnostic value, as the film density increases linearly with the logarithm of exposure:

$$D = a \log X + b \tag{1.2}$$

If a small change in the input signal X is considered in Equation 1.2, the change in optical density is proportional to the input contrast $(\Delta X/X)$:

$$\Delta D = 0.434a \frac{\Delta X}{X} \tag{1.3}$$

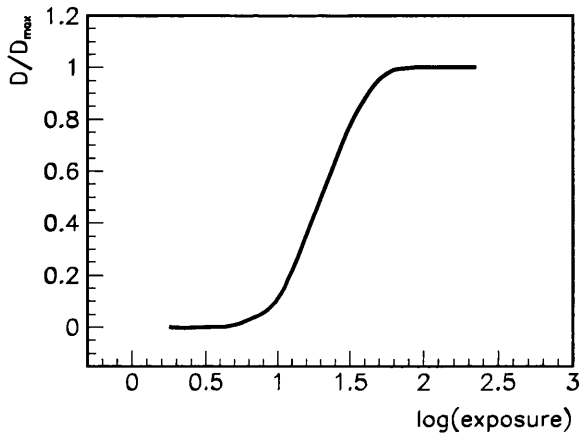

Figure 1.1: Characteristic curve of film density (blackening).

But the range of the linear response is small—less than an order of magnitude. A different film type has to be used for examinations requiring different exposures. Even if the film is exposed correctly for the particular examination, some parts of the film can be either under or over-exposed. A second exposure of the patient may be needed.

The drawbacks of film can be overcome if a digital detector is used. An ideal detector for digital radiography would have good spatial resolution (below 0.3 mm, depending on examination), wide dynamic range (of the order of 20000 photon counts), very high efficiency (if possible 100%) and high counting rate to reduce the exposure time (of the order of 1 MHz per pixel). The pixel size ideally would be 2 to 3 times smaller than the detector resolution and the size of the detector would have to match the area under examination. Good energy resolution is not very essential but it could be used for dual energy radiography.

Direct digital capture of radiographic image with such a detector offers many advantages compared with traditional radiography:

- The image is obtained on-line and displayed on a high resolution screen, without the delay of film development. It can then be printed by a high resolution laser printer, or stored.

- A detector with linear response to exposure provides information that reflects directly the absorption of X-rays. The information on the image can be processed easily since the relation between response and exposure does not change, unlike the response of film. Linear response combined with wide dynamic range means that all the available information from the exposure has been captured.

- Direct digital capture produces images without the noise added due to digitisation of film images. The contrast of the image can be manipulated to reveal details that might be invisible in a single film exposure because they

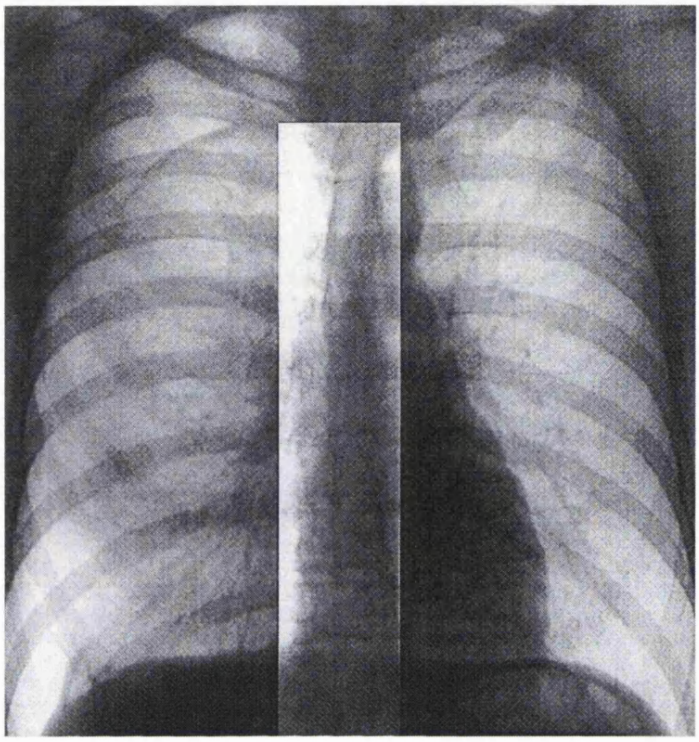

Figure 1.2: A digital image of the chest and lungs with the spinal column also visible [3].

were either over or under exposed. Moreover, windowing techniques can be used to improve the contrast only in certain areas of the image and software filtering can enhance subtle details.

Figure 1.2 is an attempt to display the advantages of Digital Radiography. A chest X-ray "sees" the spine as well as the lungs, but the different X-ray intensities are not matched to the performance of the film; lung and spine images normally require separate exposures. However with digital readout, windowing can be used to reveal separate images of the same data. In Figure 1.2 the contrast values have been changed inside the window to reveal the spine which was hidden behind the sternum. The ribs and the sternum are not visible inside the window [3].

Other advantages of digital radiography include the ability to create libraries with images which can easily be accessed through the Internet, the ability to

send multiple images by electronic file transfer to experts for evaluation, and automated diagnosis with the use of proper software algorithms.

A fully digital radiographic system, the Siberian Digital Radiographic Device (SDRD), was developed in the late 1980s at the Institute for Nuclear Physics in Novosibirsk, Russia. The MSGC system for digital mammography which will be presented in Chapter 6 below, is based on the methods and concepts used in the SDRD.

1.1.1 Siberian Digital Radiographic Device

The SDRD (Figure 1.3) [4, 5, 6] consists of a tungsten target X-ray tube, a pair of slit collimators (one before and one after the patient), a mechanical scanning

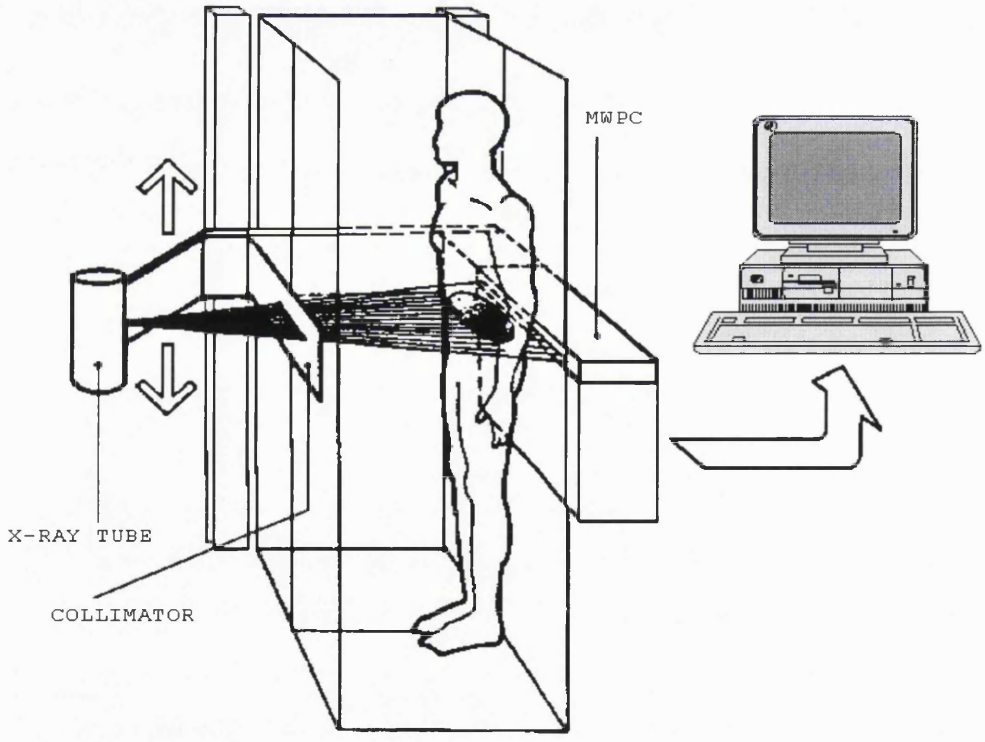

Figure 1.3: Schematic layout of the SDRD.

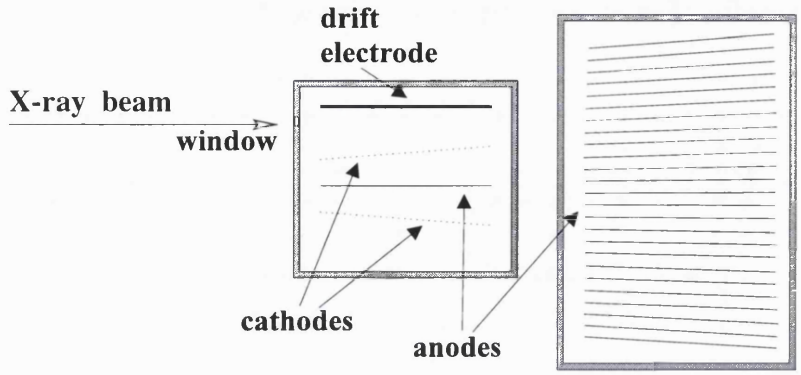

Figure 1.4: Diagram of the MWPC (not to scale). A side view can be seen on the left and a top view on the right.

system, an MWPC and the associated control and read out electronics. The first collimator between the tube and the patient forms a 1 mm thick and 40 cm wide fan-shaped beam. A second collimator between the patient and the detector suppresses scattered photons. The tube, collimators and detector are mounted on a rigid gantry which can move in the vertical direction. Every anode wire is connected to a discriminator giving a logical pulse for every photon that converts in the gas close to the wire. CAMAC scalers, connected to the discriminators, count the pulses and produce a horizontal line with information on the spatial distribution of X-ray photons. The gantry is then moved in a vertical direction producing a two dimensional image from a series of lines. This is achieved by scanning the patient at a constant speed and adding the number of hits of each wire for the time period required to produce a line. The number of hits is then stored in memory, the scalers are reset and the acquisition of the next line begins.

The MWPC was specially designed for the SDRD. The anode plane consists of 320 wires, 1.2 mm apart, all pointing towards the focal spot of the X-ray tube at a distance of 1.35 m (Figure 1.4). The fan-shaped anode plane provides sufficient absorption depth without introducing a parallax error, the error associated with particle localization when the beam crosses the detector at an angle. If parallel anodes were used photons passing through the same spot in the patient could

be registered at different positions if they converted at different depths in the detector. A plane of cathode wires is arranged so as to keep the gain of the chamber constant along the anodes, and a separate electrode creates the drift field. The chamber is filled with a Xe/CO_2 mixture, 80/20, at 3 bar.

The discriminators connected to every anode wire generate a logic pulse if the pulse from the wire corresponds to a deposited energy above $\sim$ 2 keV. Charge sharing between the wires often results in a double hit; a single X-ray photon detected by two neighbouring wires. The device can operate in two modes depending on the handling of double hits:

Standard (ST) mode Double hits are rejected using coincidence logic (Figure 1.5a) to improve the spatial resolution. The pixel size in the horizontal direction at the patient, defined by the spacing of the anode wires is 1 mm. The vertical pixel size is set by the integrating time of the scan line. For 1 mm a new scan line is produced every 30 ms and a 1 mm rear collimator is used. The maximum number of lines is 256.

High Resolution (HR) mode Double hits are registered in separate channels. This doubles the number of horizontal channels and improves the resolution even further. The horizontal pixel size is 0.5 mm and the vertical pixel size is set to the same value by using 15 ms integration time for a scan line and a 0.5 mm rear collimator. The maximum number of lines is 512.

All stages of the process are controlled from a PC. Images can be displayed on the computer screen, printed, and/or stored on hard disc. The quantum efficiency of the system is about 30% for 60 keV photons.

The ratio of hits between the coincidence and anti-coincidence channels depends both on the gain of the chamber and on the energy of the X-rays. This creates a problem because the gain of the chamber changes with the count rate

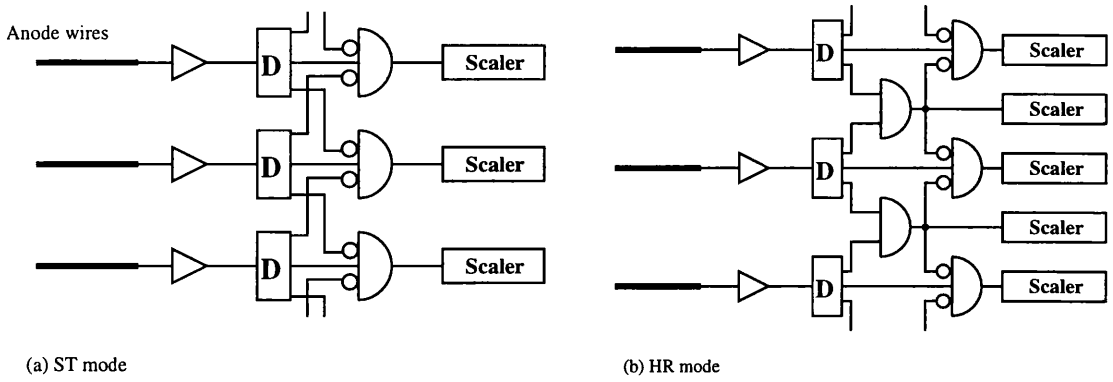

Figure 1.5: Coincidence logic used (a) to reject double hits and (b) to register double hits on separate channels.

due to space charge effects (see section 3.1.2). A normalising algorithm is used to correct for this effect using data from uniform chamber irradiation at different counting rates.

Tests performed by Martínez et al. [7] in 1993 showed that the system could achieve significant dose reductions compared with film/screen systems. Dose reductions varied from 30 to 300 times depending on the clinical examination involved. Its other advantages over film/screen were the linear response over a wide range, without the non-linearities of the film for very low exposures, and the very good signal to noise ratio. The standard deviation of pixel counts for uniform irradiation in the ST mode scaled with $\sqrt{N}$, where N is the average number of counts. This is the quantum limit set by the random nature of photon detection. In the HR mode the standard deviation scaled with N; the image was noisier. The extra noise was introduced by the necessary renormalization of the double hits. The most serious disadvantage of the system was its limited spatial resolution of 0.5 mm. The system is being used for routine clinical examinations in hospitals in Novosibirsk and Moscow.

The only way to increase the resolution of the system in the horizontal direction is to decrease the spacing of the anode wires. However, mainly due to electrostatic forces between the wires, the operation of MWPCs with wire spacing

below 1 mm is not stable. The replacement of the MWPC with an MSGC seemed natural since the motivation behind the invention of the MSGC was exactly this problem. With a typical anode spacing of 200 μm the MSGC offers resolution comparable with that of film.

The area of radiography that images the female breast, mammography, seems well suited for a device based on an MSGC:

- The imaged area is small, about 15×15 cm^2 and microstrip tiles of this size are now available. Also, the required number of channels to cover this area (15 cm/0.02 cm = 750 or 1500 in HR mode) is not exceedingly large.
- The photon energy used in mammography is about 20 keV, lower than for the rest of the body. This is because the breast tissue is not very dense and low energy X-rays give better contrast. Lower energy photons give better resolution in an MSGC because they produce lower energy photoelectrons. Since the range of electrons is reduced at higher gas pressures, for lower energy X-rays lower pressure is needed to achieve the necessary resolution.

1.2 Digital Mammography

Breast cancer is a very frequent cause of death for women, and studies in the population have shown that the mortality rate can be reduced by the screening of women between the ages of 50 and 64. By screening we mean X-ray examinations of the female breast at regular time intervals (3 years) that will help find signs of cancer when it is at its very early stages. One of the main indicators of breast cancer is the appearance of microcalcifications, a situation where local tissue is replaced by hydroxy-apatite ($Ca_5[PO_4]_3OH$) [8]. These calcifications can be very small so the imaging system must have very good spatial resolution in order to detect them.

A special type of film/screen, with a single screen placed behind the film, is used for conventional mammography in order to achieve good resolution. The resolution of this combination is below 100 μm and the efficiency around 75%. The limit in the size of calcifications that can be detected with this combination is 100–200 μm.

The first systems for digital mammography have appeared only recently and are still being tested in clinical trials. Most of the research is done with semiconductor detectors that use CCD technology. A scintillator screen is used to convert X-rays to photons in the optical part of the spectrum because the absorption coefficient of silicon for X-rays is small.

The requirements for pixel size have not been set yet. H.P. Chan argues that pixel size at least as small as 35 μm is necessary for computer detection of subtle microcalcifications [9]. M. Freedman claims that there is minimal advantage using 50 μm pixels rather than 100 μm pixels, on the basis that smaller calcifications are very difficult to detect due to their reduced contrast, and smaller pixels require greater patient dose for the same statistics [10]. Karssemeijer et al. have shown that digitising film to 100 μm pixels did not reduce the detectability of small calcifications [11].

There are certain other constraints that a system for mammography has to meet besides spatial resolution. Patient dose and time to acquire the radiogram are the most important. The time limit is imposed because the breast is compressed during the examination and the compression can be very painful. The time needed for a conventional examination is about 2 s and a system needing more than 10 s for a mammogram would be unacceptable. The current dose limit and typical dose per examination is 2 mGy glandular dose. The Gy is defined as absorbed energy per kilogram of mass (1 Gy = 1 J/1 Kg).

A typical X-ray tube for mammography operating at 30 kV provides an X-ray flux of 4.67×10^5 photons $\mathrm{mA^{-1}s^{-1}mm^{-2}}$ at 75 cm [12]. In a typical examination

the tube is used at 30–35 kV, and 100–150 mAs. Assuming a 4 cm thick breast, which absorbs ~93% of the radiation, for each 100×100 μm^2 pixel at 45 cm there are about 100,000 available photons. The SDRD produced quality images with less than 10,000 counts per pixel. So a similar system for mammography could produce images with 10 times less dose than conventional systems.

1.2.1 An MSGC for digital mammography

There are certain advantages in the use of an MSGC as a detector for digital mammography compared to CCDs:

1. An MSGC counts individual photons. There are no other sources of noise but the intrinsic randomness of photon detection, so the quantum limit can be reached. CCDs work by collecting charge produced by ionizing radiation in a potential well over a period of time. However, small quantities of charge, the dark current, are released even without exposure to ionizing radiation, so there is an uncertainty in the energy deposited in the detector and the number of absorbed photons. This uncertainty introduces noise in the images.

2. The absorption coefficient of silicon for photon energies around 20 keV, combined with a typical thickness of 200–300 μm, limits the quantum efficiency of a CCD to below 30%. Coatings, used to improve the quantum efficiency by converting X-rays to light, degrade the performance of the detector because light is emitted isotropically. An MSGC filled with xenon at 5 bar can easily be made long enough to absorb all the incoming photons (97% if 5 cm long). The factors that limit the quantum efficiency of such a device are thickness and material of entry window and possible inactive gas volume. An entry window made from 1 mm thick beryllium absorbs only about 5% of photons around 20 keV, but 0.5 cm of inactive xenon at

5 bar absorbs 30% of the photons. The actual efficiency of the system will depend on the design of the chamber, but a quantum efficiency above 50% is possible.

Both characteristics, the high signal to noise ratio and the very good quantum efficiency, can lead to a device that offers significant dose reductions for the patient. This is a big advantage for a device used in a screening programme since it involves large numbers of people and the integrated dose to the population is high.

Another application in which dose reduction could be of great importance is the imaging of small areas of the breast for the localisation of a needle during biopsies. The image can be acquired instantly and with a very small dose because the needle offers high contrast. The studies of the SDRD showed that high contrast objects can be imaged with a dose reduction of almost 300.

A system based on a CCD can, in principle, offer better spatial resolution than a system based on an MSGC since CCD pixels can be very small (below 30μm). However, in medical applications it is the diagnostic value of the images that is important, and a system with higher spatial resolution does not necessary offer higher diagnostic value. Smaller pixels require higher exposure to reach the necessary pixel counts for good image quality, hence higher dose for the patient, especially if details comparable to the pixel size are to be detected. A system based on an MSGC with lower resolution and lower noise levels could offer images with the same diagnostic value as that from a CCD system using lower exposures.

Two geometries

Two possible arrangements of an MSGC detector have been considered for X-ray detection: the "perpendicular" and the "tangential" shown in Figure 1.6.

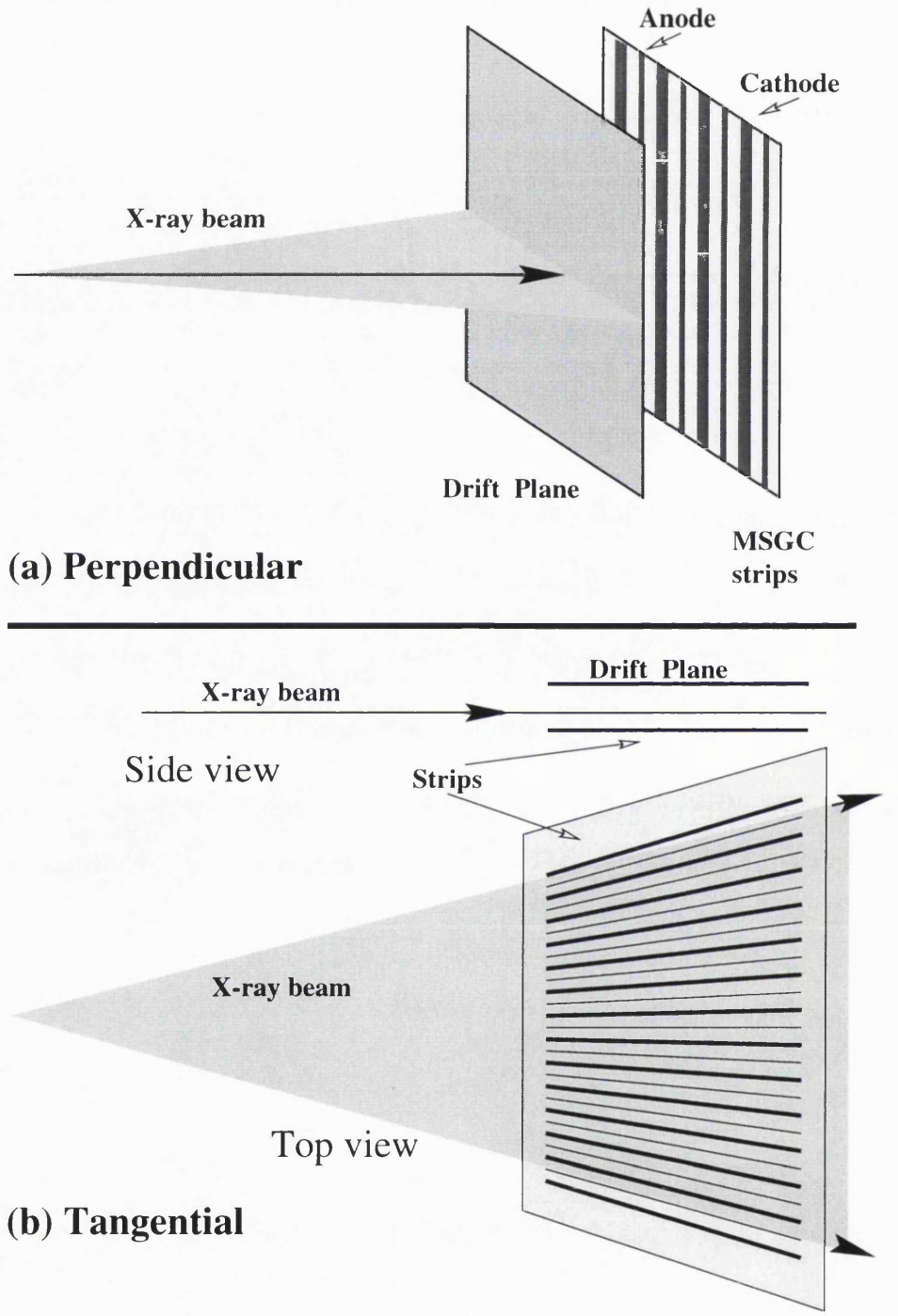

Figure 1.6: Two geometrical configurations for X-ray detection with MSGCs. The "perpendicular" geometry was used in the first series of experiments, while for a device for X-ray imaging the "tangential" geometry with a keystone tile may be more suitable.

In the "perpendicular" geometry an MSGC with parallel strips is placed with the strip plane perpendicular to the incident X-ray beam. Although this geometry is very simple, it poses certain problems. The quantum efficiency of the detector depends on how thick the drift gap is. At least 1 cm of xenon at 5 bar is necessary for efficiency above 50%. But a thick drift gap allows the electrons to diffuse significantly even if a low diffusion gas mixture is used. The diffusion coefficient of Xe/CO_2 (80/20) is about 200 μm for 1 cm of drift which degrades the resolution of the detector. With 0.5 cm drift gap the quantum efficiency limit is 30% if the gas mixture is at 5 bar.

Parallax error is also introduced because the X-ray beam enters the detector at an angle that is 90° only in the centre and can be up to 8° off the perpendicular direction at the edges. Two photons following the same path and entering the detector at 6° of the perpendicular will be registered 0.5 mm from each other if the difference in depth of their conversion points is 5 mm. Although this geometry is not very promising, microstrip tiles with parallel strips are more suitable for preliminary experiments because of their simpler geometry, readily available and cheaper since large number of tiles have been manufactured. The first series of experiments at Novosibirsk, reported in Chapter 5, were done with this geometry.

The "tangential" geometry is the same as that of the SDRD. The strips of the detector, no longer parallel, point at the X-ray source in a fan-shaped arrangement. The X-ray beam is parallel to the strip plane. There is no parallax error in this geometry and the active depth of the detector can easily be made long enough so that almost all X-ray photons are absorbed. However, this geometrical arrangement may introduce inactive gas volume in the beam entrance and reduce the detector efficiency. The effects of diffusion are minimised because the beam enters the detector very close (0.5–2 mm) to the microstrip tile. The proximity of the beam to the anodes is limited only by the mechanical construction, as the chamber is under high pressure. Special studies of different cathode configurations have proven that the gain of the chamber along the strips is uniform

(variations less than 4%) in spite of the varying anode pitch. Tiles of this geometry were not available during the first series of experiments, but the Novosibirsk group are preparing experiments with keystone tiles, and such tiles are being used in the CMS experiment at the CERN LHC.

Chapter 2

Elements of X-ray Physics

X-rays were discovered by Röntgen in 1895 and have played a major role in medical examinations from the beginning of the century. A description of the mechanisms of the absorption of X-rays is essential for understanding the operation of detectors.

2.1 X-ray Production

X-rays are conventionally taken to be photons in the energy region of 100 eV to 150 keV. Two sources of X-rays are used in this work: radio-isotopes and X-ray tubes. Synchrotron radiation is outside the scope of this thesis.

2.1.1 Radio-isotopes

Radio-isotopes are a very common source of radiation. They have the advantage that they work simply by existing. Photons from nuclear or atomic electron transitions are commonly found in the decay products of nuclei. Originally photons generated in nuclear transitions were called γ-rays, and photons generated

by electron transitions were called X-rays. Unfortunately the range of energies overlap and in this thesis the term X-rays is used to refer to any photons between 100 eV and 150 keV.

Electron capture is a decay mode where the nucleus captures one of the orbiting electrons which then interacts with a proton to produce a neutron and a neutrino. In this case atomic X-rays and/or nuclear γ-rays may be emitted without being accompanied by other decay products. Elements that decay via electron capture are very useful because they provide pure photon sources. A good example is ^{57}Co which decays to ^{57}Fe by electron capture. ^{57}Fe is created with an excess of energy of 136 keV and in 10% of cases emits a photon with that energy. In the remaining 90% of cases it decays to its first excited state which is 14.4 keV above ground and emits an 126 keV photon, followed by a 14.4 keV photon [13].

It is also possible that after electron capture the daughter atom will rearrange its electrons and will emit the characteristic X-rays for this element. ^{55}Fe, the most commonly used source in gas detector testing, is a good example of this. ^{55}Fe decays via electron capture to ^{55}Mn, emitting a 5.9 keV X-ray, the characteristic K line of Manganese. The ^{109}Cd source used in the experiments in Novosibirsk decays via electron capture to ^{109}Ag which has a double X-ray line at 21.9 and 22.1 keV.

2.1.2 X-ray Tubes

Radio-isotopes have the advantage of emitting X-rays of specific energy, but using them to generate the high photon fluxes necessary for medical examinations is hazardous and expensive. Present-day X-ray tubes, far more sophisticated than the cathode-ray tube Röntgen was using when he discovered X-rays, but based on the same principles, generate X-rays by allowing energetic electrons to hit a

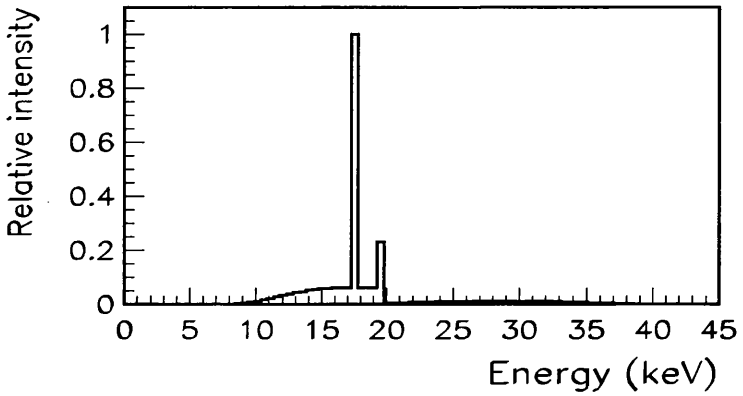

Figure 2.1: Typical X-ray spectrum produced by a tube with a molybdenum target at 40 kV and filtered with 1 mm of beryllium and 0.03 mm of molybdenum.

metal target. Electrons are produced at the cathode from a filament by thermal emission. They are then accelerated to the target (anode) by a potential difference of tens of thousands of volts. When they hit the target they emit bremsstrahlung radiation with a continuous spectrum. An example of such a spectrum can be seen in Figure 5.3. If the energy of the electrons is higher than the binding energy of the K shell of the target material, they can ionize the target atoms by kicking out electrons from the K shell. In that case electrons from the other shells fill the gap and emit the characteristic K lines for that material. The most probable transition is from the L to the K shell and is called the K_α line, while the transition from the M to the K shell produces a higher energy line called the K_β line. The spectrum of a tube with molybdenum target (used for mammography) with characteristic K_α and K_β lines at 17.4 and 19.5 keV, operated at 40 kV is shown in Figure 2.1 [12].

2.2 X-ray Absorption

The understanding of the interactions of X-rays with matter is very important in the building of a detector for X-rays. Only after considering all the possible ways that X-rays interact with matter and after understanding the processes that

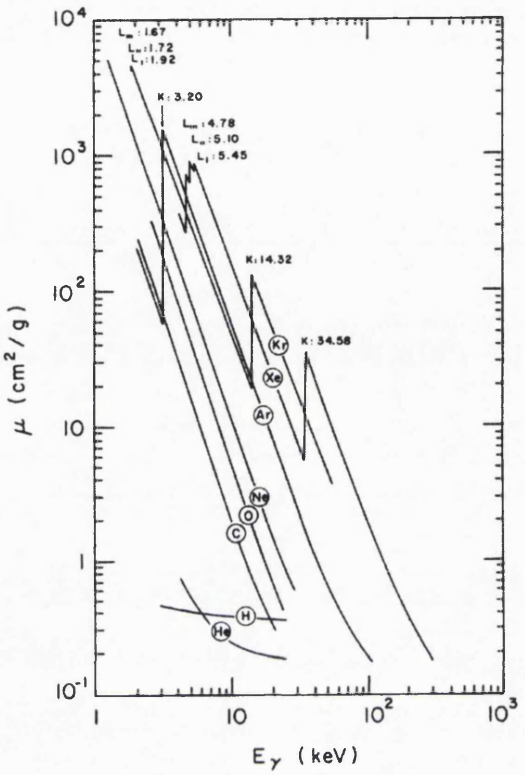

Figure 2.2: X-ray absorption coefficient versus energy of X-rays in several gases used in gas detectors.

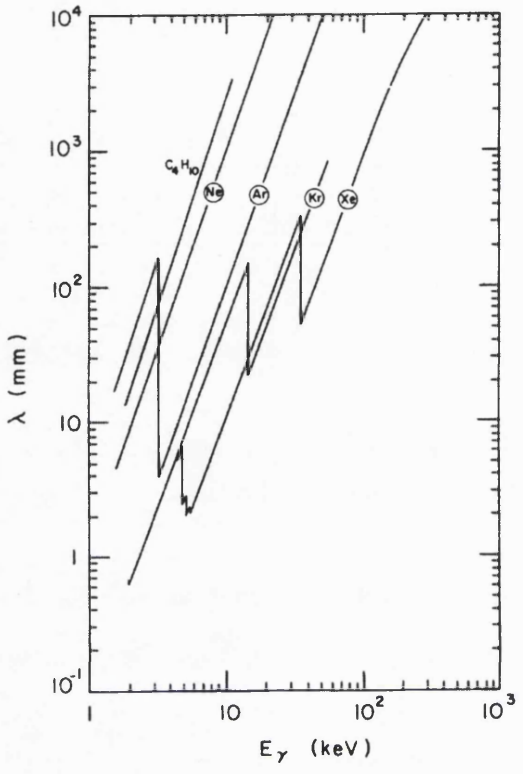

Figure 2.3: Mean free path for absorption in several gases at normal conditions.

follow the interactions, can the performance of a detector be optimized.

When an X-ray beam of intensity I traverses a thin layer of matter of thickness dx its intensity will decrease by:

$$-dI = \mu I dx \tag{2.1}$$

where μ is the *absorption coefficient.* Integrating equation 2.1 we get:

$$I = I_0 e^{-\mu x} \tag{2.2}$$

where I_0 is the initial beam intensity and I is the intensity of the beam after traversing material of thickness x. If the thickness x is equal to $1/\mu$ the beam intensity will decrease to I_0/e. This thickness is called the mean free path for

absorption. The absorption coefficient μ for the gases most commonly used in detectors is given in Figure 2.2 in cm^2/g. It must be multiplied by the density of the material to be converted to inverse length. Notice that the absorption coefficient increases dramatically when the photon energy increases above the edge of a shell. The mean free path for absorption is given in Figure 2.3. Both figures were taken from reference [14].

X-rays interact with matter in three ways: the photoelectric effect, Compton scattering and, if their energy is above 1 MeV, pair production. In the energy region that is of interest in medical applications (10–100 keV), the photoelectric effect is the dominant process of photon interaction in tissue.

2.2.1 The Photoelectric Effect

Photoelectric absorption is a quantum process involving a transition from the lower lying electron shells to the free continuum [13, 14]. Denoting by E_j the binding energy of a shell j, photo-ionization in the shell can take place only for photon energies $E_\gamma \geq E_j$ and, at a given energy, the contributions of all shells having $E_j < E_\gamma$ add up. Absorption of a photon of energy E_γ in a shell of energy E_j results in the emission of a photoelectron of energy $E_e = E_\gamma - E_j$. Table 2.1 shows the density and the binding energy of the K and L shells of various gases [15]. There are three sub-shells with slightly different binding energies in the L shell so the numbers given are the averages of their binding energies. It is easy to see that for photon energies around 20 keV only L shell ionization is possible in xenon.

After the emission of the photoelectron the excited ion can then return to its ground state mainly through two competing mechanisms:

- Fluorescence, i.e. the transition of an electron from an energy shell $E_i < E_j$ into the j shell, with the emission of a photon of energy $E_j - E_i$;

- Radiationless transition, or Auger effect, which is an internal rearrangement involving several electrons from the lower energy shells, with the emission of an electron of energy very close to E_j.

The binding energy of the i shell is usually small compared to the binding energy of the j shell so the energy of the photon is just below E_j where the cross section is at a local minimum. This means that thin materials tend to be transparent to their own characteristic X-rays. The effect is pronounced at the K edge where the difference in the cross section before and after the K shell binding energy is the largest. This has an application in the filtering of X-rays. If a broad spectrum of X-rays passes through a thin layer of some material the energies absorbed least are the energies just below the K edge. Higher energy photons can also ionize the material and cause the emission of characteristic photons also just below the K edge. If the filter is close to the X-ray source, these extra characteristic photons will also be added to the apparent outgoing flux, giving an extra enhancement below the K edge energy.

The fraction of de-excitations resulting in fluorescence is called the fluorescence yield. For the K shell the fluorescence yield increases with the atomic number. For argon the fluorescence yield is about 0.1 and for xenon about 0.75

Table 2.1: Density, binding energy of the K and L shells, average energy for the creation of an electron-ion pair (W) and the Fano factor in several gases commonly used in gas detectors, in normal conditions.

Element	Xe	Kr	Ar	Ne	He
Density (g/cm^3)	5.9	3.7	1.8	0.90	0.18
K shell (keV)	34.5	14.3	3.2	0.87	0.024
L shell (keV)	~5	~1.7	~0.3	~0.03	
W value (eV)	22	24	26	36	41
Fano factor	0.17		0.2	0.17	

[16]. For xenon L shell ionization the ITS simulation program used in this work gave a fluorescence yield of about 0.1.

2.2.2 Range of Low Energy Electrons

The electron emitted after a photoelectric ionization process and the Auger electron that might follow are the particles that ionize the gas by transferring part of their energy to atomic electrons. The range of these electrons determines the size of the ionization cluster and in most cases the performance of the detector.

Electrons are much lighter than atomic nuclei so they can scatter through large angles after a collision. As a result, although the total length of their path can be calculated using the Bethe-Bloch formula [17] this information is of little use since their range is much smaller. The *practical range* R is defined as the distance between the point of the creation of the electron and the point farthest away (Figure 2.4).

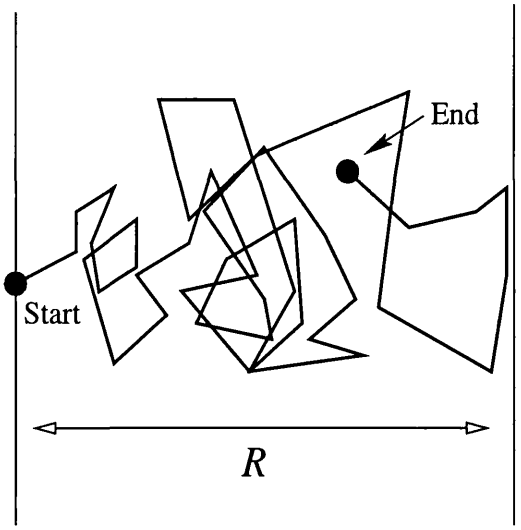

Figure 2.4: The definition of the practical range R for electrons is the distance between their creation point and the point of their path that is the furthest away.

Kobetich and Katz [18] modified the constants of the formula for the calculation of the electron practical range, originally developed by Weber [19], to fit ranges of electrons with energies from 0.3 keV to 20 MeV:

$$R = aE[1 - b/(1 + cE)] \tag{2.3}$$

where E is in keV, R in cm/gr^2 and $a = 5.37 \times 10^{-4}$, $b = 0.9815$ and $c = 3.123 \times 10^{-3}$ (dashed line in Figure 2.5). Sauli in his report on gas detectors [14]

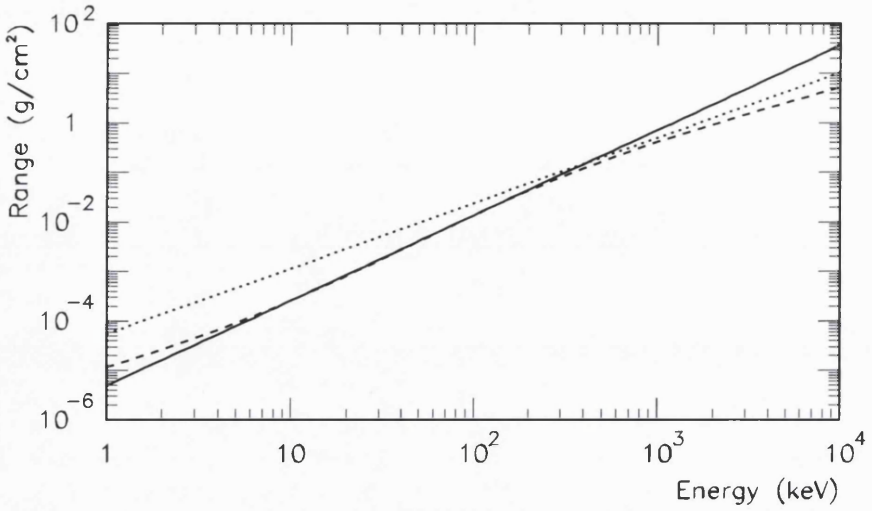

Figure 2.5: Curves indicating the practical range of low energy electrons. The dashed line is plotted using Equation 2.3, the solid line using Equation 2.4 and the dotted line using Equation 2.5.

uses the formula:

$$R = 0.71\, E^{1.72} \tag{2.4}$$

where E is in MeV. It is a very good approximation of Equation 2.3 in the range of a few to a few hundred keV (solid line, Figure 2.5). The formula:

$$R = \lambda\, E^{1.32} \tag{2.5}$$

reported by Haffner [20], with λ in the range 0.3–0.6 (here plotted for $\lambda = 0.5$, dotted line of Figure 2.5) is a better approximation of the practical range of electrons with energies from 0.5 to 10 MeV.

Using Formula 2.4 the range of a photoelectron with energy 2.6 keV, emitted after the absorption of an X-ray photon from an ^{55}Fe source in argon ($5.9 - 3.2 = 2.6$ keV), is 145 μm at 1 bar. For an 18 keV photon absorbed in xenon the energy of the photoelectron is $18 - 5 = 13$ keV and the range 690 μm for xenon at 1 bar and 140 μm for xenon at 5 bar.

Sometimes the energy transfer of the photoelectron to the atomic electrons is much higher than the ionization potential. These electrons can also ionize the

gas and move away from the interaction point, contributing to the size of the ionization cluster. They are called knock-on electrons or δ-rays and must also be taken into consideration.

2.2.3 Number of Electron-Ion Pairs—Fano Factor

Unless a fluorescence photon escapes the detector after a photoelectric absorption, all the energy carried by the incoming photon is deposited in the detector. If all of the energy was spent ionising the gas, the number of electron-ion pairs created should be equal to the incoming photon energy divided by the ionization potential. However, a considerable amount of energy is spent in non-ionising processes like excitation. So the average energy needed for the creation of an electron-ion pair W is higher than the ionization potential. It was also found that the W value depends very little on the energy deposited in the detector and it can be used to calculate the average number of electron-ion pairs created. Some values of the average energy for the creation of an electron-ion pair are given in Table 2.1 [14].

The number of electron-ion pairs created after each interaction fluctuates, and the standard deviation of the number of pairs created is given by:

$$\sigma_n = \sqrt{Fn} \tag{2.6}$$

where F is known as the Fano factor [21] and n is the total number of pairs.

The reasons for the fluctuations are due to:

1. The different modes in which energy may be absorbed. Energy can be absorbed exciting atoms and molecules as well as ionizing them, so the fraction available for ionization may vary.

2. Electrons can absorb only amounts of energy above the ionization potential of the atom. An electron given energy equal to 1.8 times the ionization potential cannot use the excess of energy to further ionize the gas.

A complete treatment of the Fano factor is given by van Roosbroeck in [22]. Values of the Fano factor for noble gases are given in Table 2.1.

Chapter 3

Principles of Operation of MSGCs

There is a wide variety of gaseous detectors offering both energy resolution and radiation position localization with applications in many fields of experimental physics. A brief introduction of their operation is given in this chapter starting from the Proportional Chamber and finishing with the Gas Microstrip Counter.

3.1 The Proportional Counter

When a charged particle, or a photon, passes through (or stops in) a volume of gas, some of its energy is dissipated ionizing the gas. The detection of the ionization is the basic principle for all gas detectors.

The electrons and ions created from the ionizing particle tend to recombine to form neutral atoms. But if a uniform electric field is applied across the gas volume electrons will drift towards the anode and ions towards the cathode. Assuming that there is some capacitance between the electrodes and that the RC time

constant of the system is much higher than the collection time, electrons and ions on their arrival at the electrodes will generate a signal:

$$V = \frac{ne}{C} \tag{3.1}$$

where n is the number of electron-ion pairs and C the capacitance of the detector [14]. For a typical capacitance of 10 μF and a few hundred pairs (typical ionization of single particles) the signal voltage is in the region of pV. For comparison, the noise at the input of a typical FET operational amplifier with 1 MHz bandwidth is about 5-10 μV [23], so the signal will be lost in the noise. (If large fluxes of particles are available then the integrated signal can be high enough for detection. This integrating type of detector is called an *ionization chamber* and is frequently used to measure doses for medical applications.)

The signal is increased if a higher electric field is applied. Electrons, which have a higher mobility than ions, can acquire enough energy between collisions to ionize the gas further in what is called *avalanche* multiplication. An electron hits an atom and ionizes it, extracting another electron so there are two free electrons, each one generating another free electron in the next step. The number of electrons doubles in every step and their final number depends on the number of steps before they are collected at the anode.

A coaxial cylindrical geometry is commonly used to create the electric field. A thin metal wire (diameter 20–40 μm) is stretched on the axis of a conducting cylindrical tube and a potential difference is applied between the electrodes. The polarity is chosen so that the wire is positive with respect to the cylindrical tube. If α is the wire diameter and β the tube diameter the electric field and the potential are given by:

$$E(r) = \frac{CV_0}{2\pi\epsilon_0}\frac{1}{r} \tag{3.2}$$

$$V(r) = \frac{CV_0}{2\pi\epsilon_0}\ln\frac{r}{\alpha} \tag{3.3}$$

where $C = \frac{2\pi\epsilon_0}{\ln(\beta/\alpha)}$ is the capacitance per unit length of the system, $V_0 = V(\beta)$ the over-all potential difference, $V(\alpha) = 0$ and ϵ_0 the dielectric constant (for gases

$\epsilon_0 \simeq 8.85$ pF/m). The minimum value for r is α and if the wire diameter is small the electric field can reach values of 70–80 kV/cm close to the anode [14].

Electrons liberated in the gas volume drift towards the anode and ions towards the cathode. Only very close to the anode, typically a few wire radii, does the field get strong enough so that multiplication starts, and every electron produces approximately the same number of final electrons independent of its original creation point—the total number of electrons follows the Polya distribution, see section 3.3.2. The total signal (sum of all avalanches) has an even narrower distribution (divided by a factor equal to the square root of the number of primary electrons) and depends only on the number of primary electron-ion pairs created,

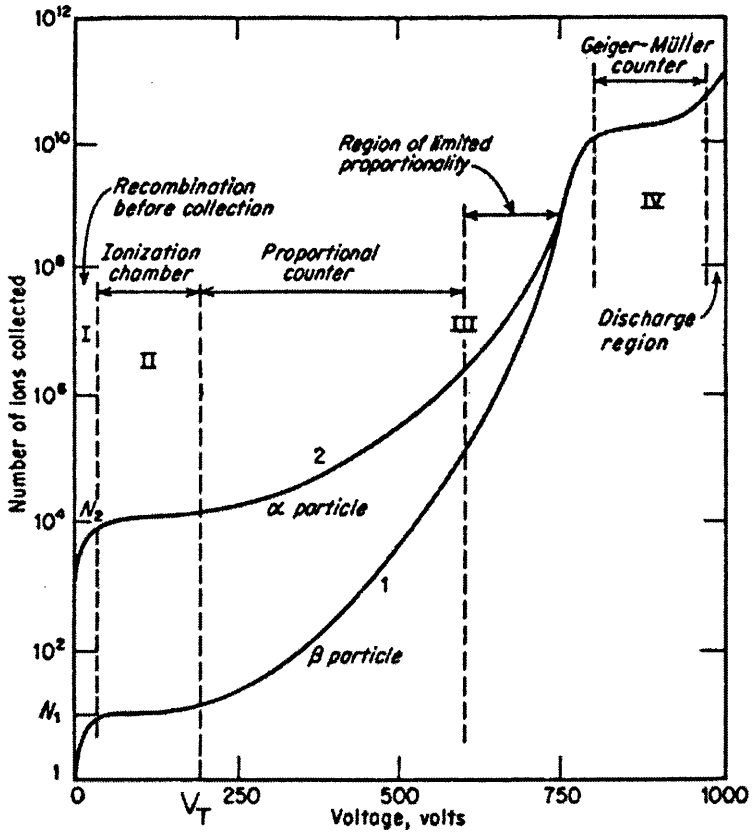

Figure 3.1: Gain-Voltage characteristic curve for a proportional counter showing different modes of operation [24].

which reflects the energy deposit. This detector is called the *proportional counter.* The gain of the proportional counter is the ratio of the number of collected ions to the number of primary ions.

Figure 3.1 shows how the number of detected ions in a proportional counter depends on the operational voltage V_0. For very low voltages some ions are collected but the main process is recombination, As the voltage increases full ion collection begins and the chamber operates in ionization chamber mode. At a threshold voltage V_T multiplication starts and gains in excess of 10^4 can be obtained still in the proportional mode. At higher voltages the proportionality is gradually lost because the space charge of the avalanche limits the multiplication. This is the limited streamer mode. Then when even higher fields are applied the avalanche is no longer localised but stretches out to a significant fraction of the wire length. Geiger-Müller mode starts at even higher voltages with every event resulting in the same saturated signal with the avalanche stretching out to cover the whole wire length.

3.1.1 Gas Properties

In principle avalanche multiplication can happen to all gases or gas mixtures, so any gas would be suitable for filling a detector. However, various aspects of the operation, particularly stable operation at high gains and long lifetime make some gas mixtures more suitable than others.

Ionization occurs more easily in noble gases than in gases with complex molecules, because there are no rotational and vibrational states to absorb the deposited energy. Avalanche multiplication also occurs more easily in noble gases because of the "Ramsauer effect" [17]. The wavelength of electrons in the range of kinetic energies around 1 eV corresponds to two diameters of bound electron orbits in noble gases. This, via a quantum-mechanical effect reduces significantly

the collision cross section, and electrons can easily acquire enough energy between collisions to create an avalanche. As a result lower fields and lower voltages are necessary for the operation of a detector that uses a noble gas.

However, a chamber filled with a pure noble gas cannot reach gains higher than 10^3-10^4 without entering a permanent discharge state. This is because during the avalanche process atoms are excited as well as ionized, and return to the ground state through radiative processes, which might include a significant amount of UV photons (the minimum energy of the emitted photon for argon is 11.6 eV). If these UV photons are absorbed by the cathode, they can extract electrons (the ionization potential of copper is 7.7 eV) which can then initiate a new avalanche soon after the primary. Ions, neutralized at the cathode, also emit photons that can also extract electrons from the cathode and start a new avalanche.

Adding small quantities of a polyatomic (usually organic) gas to the mixture can improve the performance of the detector by stopping the UV photons from reaching the cathode. This effect is called *quenching* and the gas a *quencher.* Polyatomic gases can absorb photons over a wide energy range because they have a large number of non-radiative states; methane absorbs photons very effectively in the range 7.9–14.5 keV, which covers the energy range of photons emitted by argon. The molecules then can dissipate the energy either by inelastic collisions or by dissociation into simpler radicals. Adding a polyatomic gas also reduces the number of UV photons emitted from the cathode during neutralization. As the noble gas ions drift towards the cathode, they collide with the quencher molecules and capture one of their electrons. This *ion exchange* occurs because most complex molecules have a lower ionization potential than noble gases. Very quickly almost all of the ions belong to the gas with the lower ionization potential and very few noble gas ions reach the cathode to emit UV photons.

Although organic gases are very good quenchers, allowing stable operation at gains of 10^5–10^6, they introduce problems in the long-term operation of the

chamber. When the quencher molecules are neutralized at the cathode, they either break down to simpler molecules or polymerize. The products of polymerization are deposited at the cathode and create problems in the operation of the detector. So the quencher gas must be chosen carefully. It is sometimes useful to add a third component to the gas mixture with an even smaller ionization potential than the primary quencher, which does not tend to form polymer coating (ethanol, methanol or H_2O to name a few).

3.1.2 Rate Capability—Space Charge Effects

The performance of the proportional counter is affected by the rate of particles interacting in the detector volume. The positively charged ions generated in the avalanche modify the electric field around the wire, which is restored only when all the ions are collected at the cathode (after several hundred μs). For low particle rates (up to $10^3/mm^2/s$) the gain of the chamber is not affected because the avalanche in the proportional mode does not extend more than 0.5 mm along the wire, leaving the rest of the wire active. However, as the rate of particles increases, there is not enough time for the ions to reach the cathode between events, and *space charge* builds up. The ions in the space between the anode and cathode reduce the electric field, and the gain of the chamber decreases, reducing the efficiency of the detector.

3.2 From MWPCs to MSGCs

Proportional counters are widely used wherever the the measurement of energy loss is required, but their capability in space localization is limited; a particle has either entered the detector of not. Stacking many small counters together is possible but mechanically difficult. It was Charpak who solved the problem

in 1968 with the invention of the MultiWire Proportional Chamber MWPC [25]. An MWPC consists of a series of parallel wires stretched between two cathodes. The electric field (shown in Figure 3.3) is uniform except very close to the anode wires, where it takes the $1/r$ form. Electrons liberated in the gas from a passing particle drift in a uniform field until they reach very close to an anode wire where they start avalanche multiplication as described for the proportional counter. The difference is that the signal is highest on the wire that the particle passed closest to, so the position of the particle is known (in one dimension). A second chamber with a second set of wires perpendicular to the first, or segmented cathodes on a single chamber, can provide information about the second dimension.

The spatial resolution (FWHM) of the chamber in the direction perpendicular to the wires, if it is operated with simple discrimination, is the distance between the anode wires (typically 2 mm). The resolution can be improved by using the signal from a number of cathode segments and using the centroid to locate the particle. A resolution of about 400 μm has been achieved with this method.

The centroid method is slow and has to be done off line. For fast, on line read-out systems, threshold discrimination is used and the only way to improve the spatial resolution of the detector is to reduce the distance between the anode wires. For small distances between the wires the repulsive electrostatic forces tend to move them off their position. The force that is stretching the wires to keep them in position is limited by the tensile strength of the metal. The limit in the inter-wire distance imposed on even small chambers by the tensile strength is about 1 mm leading to a resolution 1 mm resolution. Various wire support methods were devised to hold the wires and reduce the effect of electrostatic forces, but they lead to locally reduced efficiency.

Thus, it is very difficult to achieve resolution below 0.5 mm with an MWPC. A solution to this problem was suggested by Oed [1] in 1987 with the invention of the Gas MicroStrip Counter (MSGC).

3.3 The Gas Microstrip Counter

The Gas Microstrip Counter, as shown in Figure 3.2, consists of a plane electrode (drift cathode) a few millimetres above an insulating substrate on which thin metal strips (anodes and cathodes) have been deposited using the technology for micro-chip production. With this technology the strips can be very narrow and positioned very accurately. A typical pitch is 200 μm, with the anodes 10 μm wide, the cathodes 90 μm and the distance between anode-cathode 50 μm. The granularity of the detector is about 10 times denser than that of an MWPC. Figure 3.4 shows two different layouts of anode and cathode strips on glass. Special care was required at the ends of the strips to avoid sharp edges that could result in high fields and sparks in the chamber.

The principles of operation are the same as in the MWPC. Figure 3.3 shows the electric field in an MSGC compared with that of an MWPC. Electrons liberated by a passing particle drift in the area of low field and start avalanche multiplication when they reach very close to the anodes. The big difference is the presence of the substrate.

The substrate was originally made from very resistive materials to reduce the "leakage current" from the anodes to the cathodes. This approach is not

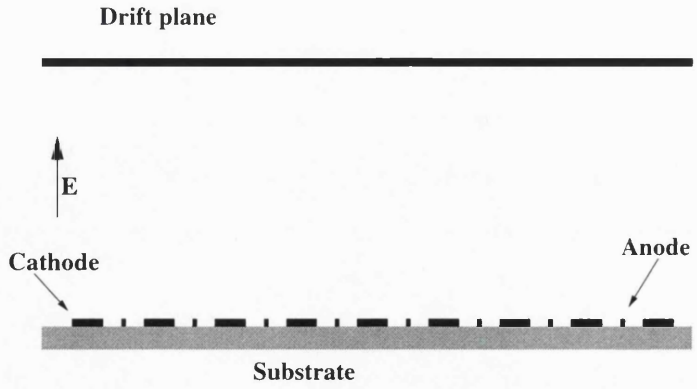

Figure 3.2: Outline of an MSGC detector.

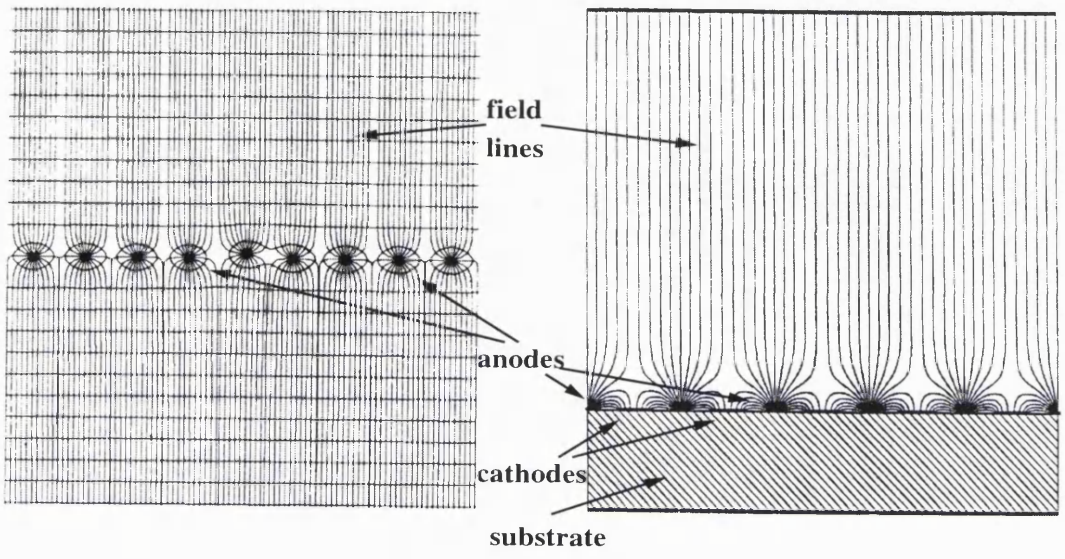

Figure 3.3: The electric field in an MWPC and an MSGC.

very successful because ions tend to get trapped in the substrate and modify the electric field, so the gain of the chamber changes with exposure to radiation. For that reason specially processed glasses with lower resistivity have been developed. In this way the ions trapped in the substrate could drift slowly to the cathodes. With Moscow C85 glass, (10^9 Ω cm), rates up to 10^6 particles/mm^2/s have been reached [26].

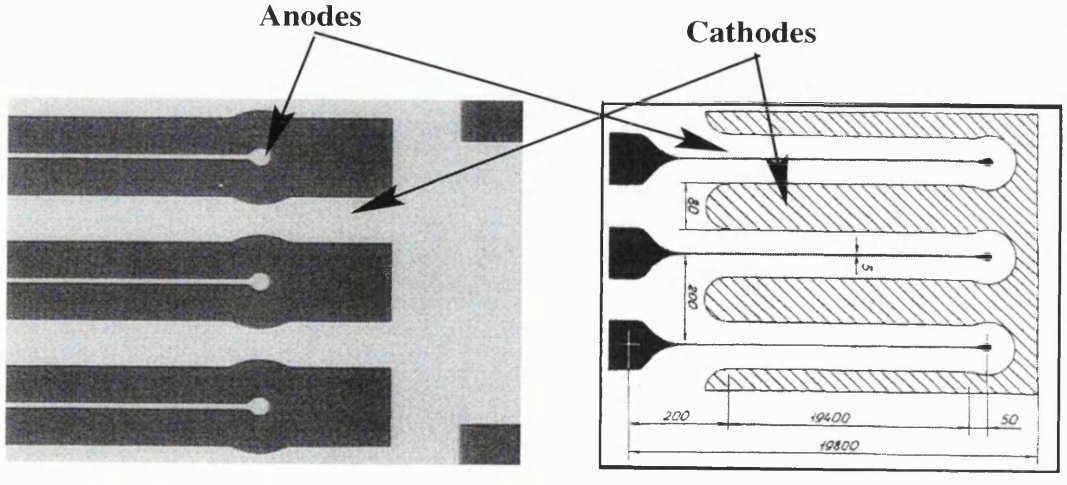

Figure 3.4: Two different layouts of anode and cathode strips on glass.

MSGCs can operate in high particle fluxes without being seriously affected by space charge effects, because the cathode strips are very close to the anode strips. After the avalanche multiplication a large fraction of positive ions is collected by the neighbouring cathodes in less than 1 μs. For the same reason the signal of an MSGC rises much faster than the signal of an MWPC and is less affected by the long drift of ions. The same signal output can be reached with lower gain, when the detector is terminated with a resistor R and the signal is differentiated with a constant RC, because of the faster rise time. However, for rates above 10^6 particle/mm^2/s the ions moving towards the drift cathode start affecting the gain of the chamber.

Another drawback of the presence of the substrate is that its properties change with exposure to radiation. The exact processes are not very well understood, but a lot of theoretical and experimental work is under way, with different types of glass. MSGCs are planned to be used in the tracking of the CMS experiment at the CERN LHC [27], where long life-time under heavy exposure to radiation is essential.

3.3.1 Spatial Resolution

The spatial resolution of an MSGC system for X-ray imaging depends on the following factors:

1. The range of electrons (photoelectrons, Auger electrons, δ-rays) in the gas.
2. The energy, range and generation probability of fluorescence photons.
3. The detector pitch.
4. Diffusion of electrons as they drift towards the anode plane.
5. The discriminator threshold, if the detector is operated in binary mode.

The first two items were discussed in detail in the the previous chapter. In binary mode, with a discriminator on each channel, possibly the only read-out mode that is fast enough for medical applications, the longer the range of electrons the worse the spatial resolution. One factor that affects the range of electrons is the density of the gas. Heavy, dense gases are expected to perform better than light gases. High pressure also increases the density of the gas and can improve the performance of the system by reducing the range of electrons.

For a chamber filled with a xenon/CO_2 mixture at 5 bar, irradiated with 18 keV X-rays the range of the photoelectrons is about 140 μm while the range of Auger electrons is almost negligible. Diffusion of electrons over a drift length of a few millimetres is also about 130 μm, comparable with the ionization spread due to the electron range. Both factors combined should give hits that are either single (only one strip) or double, if the detector pitch is 200 μm, with a very small percentage (depending on the discriminator threshold) giving a hit on three anodes.

Spreading of charge to more than one channels can be very useful in the case where the chamber is not operating in a strict binary mode, like the HR mode of the SDRD, where double hits lead to improve resolution. If a weighting algorithm is used, combining information from more than one anode, then the spreading of charge can improve the resolution significantly. In this case, a detector pitch 2–3 times smaller than the spread of electrons should be used.

Diffusion

A localized distribution of electrons diffuses by multiple collisions due to the thermal energy of the gas, following a Gaussian law:

$$\frac{dN}{N} = \frac{1}{\sqrt{4\pi Dt}} e^{-(x^2/4Dt)}\, dx \tag{3.4}$$

where dN/N is the fraction of charges found in the element dx at a distance x after time t, while D is the diffusion coefficient and it is temperature dependent [14]. The standard deviation in one dimension is given by:

$$\sigma = \sqrt{2Dt} \tag{3.5}$$

If the charges are in a uniform electric field, as in the drift area of an MSGC or MWPC, the time t until they reach the anode is equal to d/v_D. The standard deviation can then be written:

$$\sigma = \sqrt{\frac{2D'}{v_D}}\sqrt{d} \tag{3.6}$$

where d is the distance from the anode, v_D the drift speed and D' the field dependent diffusion coefficient. The diffusion coefficient has to be modified because the energies of the electrons can be higher than the energies expected from the gas temperature, because of the presence of the electric field [28]. Electrons with higher energies spread out more and the diffusion coefficient increases. For a particular field D' and v_D are constant and equation 3.6 becomes:

$$\sigma = K\sqrt{d} \tag{3.7}$$

where K is also sometimes called the diffusion coefficient, expressed usually in $\mu\mathrm{m}/\sqrt{\mathrm{cm}}$. K scales inversely with the square root of pressure.

Diffusion at normal angles to the drift direction is called *transverse* or *lateral* diffusion and along the drift direction *longitudinal* diffusion, and the coefficients can be different. In an MSGC longitudinal diffusion affects only the time development of the signal, which was not studied. In the present work the only diffusion considered is transverse.

Figure 3.5 shows the σ of the electron distribution, in the direction perpendicular to their drift direction, after 1 cm of drift, in Xe/CO_2 mixtures. The solid curves were generated [29] using a program called MAGBOLTZ [30]. The

dashed curved is an interpolation for Xe/CO_2 (80/20). The exact values used can be found in Table 4.2. The field values in the experiments at Novosibirsk were in the region of 1–3 kV/cm/atm. Electrons in CO_2 can stay at thermal energies for much higher fields than other gases because of the existence of rotational and vibrational states that absorb energy in electron-molecule collisions. A field strength of 1 V/cm produces electrons with energies distinctly higher than thermal in argon ("hot gas") while in CO_2 the same behaviour occurs at fields of the order of 2 kV/cm ("cold gas"). In Figure 3.5 diffusion gets lower as the field strength increases but at some point it reaches a minimum and starts increasing again. This is the point where electrons start gaining a significant fraction of their energy from the electric field and the behaviour of the gas mixture stops being thermal. The higher the amount of CO_2 in the mixture the higher the field when that happens.

Diffusion affects the resolution of the detector by spreading out the electrons before they are collected by the anodes. The probability of getting a pulse above the discriminator threshold on more than one anode increases as the diffusion

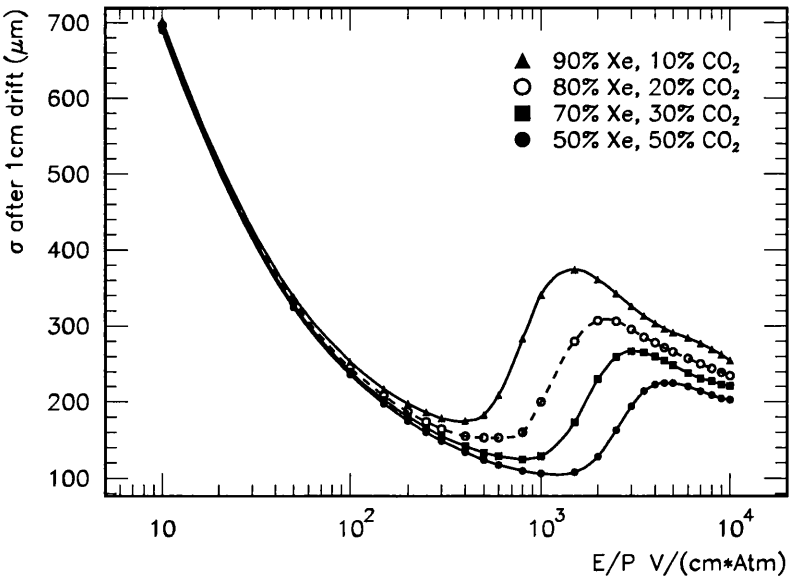

Figure 3.5: σ of electron distribution after 1 cm of drift in Xe/CO_2 mixtures.

coefficient increases. It is thus important to minimize the effects of diffusion. The obvious way is to chose a gas mixture with low diffusion coefficient. Mixtures based on CO_2 for quenching have frequently the lowest values. The use of high pressure also reduces the spreading of electrons by reducing the diffusion coefficient as well as reducing the range of electrons in the main cluster. In some circumstances raising the discriminator threshold may also improve the spatial resolution.

3.3.2 Energy Resolution

The output signal of a detector is not always the same even if exactly the same energy is deposited. The reasons for this may be intrinsic to the detector type or may be due to faults in its construction. The intrinsic factors are due to the actual processes of detection and set the physical limits in the energy resolution. For gas detectors there are two intrinsic factors: the fluctuations in the number of electron-ion pairs and fluctuations in the gain. These factors set the limits of the energy resolution of gas detectors.

Gas detectors detect the ionization in the gas, but since energy can be absorbed in other modes the number of electron-ion pairs created varies from event to event. A varying number of electrons results in a varying output signal. More detailed discussion on the fluctuation of the primary number of electrons can be found in section 2.2.3.

The second intrinsic factor is variation of gain. Every electron when it reaches close to the anode starts an avalanche. The process of multiplication is statistical so the exact number of produced electrons (and the gain of the chamber) cannot be predicted. It follows the Polya distribution [31]:

$$P_m(x) = \frac{m(mx)^{m-1}}{\Gamma(m)} e^{-mx}\, dx \tag{3.8}$$

where $\Gamma(m)$ is the Gamma function. The probability of having gain $g = xG$ (where G is the measured gain of the chamber) is given by $P_m(x)$. The mean value of the Polya distribution is 1 and the variance m^{-1}. For $m = 3/2, P_{3/2}(x)$ is called the Curran distribution and has been found to be a good approximation of the gain fluctuations in wire chambers [31].

Imperfections in the construction of the chamber, like rough metal surfaces, variations in the distance between anodes and cathodes or a non-uniform substrate, affect the local electric field, the local gain and as a result the energy resolution. Impurities in the gas can also affect the energy resolution by capturing electrons before they reach the anodes. Electron clusters created away from the anodes will produce a lower signal than clusters created close to the anodes.

3.4 Choice of Gas

Xenon and CO_2, in a ratio 80:20 were chosen to form the gas mixture for the detector used in the experiments at Novosibirsk (Chapter 5) and for the simulated future system (Chapter 6), for the following reasons:

1. Xenon is the heaviest of the stable noble gases. For that reason it has generally the highest absorption coefficient for X-rays, although at the energy region of 20 keV krypton has a slightly higher absorption coefficient because of its K edge. A high absorption coefficient is essential for a system used in medical applications because it leads to better quantum efficiency and reduced patient dose.

2. Carbon dioxide has the lowest diffusion coefficient of all gases and used as a quencher can reduce the diffusion coefficient of the mixture.

3. Carbon dioxide does not polymerize, so it offers a longer lifetime for the detector. It is also stable in time, important since the detector will probably

operate in a sealed box.

4. The mixture is not flammable, thus no special guidelines are needed for handling the gases.

Chapter 4

Simulation

"As far as we know, our computer has never had an undetected error."

Weisert

As mentioned in the introduction, the purpose of this study is to establish the feasibility of an MSGC for medical imaging, especially mammography. A combination of computer simulation and experiments was used. Computer simulation is a powerful tool, which can be used to model the experimental results of many different set-ups and at a very small cost. The comparison of specific simulation results with experimental data can show if the predictions are correct or not. The model can then be extended to predict the performance of a system which is optimized for a particular application, such as medical imaging.

4.1 EGS4

Electron Gamma Shower 4 (EGS4) [32] is a Monte-Carlo program developed to simulate the interaction of electrons and photons with matter. It is used extensively both in particle physics and in medical physics and has very good documentation. It was found not to be ideal for this study for the following reasons:

- The physical model used for the transport of electron assumes that all the electrons in matter are free. This assumption works nicely when the energy

of the incoming particles is much higher that the binding energy of electrons in matter, and it reduces computing time, but it does not give accurate results when the energy of the particles that are being tracked is comparable with the binding energy of electrons. The program was originally developed for High Energy Physics applications, so this approach is understandable. In recent years the program has been extended to cater for many lower energy problems with biomedical applications in mind. One of the additions has been the the PRESTA subroutine, which makes corrections in the step sizes of the particle transport, and allows electron transport down to 10 keV. But the present study was concerned with showers initiated by primary X-rays with energies in the range from 6 to 20 keV, so even the modified version of EGS4 is not really applicable.

Table 4.1: Processes treated by ITS 3.0 [34].

- **Electron/Positron Interaction**
  - **Energy loss straggling**
  - **Elastic scattering**
  - **Production of knock-on electrons (δ-ray)**
  - **Impact ionization followed by production of fluorescence photons and/or Auger electrons**
  - **Production of annihilation radiation**
- **Photon Interaction**
  - **Photoelectric absorption with the production of photoelectrons, Auger electrons and fluorescence photons**
  - **Incoherent scattering with the production of scattered electrons**
  - **Coherent scattering**
  - **Pair production**

- The photoelectric effect, the dominant process of photon interaction at low energies, is simulated in EGS4, but the photons interact only with the K shells of elements. A significant part of this study, the absorption of 20 keV photons in xenon, could not be simulated with EGS4 because the binding energy of the K shell in xenon is 34.5 keV. A program able to handle L shell interaction was necessary.

- From the relaxation processes after a photoelectric interaction only the K_α fluorescence is simulated by EGS4. It generates no fluorescence photons from other shells and no Auger electrons. Auger electrons in the case of L shell ionization in xenon have initial energy of 5 keV and depending on the pressure of the gas their range can be significant. Again a program able to handle Auger electrons was necessary.

4.2 ITS

The Integrated Tiger Series 3.0 code (ITS) has been developed in SANDIA Labs and is described in its documentation as "a software package for the Monte-Carlo solution of linear, time independent coupled electron/photon radiation transport problems, with or without the presence of macroscopic electric and magnetic fields" [33]. This amounts to the same goal as EGS4 but there are important differences in how it is achieved. The physical model of ITS allows the production and transport of the electron/photon cascade from 1 GeV down to 1 keV. Table 4.1 gives a brief list of the processes simulated by the program.

4.2.1 Description of the Program

As the name suggests, the Integrated Tiger Series is an incorporation of a number of different codes in a single library. The user has to run a program called the

UPDATE emulator to extract the modules needed. The same program can be used to modify the FORTRAN code by inserting or deleting lines. There are three main options to be chosen according to the geometry of the problem in hand:

TIGER A code for one-dimensional problems made of layers of different materials.

CYLTRAN A three-dimensional description of particle trajectories within an axi-symmetric cylindrical geometry.

ACCEPT The option used in this work. It is a general three-dimensional transport code that uses the combinatorial geometry scheme in which the volumes of material inserted in the process are built up of primitive bodies, like a sphere, a box or a cone. These bodies can then be combined, using the union, the difference or the intersection between bodies, or combination of bodies, to create complicated geometries [35].

Other options that can be combined with the three main ones are the M-codes option for macroscopic electric and/or magnetic fields, the P-codes option for low energies and machine compatibility options (VAX, IBM or CRAY).

The P-codes give an improved modelling both of the ionization process and the subsequent relaxation processes and were always used in this study. With the P option, ITS is a more suitable program than EGS4 for simulation of the absorption of low energy X-rays in MSGCs, because there is more detailed modelling of the photoelectric effect, fluorescence and Auger electron emission. Photoelectric interactions are simulated for all K, L, M and N shells as long as the binding energy of the shell is above 1 keV. After the photoelectric interaction, fluorescence and Auger emission are simulated, taking into account electron transitions from all the above shells until the atom returns to its ground state.

No published flow chart of the program has been found in the literature or in its manuals, and the comments that exist within the code are very brief. The

authors of the code (particularly R.P. Kensek of SANDIA labs) were very willing to reply to enquiries and give ad hoc explanations of particular points. They suggested that one of the best accounts on modelling of ITS is to be found in the documentation of a similar program called ETRAN [36]. Figure 4.1 shows a flow chart of the operation of the ITS code, as utilised in this project, in an attempt to fill this gap.

The cross sections for all the processes listed in Table 4.1 are generated by a program called XGEN before the main run of the Monte-Carlo. The input files used for XGEN and ITS are given in Appendix A.

4.2.2 How ITS Works

All Monte-Carlo simulation programs make use of random numbers to sample various quantities—like energy deposition—from known distributions. These distributions depend on the energy of the particle and have to be re-calculated every time the energy of the particle changes. ITS, which Kensek has classified as a "Class I" code, pre-calculates a table with electron transport step sizes for a number of different energies. It also pre-calculates sampling distributions based on these step sizes. That saves a lot on computing time, because for a given electron energy the program looks up the appropriate step size from the table and then samples the pre-calculated distributions that correspond to that step size. The disadvantage of this method is that the step size cannot be changed if necessary, for instance when a boundary between zones is crossed. In this case ITS deposits energy in both zones proportionally to the length of the electron track in each one of them. "Class II" codes, like EGS4, sample a distance for each step and then calculate the necessary distributions based upon this distance. This is more time consuming, but more flexible.

The geometry of the problem is made up of user defined zones. Every zone

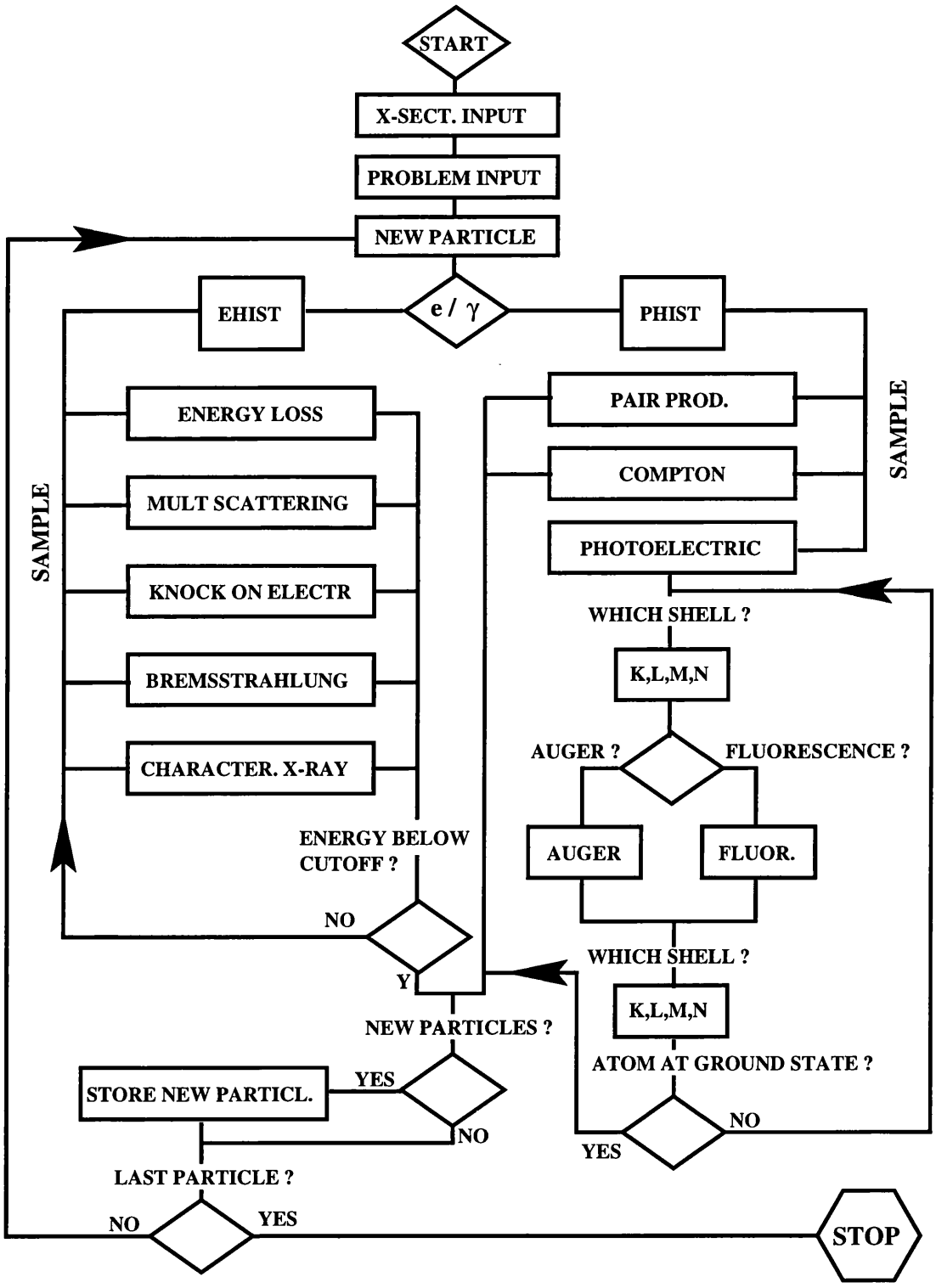

Figure 4.1: Flowchart of ITS (ACCEPT, P-option).

occupies a certain sub-volume of the geometry and can be made of different material. The zones are also used for scoring energy deposition, so if a detailed mapping of energy deposition is needed the volume of interest must be divided into a large number of zones. The volume of each zone, or a subroutine with the necessary logic for the calculation of the volume, has to be provided separately.

The initial particles can be either electrons or photons. They may be monoenergetic or sampled from a spectrum and the particle source can be point-like, or a disc. The default direction is along the z-axis, but in ACCEPT the keyword DIRECTION can be used to define the direction in terms of θ and ϕ. The user can easily create customised sources by modifying the FORTRAN code using the UPDATE program. Particle transport in ITS is done in steps and sub-steps. A table of step sizes is pre-calculated in the XGEN program for a number of particle energies and cannot be modified. The user has access to the number of sub-steps per step using the keyword SUBSTEP. The number of sub-steps is initialised to an empirical value and can be increased to match the geometry of the problem in hand. According to the authors there are no physical limitations in the number of sub-steps per step, but very big values (above 50) could cause inaccuracies in the numerical calculations. A number of about ten sub-steps per scoring zone is required to give accurate results. Care was taken to follow this rule in the simulations. A test was done by solving the same problem with different zone sizes and no problems were observed.

The default output of the program contains mainly:

- The number of events for the various physical processes (e.g. photoelectric ionization, Compton scattering etc.) that were generated and the energies that correspond to these processes. No distinction is made between processes initiated by primary or secondary particles.

- The energy and charge that was deposited in the user defined zones.

- A number that shows how accurately energy was conserved. Since the energy loss of the particles is treated in a statistical way there is always the possibility of an error in energy deposition. This number provides an extra test of the program.

Other output options include the scoring of electrons and photons that escape the defined geometry, or the scoring of the electron or photon flux that crosses the boundaries between certain zones. The user can create specialised output by modifying the code with the UPDATE program.

A significant problem which had to be solved before ITS could be used at all stemmed from the fact that ITS was designed to calculate energy depositions averaged over large numbers of incoming particles, rather than event by event. In this work the energy deposition of individual photons was essential. Since an MSGC is a counting and not an integrating device, information for the energy deposition of individual X-ray photons was necessary if the actual counting process was to be simulated accurately.

Small modifications were made to the program in order to generate an output for individual particles. The files that were used as input for the UPDATE program and the actual Monte-Carlo can be found in Appendix A. A feature of ITS is the division of the number of primary particles into batches with a new seed for the random number generator for every batch. This is done so that statistical errors can be calculated for the output. The output subroutine is called at the end of every batch and the final output consists of the average of all batches. By setting the number of batches equal the to number of primary particles the output subroutine is called every time all the events triggered by one primary particle have terminated. With a small modification of the FORTRAN code the energy deposition from each individual primary particle could be written as a separate record in a file. The file of these records was then available for further analysis.

A fundamental question and its answer

A problem of energy depositions with negative values appeared when ITS was used to score energy depositions of individual X-ray photons. The negative values have no physical meaning and the problem has its roots in a peculiarity of the modelling of the program. In the modelling of electron transport the production of δ-rays is sampled from a distribution that is independent of the energy loss of electrons. A δ-ray can be deemed to be created even if the energy which was deposited at that point is less than the energy of the δ-ray. The extra energy needed is subtracted from the medium and appears as a negative energy deposition. These negative depositions of individual particles disappear when the average over thousands of particles per batch is calculated and this is why the writers of the program made use of such a model. But the problem becomes acute in our case where each batch contains only one primary particle.

The generation of events that had some negative energy deposition could be limited with the use of large zone sizes, so that enough "positive" energy would be deposited to cancel them out. However, the size of the zones had to be small enough to give good spatial resolution at the same time. The combination of photon energy, gas density and zone size used in the simulations was such that about 1–10% of the simulated events had some negative energy deposition.

One approach used was to correct the output of ITS before it was used for the simulation of an MSGC. A negative deposition was created because a δ-ray had been generated at a point where the electron had not deposited enough energy. But if the electron had deposited enough energy in one of the neighbouring zones (within 50 μm) then the error was not very significant. A program was written to look for zones with negative energy and then find a neighbouring zone with positive energy of a value higher than the absolute value of the negative energy zone. If there was one, the program would put the energy content of the zone with the negative energy to zero, and subtract that amount from the zone with

the positive energy.

There were of course cases when even this approach did not work. Especially for gas mixtures at atmospheric pressure, where electrons do not lose energy as fast as for higher pressures, about 1% of the events had some negative energy deposition without having big positive energy depositions in adjacent zones. These events were without physical meaning and had to be discarded. The creation of negative energy depositions is a random process depending only on the energy of the primary particle. Since all primary photons had the same energy no bias is expected from the rejected events.

4.2.3 Energy Deposition

For the simulation purposes of this study ITS was used to generate the initial spatial distribution due to energy deposition of individual X-ray photons. As mentioned before the energy deposition mapping of the detector volume is done by recording the energy deposited in the user defined zones (in this case small boxes). Good spatial resolution was needed to localise the ionization in the gas, but zones that were very small would create problems with negative energy depositions. Zones with dimensions of about 50 μm in the directions of interest (across the strips and along the drift) provided sufficient spatial resolution without creating big problems with negative energy depositions. The error of positioning electrons within boxes of 50 μm is $50\,\mu\text{m}/\sqrt{12} \simeq 15\,\mu\text{m}$; much smaller than the contribution from diffusion which varied from 70 to 130 μm.

The two different geometries described in section 1.2.1 were simulated. In both cases the direction of the beam was along the z-axis.

For the "perpendicular" geometry (Figure 1.6a), the x-axis was chosen to be across the strips, the y-axis along the strips and the z-axis along the direction of the drift. The volume of the detector simulated was 4 mm $\times$ 150 mm $\times$ 5

mm ($x \times y \times z$). This volume was divided into 100 zones along the x-axis (every 40 μm) and 100 zones along the z-axis (every 50 μm) as seen in Figure 4.2a. No division into zones was made along the y-axis since the strips were considered uniform along all their length.

For the "tangential" geometry (Figure 1.6b) the simulation was performed not for a keystone tile but for tiles with parallel strips. The effect of the varying detector pitch was studied by simulating three detectors with pitch of 180, 190 and 200 μm (see section 6.3.1). A complete three-dimensional simulation was not made, because of the extremely large number of zones that would have been required. The division into zones was done again with the x-axis in the direction across the strips, the y-axis the direction opposite to the direction of the drift and the z-axis the direction along the strips. The simulated detector volume was the same as before. The division into to zones this time was made along the x-axis (again every 40 μm) and along the y-axis (every 50 μm) as shown in Figure 4.2b. No division was made along the z-axis (along the strips).

The zones were numbered from 1 to 10000. After the end of all the histories that were initiated by one source photon, the program wrote the zones with non-zero energy content and their energy to a file. The zone number was used to provide the spatial coordinates and the energy as a measure for the ionization in the zone area.

4.3 From Energy Deposition to Signal Generation

The energy deposition in the detector volume is only the beginning of the simulation of an MSGC. It is the electrons in the gas that create the signal, and electrons diffuse before they reach the anodes. For that reason, a special program was de-

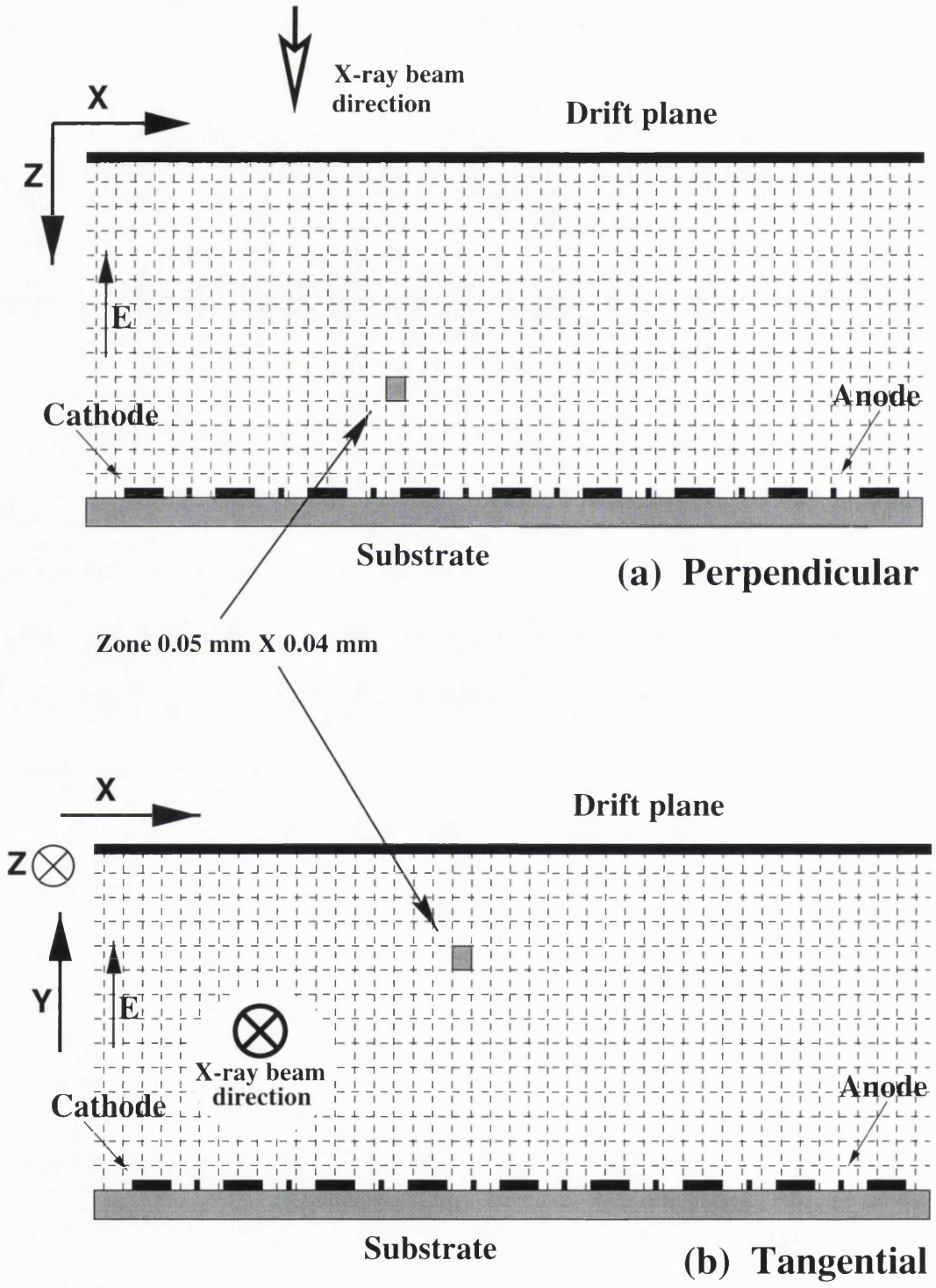

Figure 4.2: Division of the detector volume into zones for energy deposition. a) Perpendicular geometry, b) Tangential geometry.

veloped to take the output of ITS and use it to simulate the performance of the detector. The task is performed in five stages:

1. The energy deposition in every zone is converted into a number of electrons by dividing the energy by W, the average energy to create an electron ion pair. Adding these numbers for all zones gives the total number of electrons per event, which is the same for all events with the same energy. This number is used as the mean number of electrons per event. Fluctuations on this number are introduced by sampling a Gaussian distribution [37] with mean zero and σ the value from the Fano factor calculation (see section 2.2.3). The sampled number is added to (or subtracted from) the mean number of electrons to give the number of electrons for the particular event. The extra electrons are added to (or subtracted from) the number of electrons generated by ITS in separate zones, one by one, choosing the zones randomly. After the number of electrons for every zone has been specified, the electrons are distributed uniformly (by sampling a flat distribution) inside their zone, so each one has an exact position (Figure 4.3 (a) and (b)).

2. The effect of impurities in the gas is simulated by introducing a probability of electron capture. The probability has the form $p = 1 - e^{-cS}$ where c is a constant and S the distance the electron has to travel to reach the anode. For $S = 0$ (the electron being very close to the anode) the probability is zero, and for big S the probability goes to one. Whether the electron is captured or not is decided by sampling a uniform distribution from zero to one and comparing the outcome with the value of p. If the sampled number is smaller than p the electron is captured.

   This effect was used only in the simulations of the experiments in Novosibirsk where we had reasons to believe that the gas was not absolutely clean. The value of the constant was scaled with pressure, since the number of molecules per unit length increases linearly with pressure, and was tuned

Table 4.2: Diffusion coefficients for the gas mixtures used in the simulations.

	$Ar/isoC_4H_{10}$[a]	Xe/CO_2[b]			
Pressure (bar)	1	2	3	5	7
Dif. coef. ($\mu m/\sqrt{cm}$)	235	300	220	160	160

[a]See ref. [14]
[b]Calculated with MAGBOLTZ [30]

to fit the experimental data.

3. Electrons are allowed to diffuse in the direction across the strips during their drift to the anodes. Diffusion is sampled from a Gaussian distribution with sigma $\sigma = D\sqrt{S}$ where D is the diffusion coefficient for the specific gas mixture and S is the distance from the microstrip tile. The diffusion coefficients used in the simulation are shown in Table 4.2. The sampled number is added to the initial position of the electron to determine its position just before reaching the anodes. Since the electric field is not simulated, all electrons arriving in the area from the middle of one cathode to the middle of the next cathode are considered to be collected by the anode between the two cathodes (Figure 4.3 (c)). And since the development of the signal in time was not part of this study, all electrons are considered to arrive at the same time.

4. Just before its arrival at the anode, every electron is multiplied by a gain factor G. This gain is the result of the avalanche multiplication process in the gas which is a statistical process that follows the Polya distribution, described in section 3.3.2. This distribution was sampled using the subroutines HISPRE and HISRAN from the CERN library. HISRAN is a subroutine that samples a distribution which is given in histogram form and HISPRE has to be called before HISRAN to prepare the array that represents the histogram.

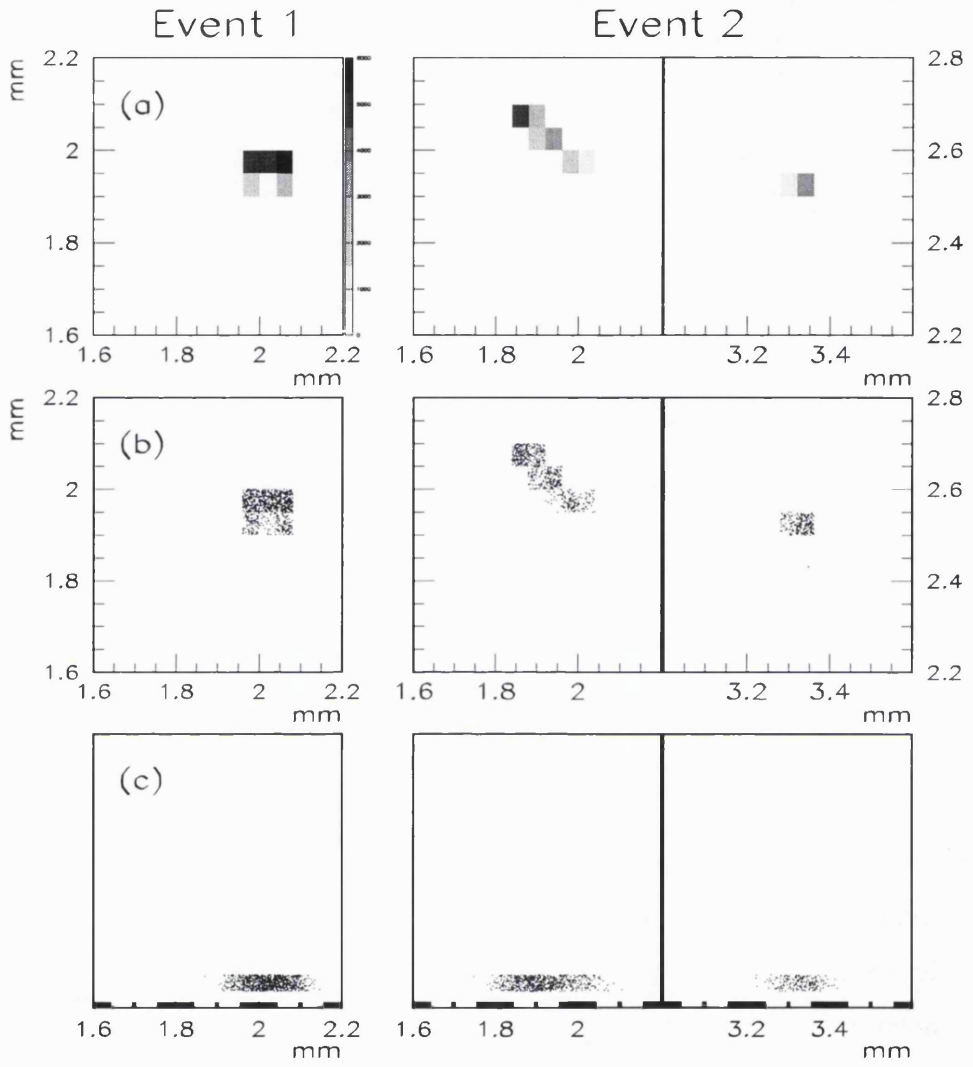

Figure 4.3: Two photon conversions: in event 1 an Auger electron followed the photoelectron. Both electrons have undergone multiple scattering and have not travelled far from the interaction point. The energy density around the interaction point is high. In event 2 a fluorescence photon was emitted after the photoelectric interaction, which also converted in the detector volume about 1.5 mm further away. To keep the scale the same and the zones visible, only the area close to the two interaction points is shown. The first photoelectron followed a rather straight path ionising the gas away from the interaction point. The second photoelectron did not have enough energy to travel far. (a) ITS output; the 40×50 μm zones are shown with their energy content. (b) The energy deposition has been converted to number of electrons and each dot represents one electron. (c) The electron cloud after lateral diffusion just before reaching the anodes. No attempt has been made to represent the true distribution in time. The detector pitch is 200 μm.

All the electrons that arrive at each anode are added together to create the anode signal. This signal is then converted from number of electrons to keV so that it does not depend on the gain of the chamber and can easily be compared with experimental data. For the conversion the program is run once giving the output in number of electrons. The energy of the peak in the spectrum is known so an extra factor is then introduced in the program to convert the number of electrons to keV.

5. Noise is added to the signal, if the results are to be compared with experiments, from a distribution that has been measured in the experiment. Noise is estimated in the experiment by collecting a pulse height spectrum without a source triggering the detector. Ideally the spectrum should be just a line at the value of the ADC pedestal, but noise spreads the spectrum to a (usually) Gaussian distribution. In the simulation, noise is inserted to the signal by adding samples of a Gaussian distribution to give similar results.

Chapter 5

Experiments and Comparison with Simulation

It is usually said that the final test of a theory is the experiment. This is also true for computer simulations. The only way to validate a model is to compare its predictions with experiments. The methods and results from the experiments at Novosibirsk and UCL are presented in this chapter together with the results from the simulations.

5.1 Experiments with Xe/CO_2, 2–7 bar

A special visit was made to the Budker Institute of Nuclear Physics in Novosibirsk, Russia, to take data with their equipment. The Novosibirsk group had experience in pressurised gas chambers from the SDRD work and they were starting a series of experiments to investigate the use of MSGCs for medical applications. They were particularly interested in the simulation methods described in the previous chapter. A number of joint publications resulted from this visit [38].

5.1.1 Description of Laboratory Set-up in Novosibirsk

The laboratory installation consisted of an X-ray source, a microstrip detector in a pressurised box, a slit collimator, and the associated electronics for operating and reading out the detector (Figure 5.1). The size of the sensitive area of the detector was 2 cm wide (across the strips, 96 channels) each strip being 1 cm long. The distance between anodes was 200 μm and the drift gap 5 mm. The window of the pressurised box was about 3 cm $\times$ 2 cm (slightly bigger than the detector), made of 1 mm thick beryllium. Beryllium has a very small cross section for X-ray absorption and is the ideal window material for X-ray sources or detectors. A piece of aluminized mylar was glued to the inner side of the beryllium window, and acted as the drift electrode. In this way, there were no dead areas in the gas. The gas mixture used was 80% xenon and 20% CO_2 at pressures of 2 to 7 bar. A lead collimator 2 cm wide and 0.5 cm long was placed in front of the window during all the measurements to reduce the effective window size along the strips. Two high voltage power supplies were used, one to provide high voltage for the drift plane and one for the cathode strips, the anodes being grounded. All the voltages given were negative with respect to the ground.

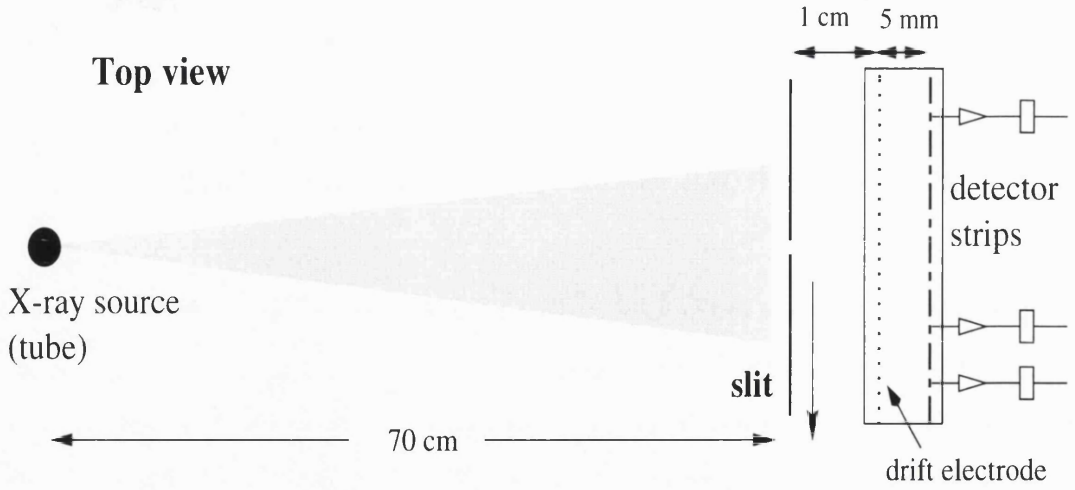

Figure 5.1: Schematic diagram of the experimental set-up in Novosibisk.

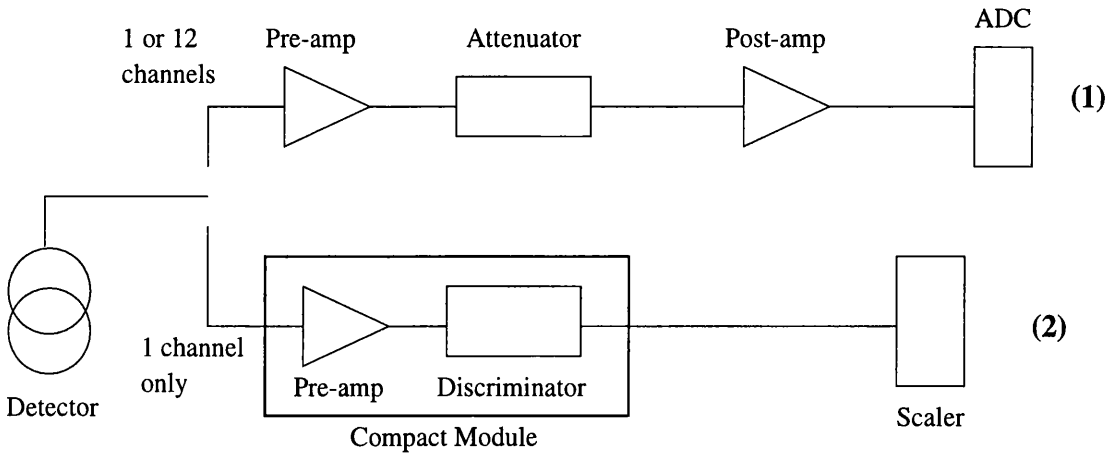

Figure 5.2: Configuration of read out electronics in Novosibirsk. Line (1) was used for spectra collection, while line (2) was used for spatial resolution measurements.

Two different configurations were used in the read-out electronics (Figure 5.2). Line (1) was used for spectrum (pulse height) measurements. Either one or twelve anodes together were connected to a pre-amplifier and a post-amplifier, and then to a CAMAC ADC. The attenuator was used because the gain of the post-amplifier was fixed. Line (2) was used for spatial resolution measurements. Compact modules, with a pre-amplifier and a discriminator for every anode, were plugged into the pressurised box and produced a digital signal that was read by scalers in a CAMAC crate. A PC was used to read the CAMAC units in both cases.

Two sources of X-rays were used; a Cadmium source and a tungsten anode X-ray tube. The ^{109}Cd source is known to produce a double X-ray line at 21.9 and 22.1 keV and was used as a reference energy. The tube could operate in the range 0–40 kV, and two voltage settings, 15 and 30 kV were used in the experiments. Tungsten characteristic K lines are above 70 keV, so the main process of X-ray generation was bremsstrahlung of electrons. The exact shape of the spectrum was not measured but Figure 5.3 shows a typical spectrum produced by a tube with a tungsten target at 30 kV, and filtered with 1 mm of beryllium and 0.5 mm of aluminium [12]. However, the tube used had a glass window with a higher X-ray absorption coefficient than the Be/Al combination, so the lower

energy end of the spectrum could be different than the one shown in Figure 5.3. A Molybdenum filter was also used to reduce the range of energies when the voltage was set to 30 kV.

5.1.2 Calibration Measurements

A number of spectra were collected for calibration purposes before any spatial resolution measurements. Figure 5.4 shows spectra taken at 5 bar using Line (1) of Figure 5.2 with 12 strips connected together or (Figure 5.4c only) using a single strip. The settings of the pre-amp and post-amp were kept constant throughout the experiments.

Figure 5.4a shows spectra taken either with the ^{109}Cd source or with one of two different voltages (15 and 30 KV) on the X-ray tube. The spectra are clearly broadened by the energy resolution of the detector, which can be calculated from the FWHM of the ^{109}Cd spectrum (28% for 22 keV). An interesting feature of the spectra is a long tail in the low energy region. This is probably due to electronegative impurities in the gas which can capture electrons before they reach

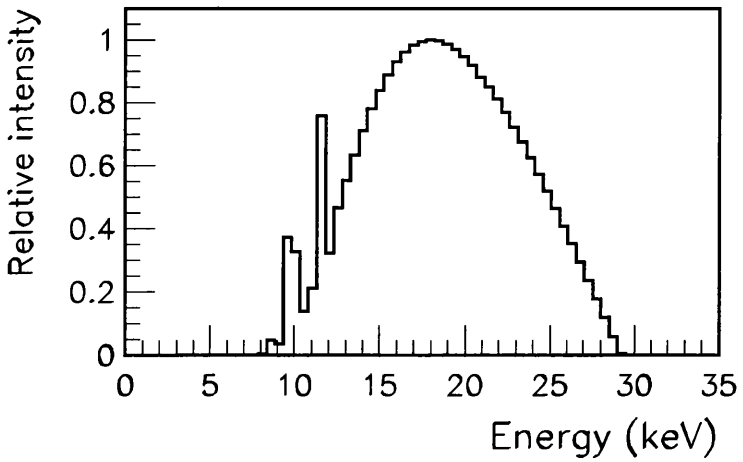

Figure 5.3: Typical X-ray spectrum produced by a tube with a tungsten target at 30 kV and filtered with 1 mm of beryllium and 0.5 mm of aluminium.

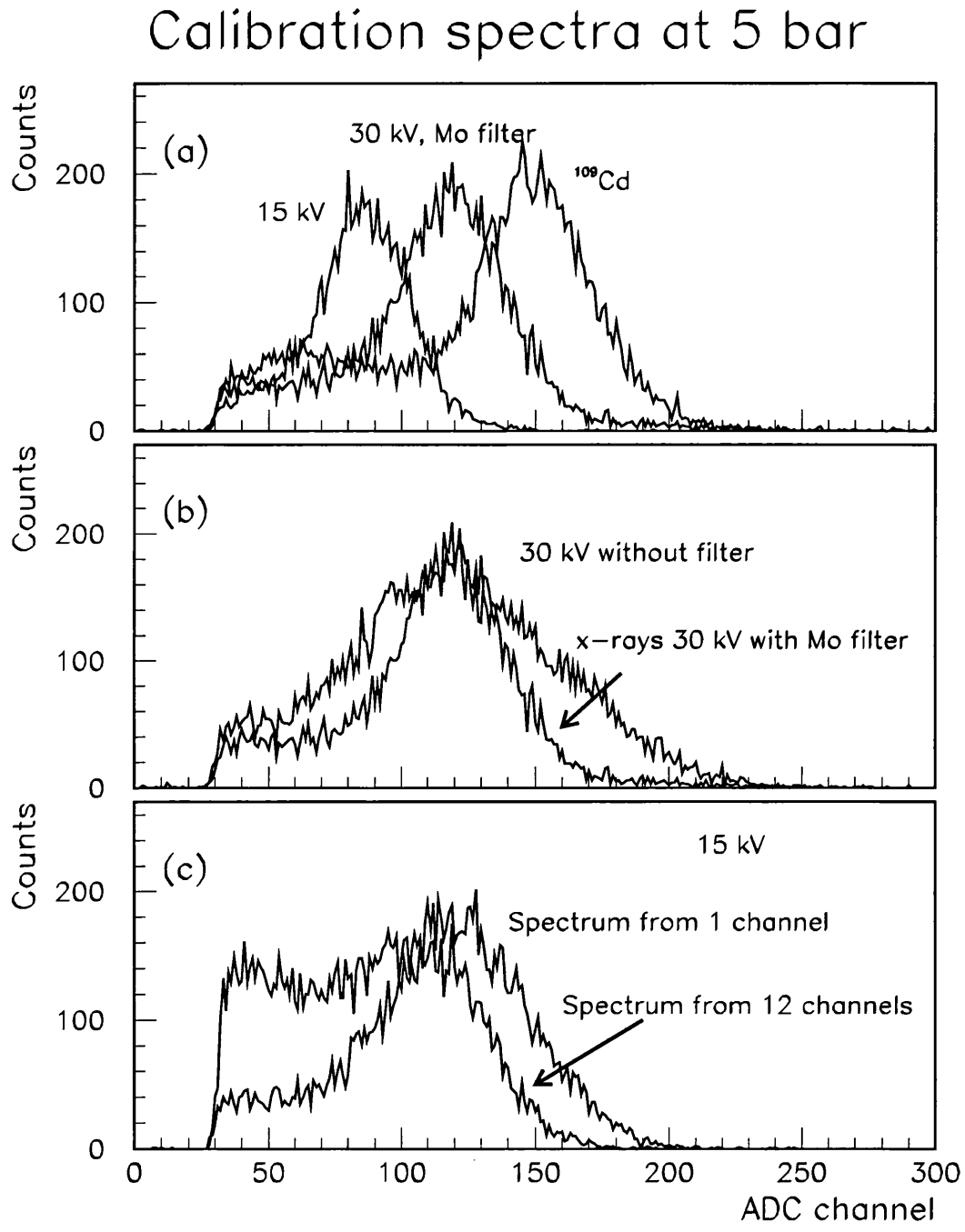

Figure 5.4: (a) Spectra showing different energy X-rays. (b) Spectra showing the difference with and without Mo filter. (c) Spectra showing the difference between one and 12 channels.

the anodes. Other smaller contributions to the tail could be due to conversions that take place close to the outermost strips of the 12 channel group so that not all of the energy of the photoelectron is collected. Fluorescence photons could also contribute, either by escaping the area covered by the 12 anodes, or by being detected within that area, even though the primary conversion was outside the 12 channel group. However, simulations with the ITS program showed that after L-shell ionization the xenon atom returns to the ground state mainly by emitting an Auger electron, so fluorescence is not expected to make a significant contribution. The ^{109}Cd spectrum was used as reference for the calculation of the energy of the two other peaks. The Russian group had set up the ADC with a linear response and no offset of the zero. The 30 kV peak was calculated to be at 17.8 keV and the 15 kV at 13.2 keV.

The effect of the Molybdenum filter is shown in Figure 5.4b. The unfiltered spectrum has its peak at 17.8 keV in agreement with Figure 5.3 which shows the spectrum from a tube with the same settings. The filtered spectrum has also its peak at the same energy. Materials tend to be transparent to their own characteristic X-rays (see chapter 2), and the Molybdenum characteristic X-rays are at 17.5 keV. The range of energies after filtering is clearly reduced significantly. The FWHM of the curve is 35% which, compared with the FWHM for the ^{109}Cd source (28%), means that the spectrum after filtering is not monochromatic.

Figure 5.4c shows the difference between spectra collected with a 12 channel group or just one channel using 15 kV photons. The tail at low energies is much more marked for one channel readout. This shows that with uniform irradiation of the chamber, only part of the photon energy is collected in one channel. That is why it was found more useful to take the spectra with 12 anodes joined together. The spectrum from 1 channel appears to reach its maximum at slightly higher energies than does the spectrum from the 12 channels. This is probably due to the lower capacitance of one channel which leads to higher effective gain in the pre-amp.

5.1.3 Spatial Resolution Measurements

The spatial resolution of the detector was measured for different gas pressures, for different cathode voltages and for two settings on the X-ray tube, 15 and 30 kV. Line (2) of the readout electronics (Figure 5.2) was used, and the threshold of the discriminator and the gain of the pre-amplifier were kept constant.

The threshold of the discriminator was measured by the Novosibirsk group with the following procedure. A step voltage pulse from a square pulse generator was applied to the input of the pre-amplifier through a known capacitance. The pulse had a very short rise time and very long width compared to the shaping time of the pre-amplifier, so the charge delivered was known accurately from the height of the voltage step and the value of the capacitance. The height of the test pulse was increased until the scaler connected to the discriminator gave a number of counts equal to half the number of pulses of the generator. The threshold of the discriminator was found to be 6 fC.

The set-up shown in Figure 5.1 was used to measure the spatial resolution of the detector. The size of the X-ray source was 2 mm, the distance between the source and the slit about 70 cm, the width of slit was 50 μm and the distance between the slit and the detector 1 cm. From geometrical arguments we can deduce that the width of the irradiated area on the strip plane was 75 μm. The length of the window along the strips was intentionally reduced to 0.5 mm with the collimator to avoid errors caused by misalignment of the slit with the anodes.

The slit was moved across the strips in 40 μm steps and the number of hits on individual channels was measured over a 10 second period. By plotting the number of hits on one anode versus the position of the slit we get a curve that rises as the slit moves closer to the anode and falls as the slit moves away from the anode. The FWHM of the curve represents the resolution of the detector, the least distance between two distinguishable slits.

Figures 5.5–5.8 show the results for two adjacent channels for different pressures and cathode voltages. The scale of the x-axis is the same in all graphs at the same pressure. It is easy to see the broadening of the curves for higher cathode voltages. Table 5.1 shows a summary of all the results. The estimated error on the FWHM of the curves is ± 10 μm. After each resolution measurement a spectrum would be collected from a 12 anode group and the position of the peak recorded. The position of the peak was an indication of how much charge was delivered to the anodes, assuming that the pulse height is proportional to the charge.

5.1.4 Discussion of the Results

From Table 5.1 we see that the resolution of the MSGC under test varied from 450 μm to 190 μm. For low pressure (2–3 bar) the resolution is slightly better than 0.5 mm, the limit for an MWPC. But for 5 and 7 bar the resolution is around 200 μm, the pitch of the detector. This is very promising for the construction of a device for digital radiology based on microstrip detectors, especially since this resolution was achieved with simple discrimination. Experience from the SDRD has shown that the resolution can be improved with more sophisticated electronic readout (see section 1.1.1).

There are also two interesting observations to be made. First, we can see that for the same pressure and cathode voltage, lower energy photons give better spatial resolution. This could be due to two reasons: more energetic photoelectrons have longer range and/or the fact that higher energy photons produce more charge in the detector, which after diffusion can give a signal above threshold to more anodes. A graph (Figure 5.9) can be made with the resolution of the chamber versus the charge delivered on the anodes (which is the initial charge times the gain of the chamber). This allows comparison of the resolution for the same charge delivered to the anodes, in which case, for lower energy photons the cham-

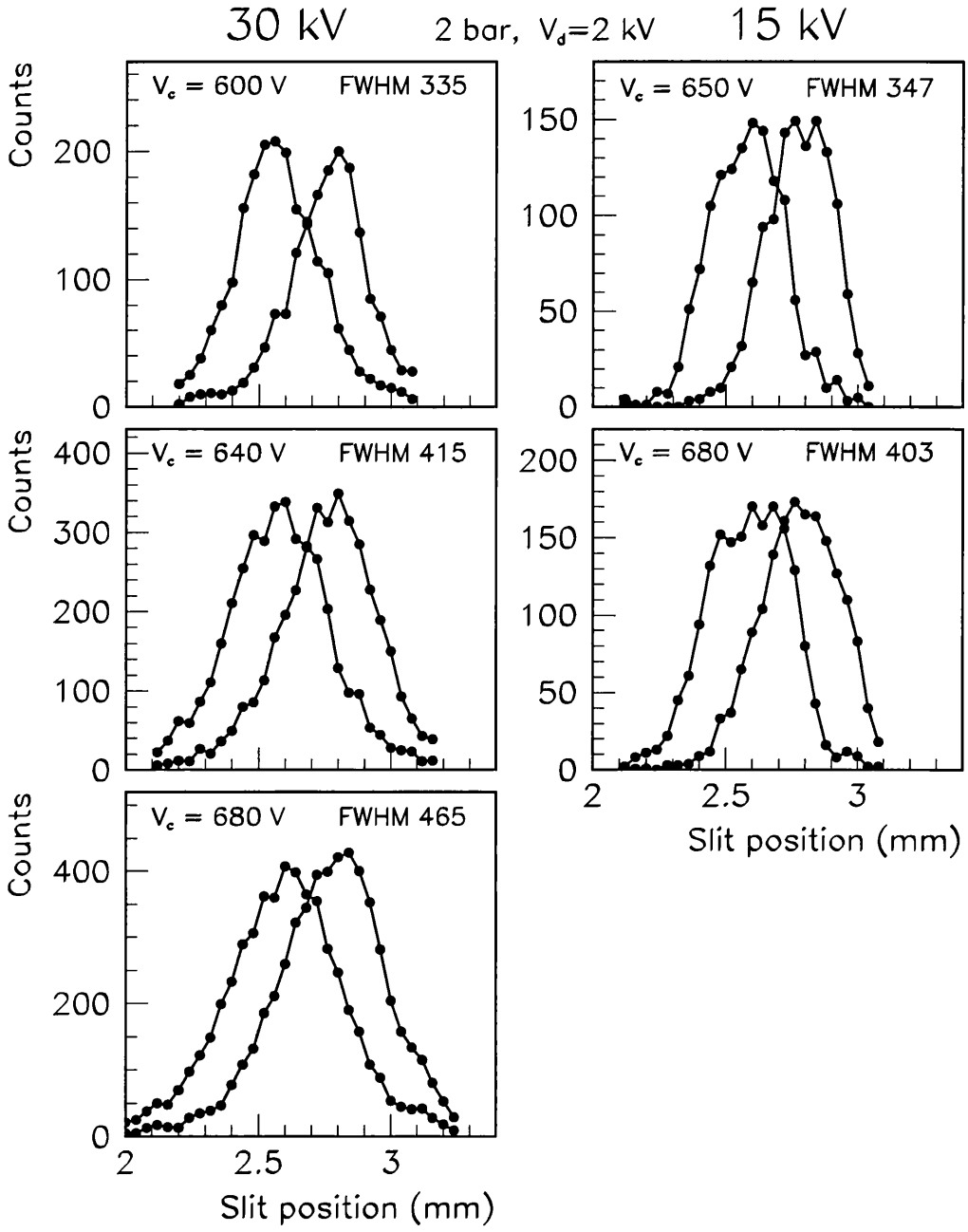

Figure 5.5: Curves for the calculation of the spatial resolution at 2 bar. V_d is the drift voltage, V_c the cathode voltage and 30 kV and 15 kV are the X-ray tube voltages.

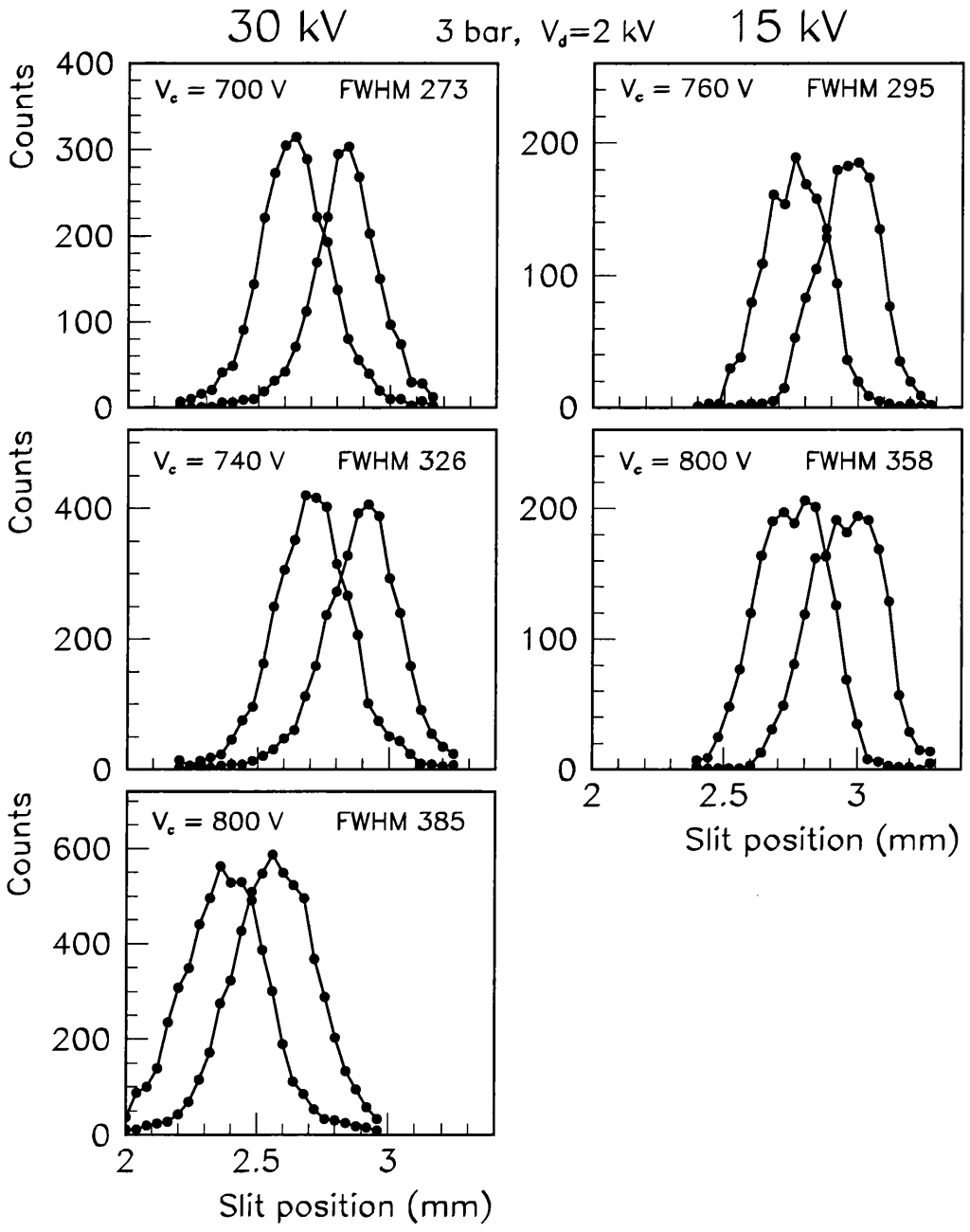

Figure 5.6: Curves for the calculation of the spatial resolution at 3 bar. V_d is the drift voltage, V_c the cathode voltage and 30 kV and 15 kV are the X-ray tube voltages.

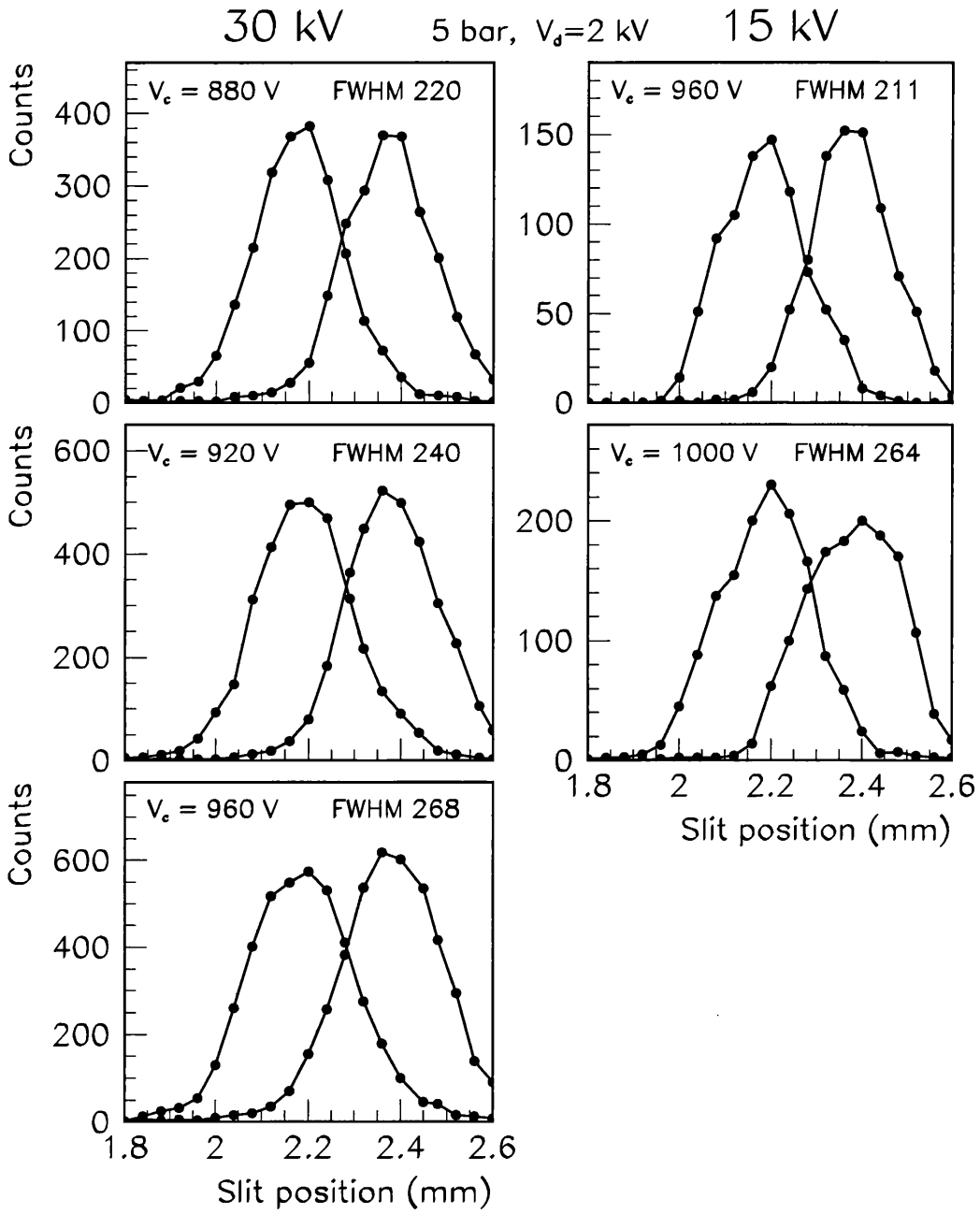

Figure 5.7: Curves for the calculation of the spatial resolution at 5 bar. V_d is the drift voltage, V_c the cathode voltage and 30 kV and 15 kV are the X-ray tube voltages.

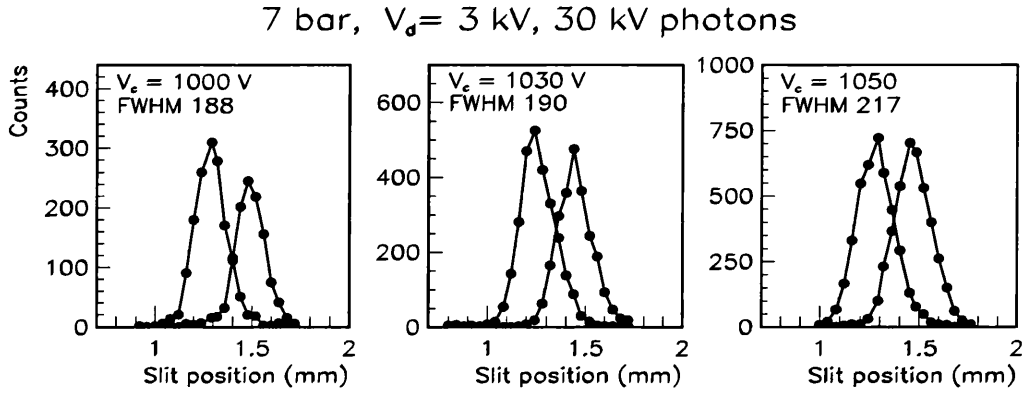

Figure 5.8: Curves for the calculation of the spatial resolution at 7 bar.

ber is operating at a higher gain. If the initial charge deposition was point-like, then the resolution should not depend on the photon energy. However, from the

Table 5.1: Full Width at Half Maximum of all the spatial resolution curves.

Pressure	18 keV photons		13 keV photons	
(bar)	Cath.Volt. (V)	FWHM (μm)	Cath.Vol. (V)	FWHM (μm)
7	1000	188		
	1030	190		
	1050	217		
5	880	220	960	211
	920	240	1000	264
	960	268		
3	700	273	760	295
	740	326	800	358
	800	385		
2	600	335	650	347
	640	415	680	403
	680	465		

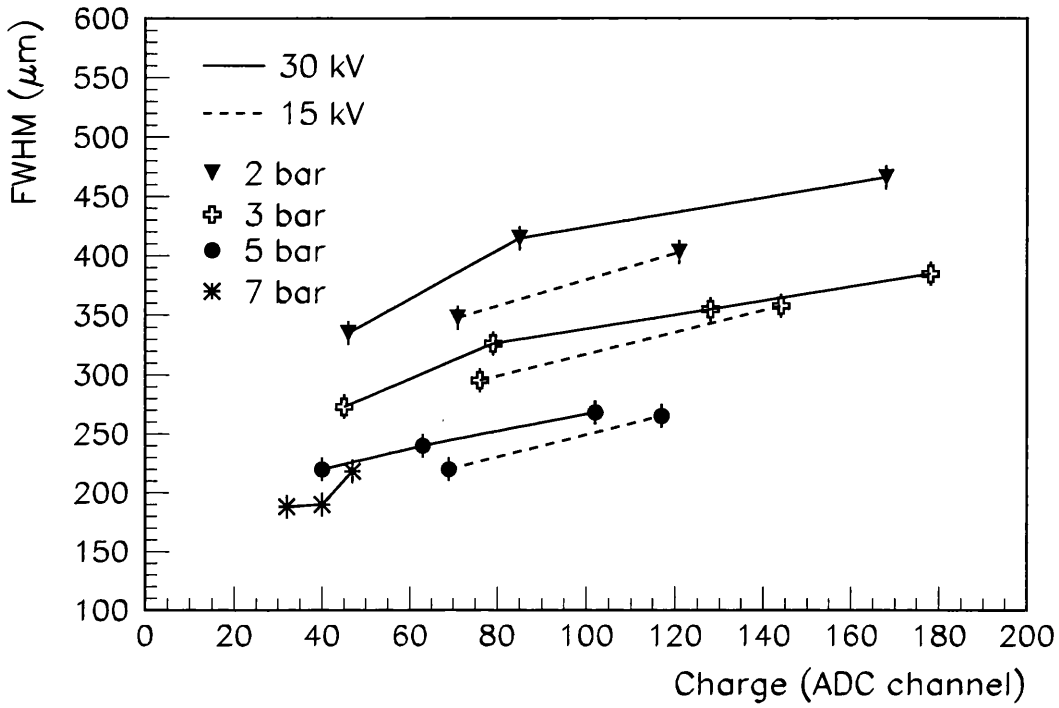

Figure 5.9: Resolution of the chamber versus signal delivered to the anodes.

graph it can be seen that lower energy photons give better resolution for the same output charge. So the range of the photoelectron is an important factor in the resolution of the detector.

Second, it is obvious that for photons of the same energy the resolution of the chamber gets worse with increasing cathode voltage. This is because the chamber gain is higher at higher voltages and a smaller number of initial electrons can produce a hit. So for constant discriminator threshold, the effective threshold, the number of primary electrons necessary to produce a hit, decreases with gain, and that leads to worse resolution. The number of primary electrons reflects the energy deposited in that channel so an effective threshold in energy units is very practical, especially for comparison with simulations.

For each measurement of the spatial resolution the ADC channel of the X-ray peak was recorded. Using this information the 6 fC threshold can be converted

into energy units. The gain of the pre-amplifier was known to be 0.31 mV/fC, so for a 6 fC input, the output was $6 \times 0.31 = 1.86$ mV. Acquisition of a spectrum with the ^{109}Cd source showed that an output of 12 mV corresponded to ADC channel 117. So the threshold charge corresponded to channel $117\frac{1.86}{12} = 18$.

Channel 18 can be converted into energy from the known energy and position of the X-ray peak:

$$E_{th}(\text{keV}) = 18 \times \frac{peak\ energy(\text{keV})}{peak\ position(\text{ch})} \tag{5.1}$$

Equation 5.1 was used to calculate the effective threshold of the discriminator for the each of the spatial resolution measurements. The results for the 18 keV X-rays are shown in Figure 5.10. At 7 bar the limits of the lower threshold were

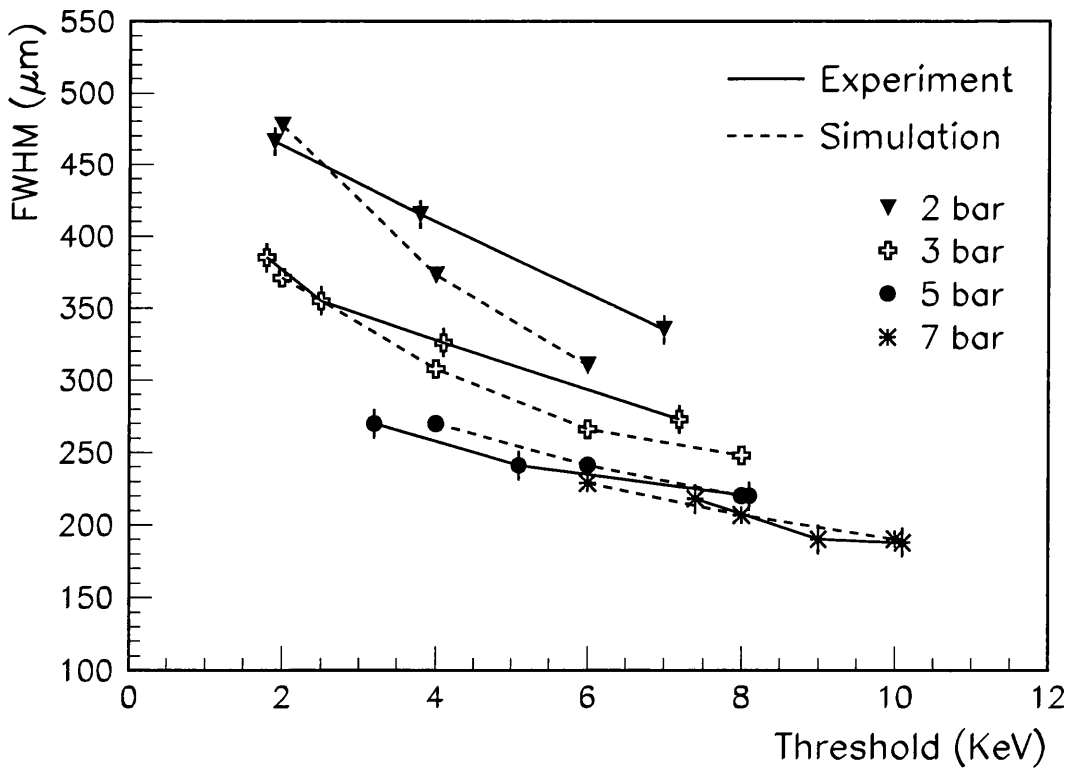

Figure 5.10: Resolution (FWHM) of the detector versus discriminator threshold for 18 keV X-rays. The solid lines join the experimental results; the dashed lines join the results of the simulations.

set by the inability of the chamber to operate at higher voltages. As expected, the resolution gets better for higher thresholds.

The results of the simulation have also been plotted in Figure 5.10 for comparison. The resolution in the simulation was also calculated using a very narrow source that was moved in 40 μm steps. Some of the simulated curves are shown in Figure 5.11. They are much smoother than the experimental curves because the same initial number of photons was generated for all the points of the same curve. The experimental curves were produced by exposing the detector to X-rays for the same time for all points, but the detected number of photons fluctuated as expected from the random nature of photon interactions.

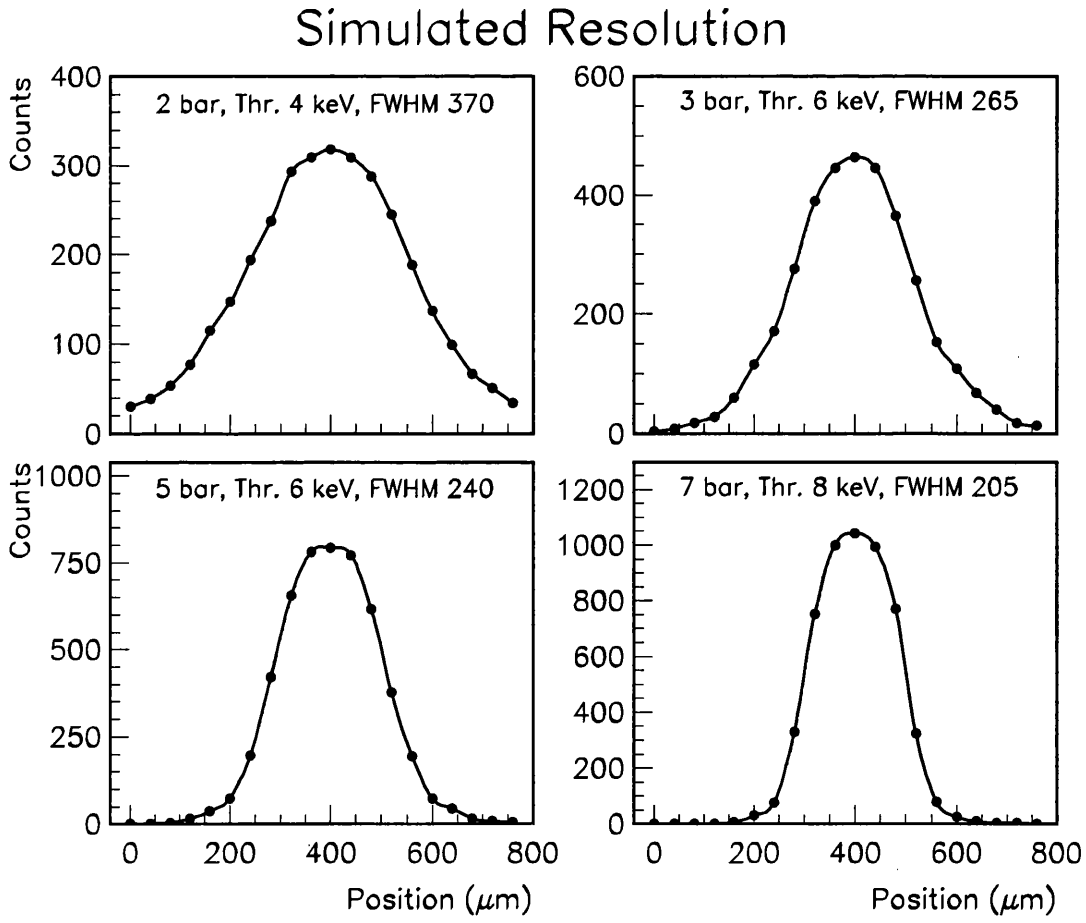

Figure 5.11: Simulated resolution for various pressures and thresholds.

Since the exact spectrum of X-rays in the experiments was not known a source with energy 17.8 keV was used in the simulation. The only free parameter in the model was the mean free path for electron capture due to impurities in the gas. Electron capture affects the resolution because fewer electrons reach the anodes creating a lower signal that could be below threshold. The smaller the mean free path the better the resolution. The measurements were performed by filling the chamber to 7 bar and then releasing gas to reduce the pressure. The chamber had been cleaned thoroughly before being filled, so a constant fraction of impurities was assumed for all measurements. Since gas density scales inversely with pressure the same relation was used for the mean free path. The best values were obtained with a mean free path of 50 mm, which hardly affected the resolution for 2 bar (where the biggest difference appears). The difference between experimental data and simulation at 2 bar cannot be improved by changing the mean free path for electron caption, as that would increase the difference by improving the simulated resolution.

5.2 Experiments with Ar/Isobutane, 1 bar

Although the simulation results could be made to agree reasonably with the experiments at Novosibirsk, further testing of the Monte-Carlo was needed. Experiments were planned at UCL to provide more data for comparison with simulations. The advantages of performing an experiment at UCL were complete control of the apparatus, time for repeated measurements, ability to change various parameters and collection of data that could be compared with simulations in a direct way. An MSGC filled with Ar/Isobutane was used and pulse heights distribution on individual anodes were recorded.

The MSGC was built at RAL and came as a complete assembly with preamplifiers and post-amplifiers (Figures 5.12, 5.13). The strips were made of alu-

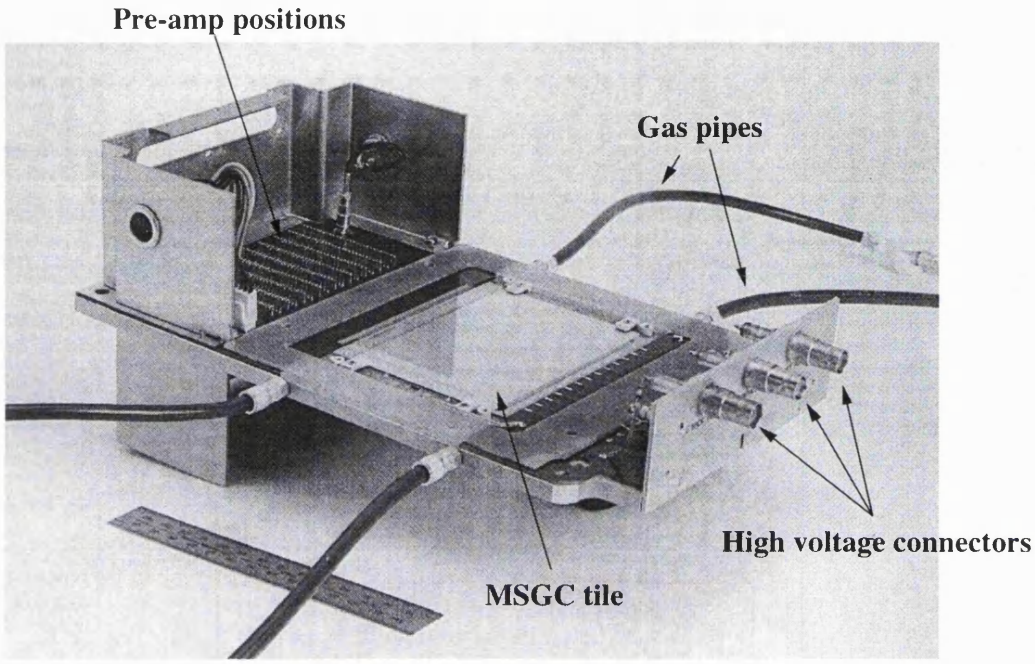

Figure 5.12: A RAL MSGC assembly, identical with the one used for our experiments.

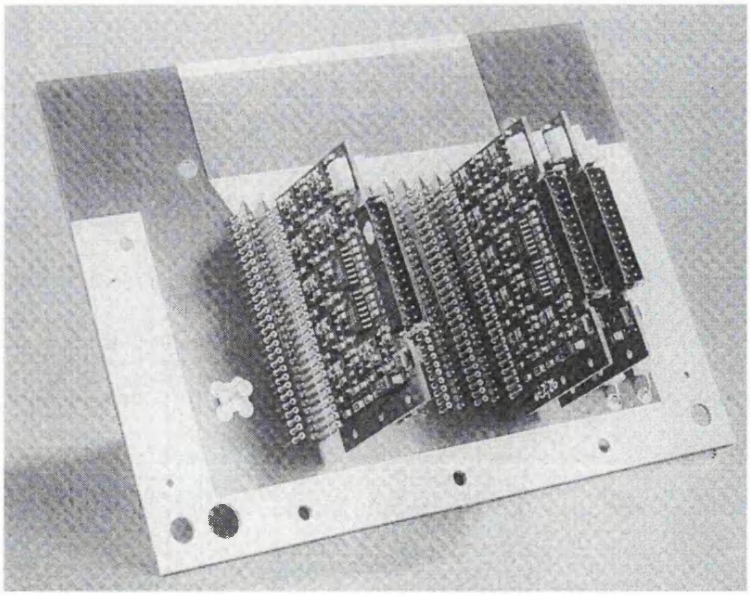

Figure 5.13: RAL hybrid preamplifier boards plugged into position.

minium and were deposited on Tempax glass. The anodes were 10 μm wide and the cathodes 90 μm. The pitch of the detector was 300 μm and the distance from the drift cathode to the anodes 3 mm. Out of the 270 anodes a group of 16 was connected to a block of 16 pre-amplifiers and about 20 cathodes, containing the 16 anodes, were biased. The output of the post-amplifiers was differential and was matched by a transformer to oscilloscope or ADC input. The gas mixture used through out the experiments was Ar/Isobutane 80/20. The gas proportions were regulated with flow-meters and there was a constant gas flow. The flow-meters were calibrated by making the gas bubble in a measuring cylinder filled with water and turned upside down in a bowl.

5.2.1 Data Acquisition Using a Digital Scope and a PC

Preliminary exploration of the chamber performance, including energy resolution measurements, was done with a four-channel digital oscilloscope connected to a Pentium PC via a GPIB board. The PC was running LabVIEW 3.0 and a program was developed for the communication with the scope. An ^{55}Fe X-ray source emitting photons at 5.9 keV was used for the tests.

LabVIEW is a user friendly and powerful program for the control of digital instruments. The instruments can be cards that plug in the PC bus, and their control is directly through software, or instruments that use the General Purpose Interface Bus (GPIB), and their control is through a GPIB card on the PC. In the latter case LabVIEW controls the GPIB card, and this was the configuration we used. Programs for the communication with the scope were found on the Internet and were modified to suit our needs.

Figure 5.14 shows some typical events as seen on the scope, with the four channels connected to four adjacent anodes. The effect of the induced positive pulses can be seen on anodes next the anodes that were hit (negative pulses).

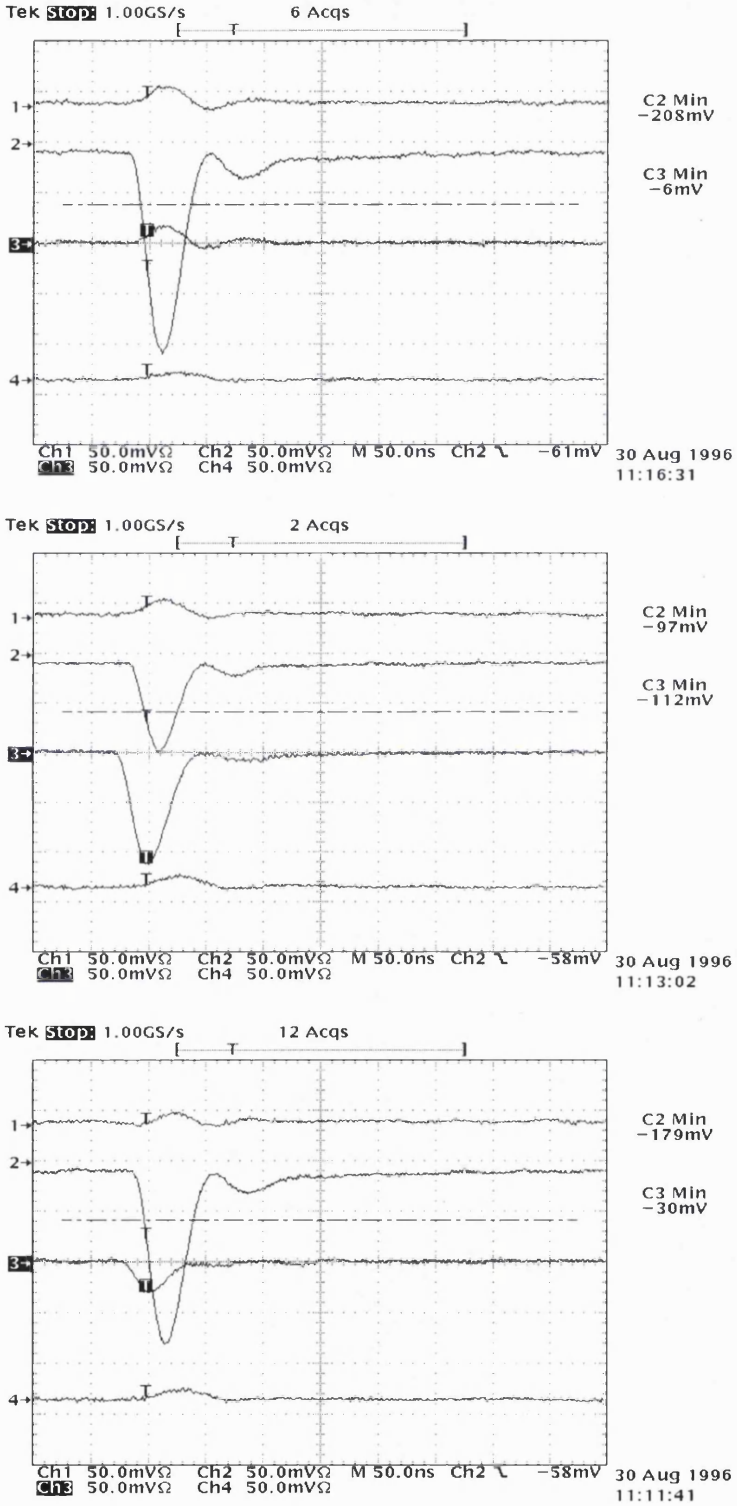

Figure 5.14: Three ^{55}Fe events as seen on the scope at UCL. The four traces come from four adjacent channels of the RAL MSGC

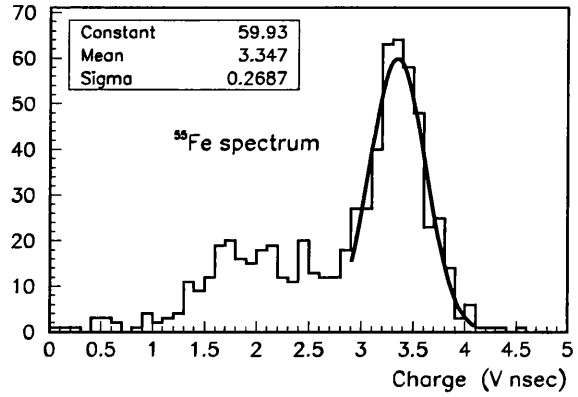

Figure 5.15: An ^{55}Fe spectrum collected by digitally adding the four scope channels that were connected on adjacent anodes.

The pulse heights of events that are spread over more than one anode are clearly smaller. This is because the total number of electrons is effectively constant and when they are shared between anodes the signal on each anode is not as big as in single anode events. Adding the pulse heights of the hit anodes together should give roughly the same result, depending on the energy resolution of the chamber.

An estimate of the energy resolution of the chamber was obtained by adding the pulse heights of all four channels, and found to be 19% (Figure 5.15). Channel 2 was set as the trigger channel, and after each event the pulse heights of all channels with a negative value were added together and stored on the disk. Only the channels with negative pulses were used because channels where no energy was deposited had positive values instead of zero due to the crosstalk. We were able to measure the energy resolution with only four channels because of the small range of photoelectrons produced with the ^{55}Fe source. Less than one out ten events spread out to three anodes, and only the very few of them that triggered channel 2 and spread to channel 1 and the next anode (not connected to the scope) could degrade the estimation of the energy resolution.

For higher energy X-rays a system with more channels was necessary in order to collect all the charge from the ionization cluster because of the longer range of

photoelectrons. The data acquisition system would also have to be fast to handle the high photon flux from an X-ray tube.

5.2.2 Data Acquisition Using a CAMAC ADC

After the preliminary exploration showed that the chamber was in good working order, another data acquisition system was used to provide more channels with faster readout. The set-up for the experiment is shown in Figure 5.16. Nine adjacent anodes were read out using the pre-amplifiers and post-amplifiers that were provided with the MSGC assembly. A CAMAC ADC (LeCroy 2249A) controlled by VME was used for the data acquisition. Eight of the anodes were each connected to an ADC channel through a delay of about 80 ns. The ninth anode, in the middle of the group, was connected to an analogue fan-out. One of the fan-out outputs was connected to the ADC through a delay while the other was connected directly to a discriminator and then to a timer which provided the gate for the ADC. Every time the discriminator was triggered all nine strips were read. The duration of the pulses from the chamber was about 80 ns (Figure 5.14) and the duration of the gate 150 ns.

Two different photon sources were used to provide a range of photon energies, the ^{55}Fe source and an X-ray tube with a copper anode. The spectrum of the X-ray tube was measured with a high purity germanium detector (made by EG&G) and is shown in Figure 5.17. The main features are the K_α and K_β lines of copper at 8.0 and 9.0 keV. The photons above 10 keV are produced via electron bremsstrahlung processes.The nominal energy resolution of the germanium detector is 470 eV at 60 keV. The FWHM of the two peaks is about 500 eV so the main contribution to the broadening of the peaks is the detector resolution.

In order to be able to select "whole" events, events in which all the charge deposited in the main ionization cluster was collected, a slit collimator was used

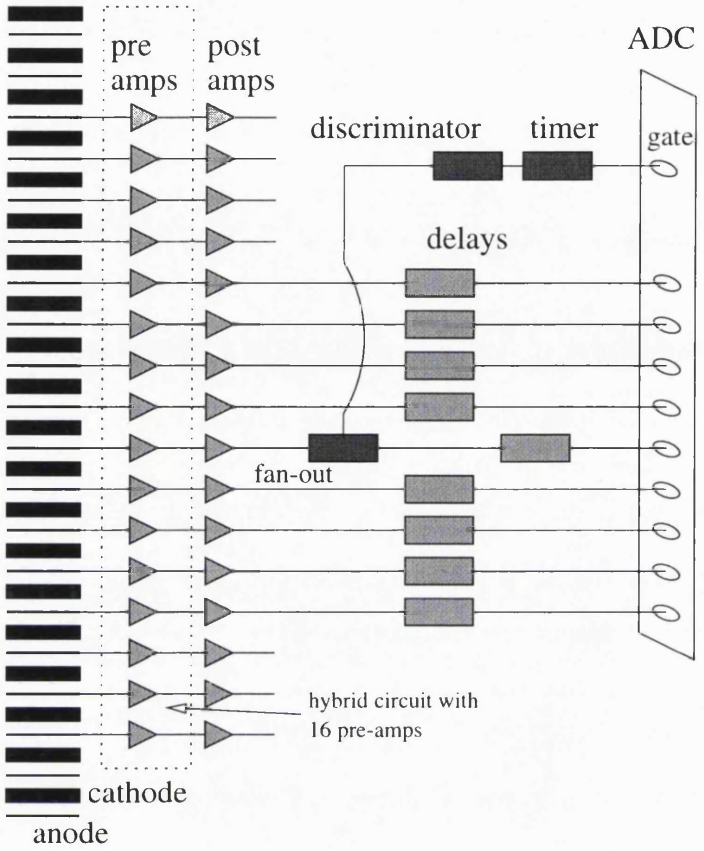

Figure 5.16: Experimental layout for data acquisition with a CAMAC ADC.

in combination with the X-ray tube. The slit was 80 μm wide, 2 mm long and aligned with the centre strip. The need for the slit arose from the fact that X-rays that converted away from the centre anode could still trigger the discriminator. The range of photoelectrons for 9 keV X-rays is about 0.8 mm at 1 bar and is sufficient to spread the signal to three or more anodes after diffusion, resulting in events where only part of the produced charge is collected. By only allowing photons to interact close to the centre strip, the simulation of the experiment became easier and more accurate. The length of the slit was chosen to be 2 mm to eliminate any errors caused by misalignment of the slit with the strips. (If the slit and the strips were not parallel the irradiated area would be wider than the width of the slit.) The accuracy in the alignment was better than 5°, giving a very small error in the irradiated area. The positioning of the slit in order to

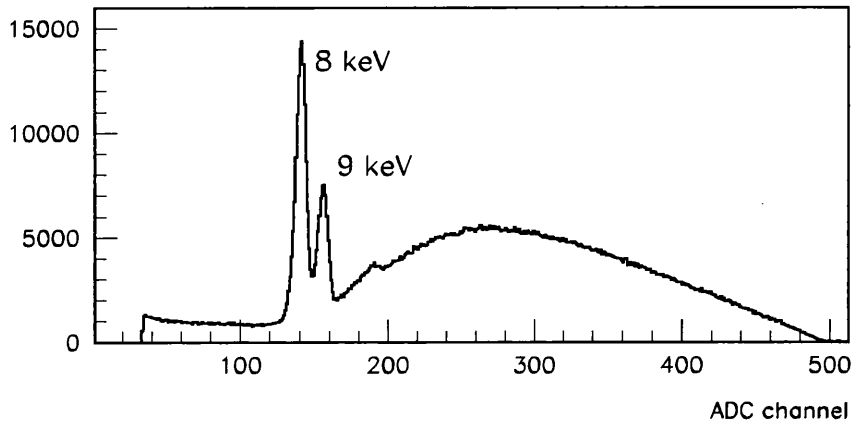

Figure 5.17: Spectrum of X-rays from the copper-anode tube.

be in front of the centre strip was done by counting the events on the anodes on either side of the centre strip and adjusting the slit until the number was roughly equal.

The use of a collimator was not necessary when the ^{55}Fe source was used. The discriminator was triggered only by X-ray photons that converted very close to the centre strip since the range for a 2.7 keV (5.9 – 3.2) electron in argon is about 0.2 mm. A narrow slit would also reduce the already low count rate and introduce problems associated with the very long times for data collection, like interference noise or drift of the chamber gain. The simulation of this experiment was simpler because of the small spread of charge in the detector.

In order to measure the pedestal of the ADC, and the noise levels, pulse heights were measured without a source while the discriminator was triggered randomly 1000 times. The results are shown in Figure 5.18. Small DC offsets in the output of the amplifier could change the pedestal of the ADC, so all the channels had to be measured separately. And since only one source with a line spectrum was available it was essential to measure the offset for the zero correctly. The sigma of the Gaussian fit to the histograms was used for the sampling of noise in the simulations. Channel 0 and channel 7 are obviously noisier than the other

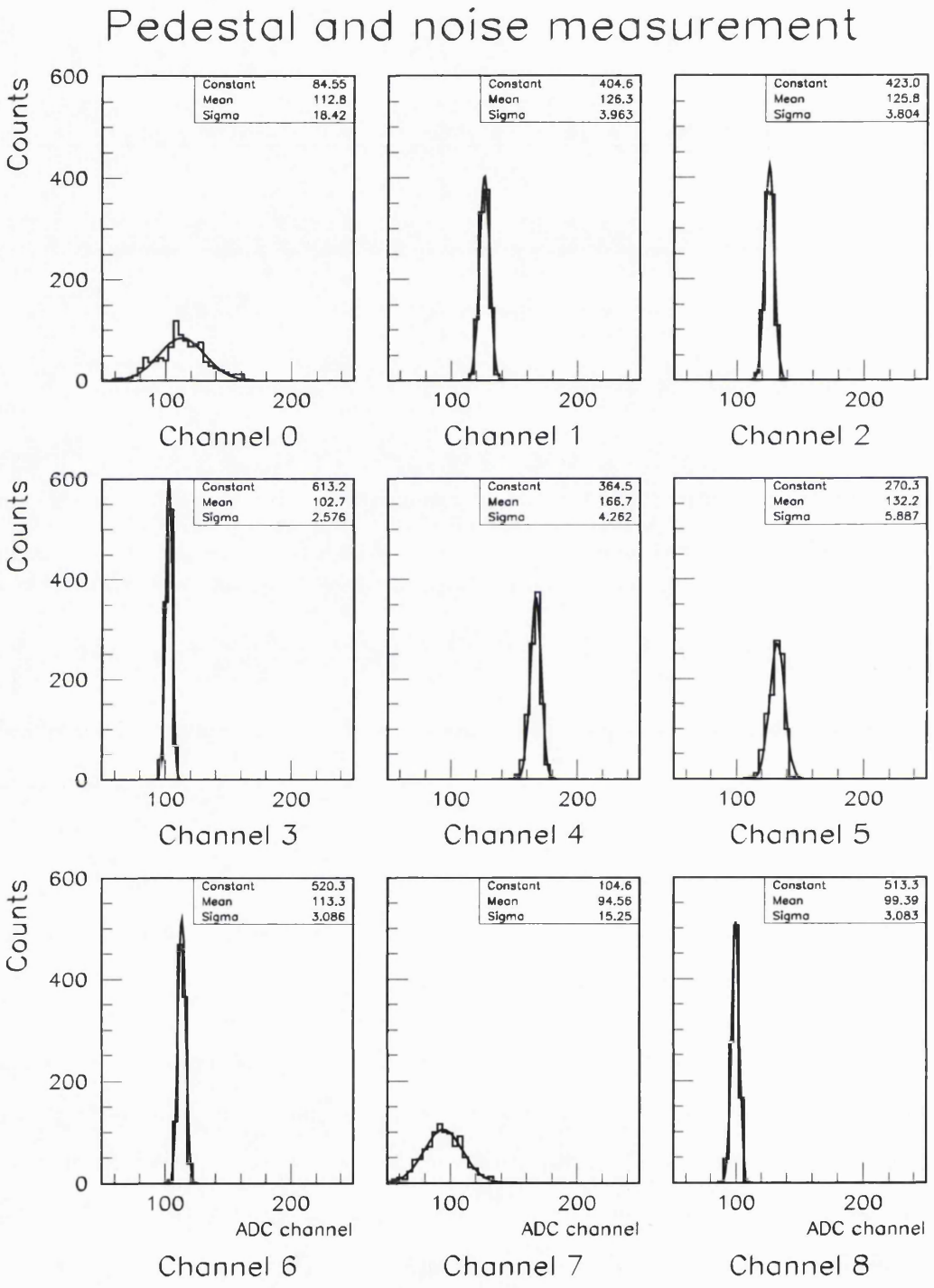

Figure 5.18: Pedestal and noise measurements for all the ADC channels.

channels, and the effect of the linear fan-out can be seen in channel 4 where the pedestal is somewhat shifted but no serious extra noise is introduced.

Uniformity of gain of the channels was also checked by applying a test pulse through a test input that was common for all channels. The test input was coupled to the input of each pre-amplifier through a separate 0.6 pF capacitor. Figure 5.19 shows the results after subtraction of the mean pedestal value. There are small differences of the order of 10% indicating different gains for different channels, but these differences could be due to variations in the values of the capacitors. A way to check if these variations were due to gain differences between channels is to calculate the energy resolution of the chamber with and without the corrections, because for energy resolution the values of all channels are added. The energy resolution of the detector with corrections for different gains was slightly worse than without corrections so it was assumed that the different gains were due to variations in the values of the capacitors.

Figures 5.20 and 5.21 show pulse heights on the nine channels after irradiating the chamber with X-rays from the ^{55}Fe source and the X-ray tube respectively. The mean pedestal value has been subtracted for all the channels. Channel 4 is the channel where the X-rays converted. The position of the "no signal" peak on the other channels is sightly negative due to induced pulses of opposite sign from the centre anode to the other anodes.

The first results with nine channel read-out gave an energy resolution for the chamber of 21% for 6 keV, which was worse than the energy resolution that had been measured with the 4-channel oscilloscope. It was important to identify the reason for this increase and eliminate its effects. The energy resolution of a detector is affected if any of the operational settings, like the voltage or the amount of quencher in the gas mixture, change with time. Changes of barometric pressure might also affect the gain by changing the ratio of main-gas/quencher. The rate from the ^{55}Fe source was slow (about 0.5 Hz), so a few hours of data

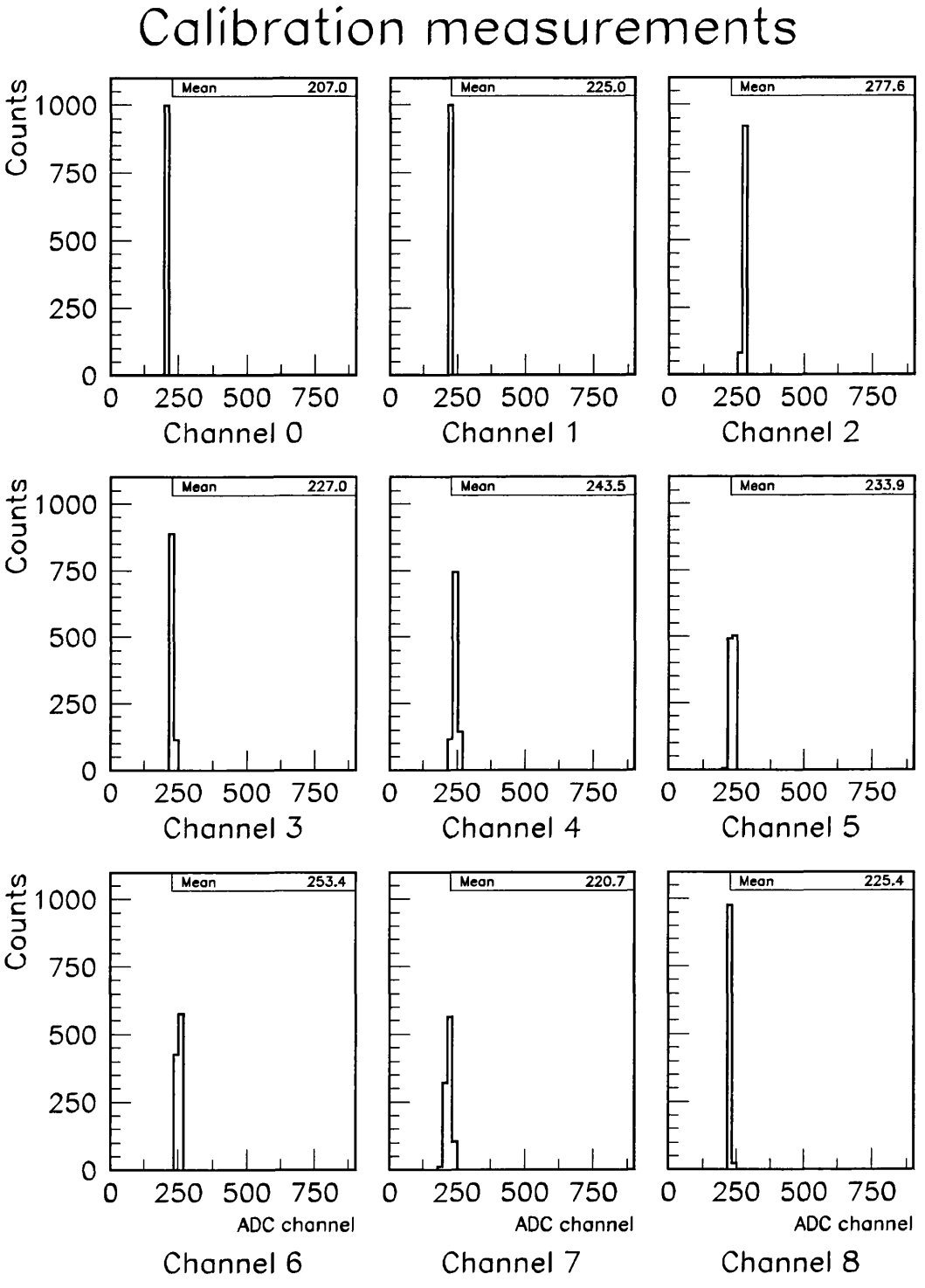

Figure 5.19: Test pulse measurements for gain variations between anodes.

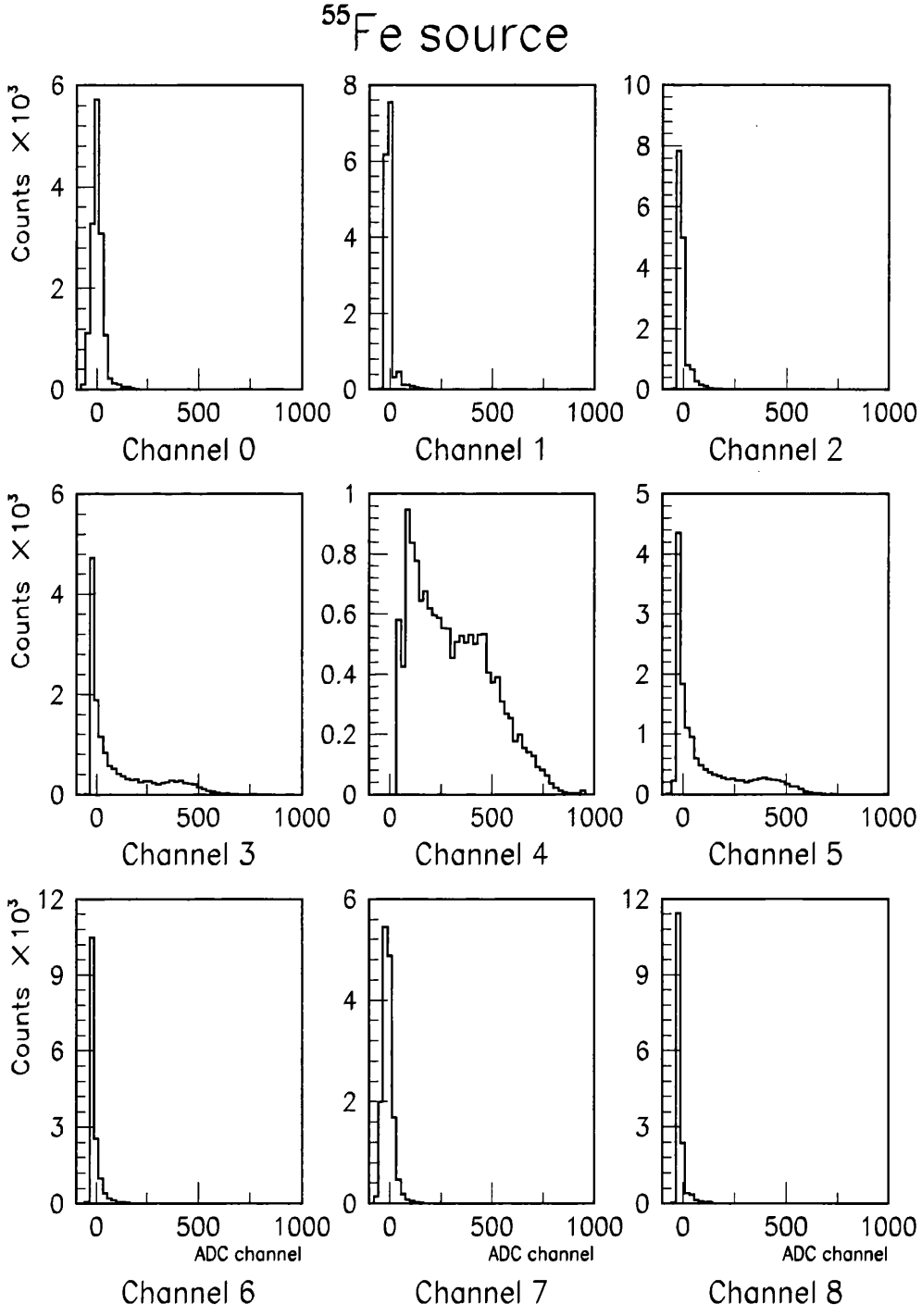

Figure 5.20: ^{55}Fe data from the nine ADC channels after subtraction of the mean pedestal value.

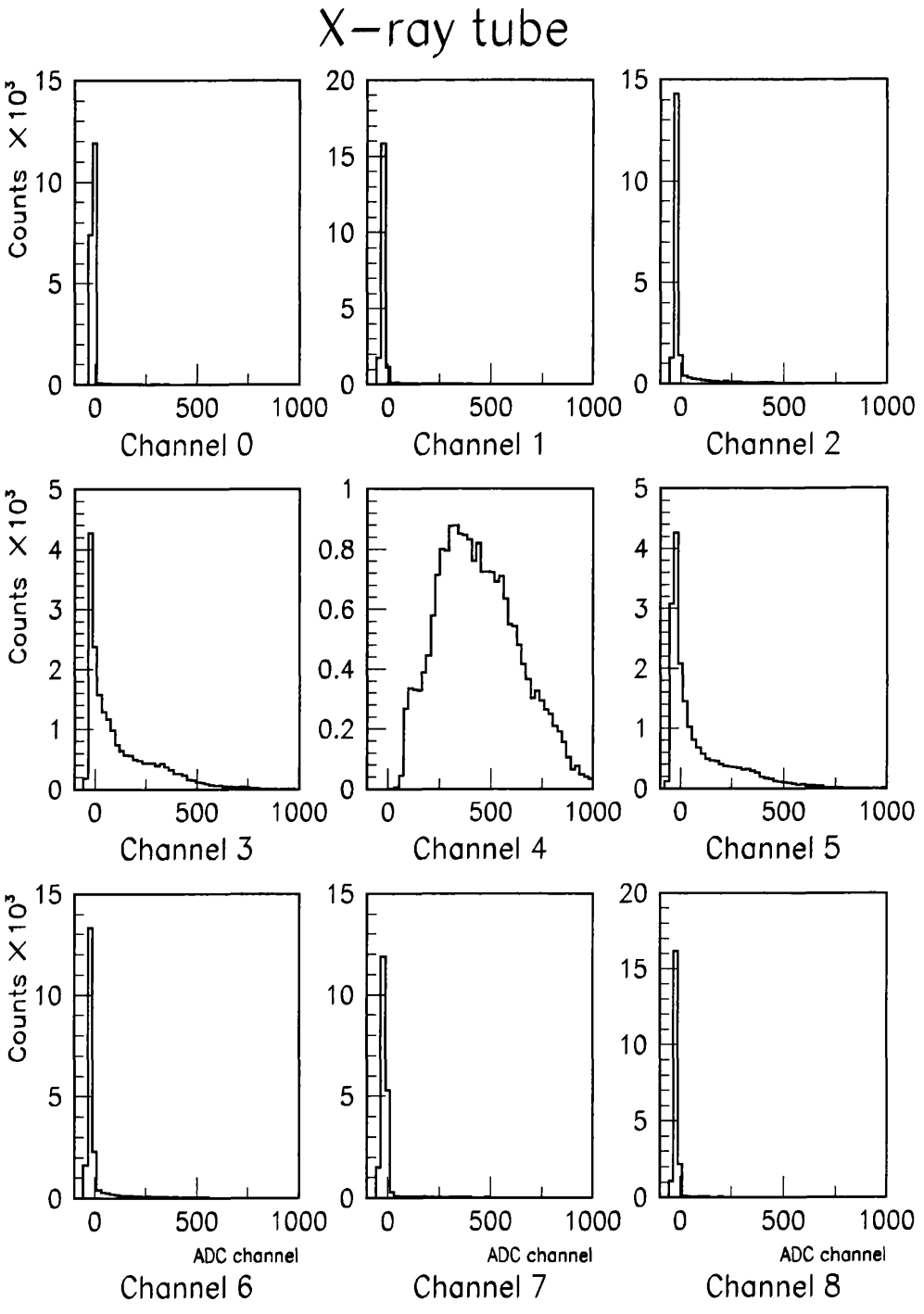

Figure 5.21: X-ray tube data from the nine ADC channels after subtraction of the mean pedestal value.

collection were necessary to get good statistics. In this time the gain of the chamber might change resulting in a worse energy resolution than the intrinsic resolution of the chamber. Small fluctuations of the order of 0.02–0.03 lt/hr had been observed in the readings of the flow meter controlling the isobutane in time periods of a few hours. It was decided to investigate.

5.2.3 Stability of Gain

First we looked at the possibility of changes of gain due to barometric pressure. The chamber was left to acquire data from the ^{55}Fe source for four days. Every event was recorded in a file. At the end of each day the number of events was divided into 24 groups one for each hour (about 1500 events). These groups were used to estimate the gain of the chamber for every hour and check if it was stable with time. With about 1500 events per group and for energy resolution of the order of 20% the statistical error on the calculation of gain is about 0.4%.

Information about the barometric pressure, for the same time period, was obtained from the Meteorological Office. The results are shown in Figure 5.22. It is obvious that there are gain fluctuations much bigger than the ones due to statistics. From the two graphs there seems to be no correlation between the change of gain and barometric pressure.

The linear correlation coefficient was also calculated. For a pair of quantities $(x_i, y_i), i = 1, \ldots, N$ the linear correlation coefficient r is given by the formula:

$$r = \frac{\sum_i (x_i - \overline{x})(y_i - \overline{y})}{\sqrt{\left(\sum_i (x_i - \overline{x})^2\right)\left(\sum_i (y_i - \overline{y})^2\right)}} \tag{5.2}$$

where, $\overline{x}, \overline{y}$ are the means of x_i and y_i respectively [39].

The value of r lies between -1 and 1, inclusive. It takes on a value of 1 when the data points lie on a perfect straight line with positive slope, with x and y

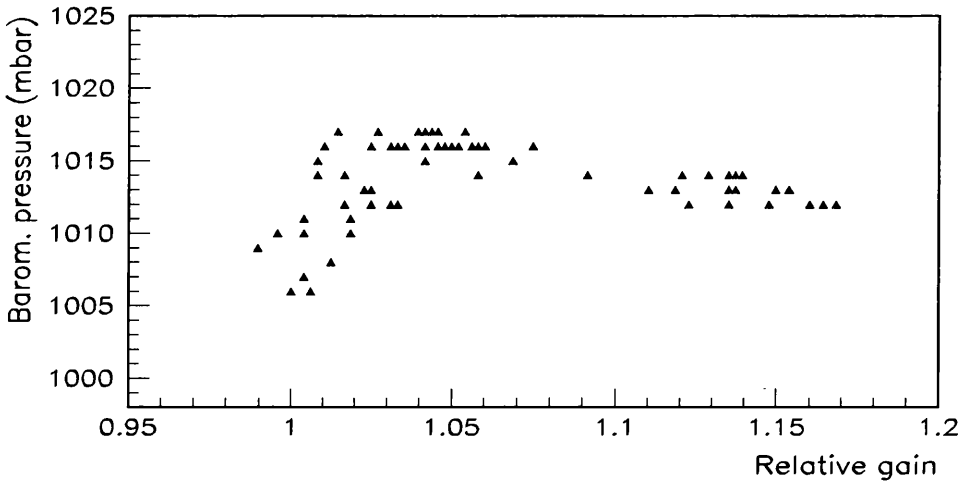

Figure 5.22: Barometric pressure versus gain.

increasing together. The value 1 holds independent of the magnitude of the slope. If the data points lie on a perfect straight line with negative slope, y decreasing as x increases, the r has the value -1. A value of r near zero indicates that the variables x and y are uncorrelated. The value of r for the set of points from gain and barometric pressure measurements was -0.04, which also indicates that there was no significant correlation.

A further 13 days of data were collected and various small changes in the operational settings of the detector were introduced to examine their effect on the gain variations. Fluctuations of about 0.1 lt/hr had been observed at random time intervals in the flow of the isobutane, and we wanted to examine whether they could affect the gain of the detector significantly. Figure 5.23 shows a plot of the relative gain versus time. The points marked with arrows correspond to the following changes of operational settings:

1. The flow of isobutane was changed from 0.4 to 0.5 lt/hour, keeping the argon flow constant. This change corresponded to about three times the fluctuations in the flow of isobutane that had been observed and resulted in a significant reduction of the gain.

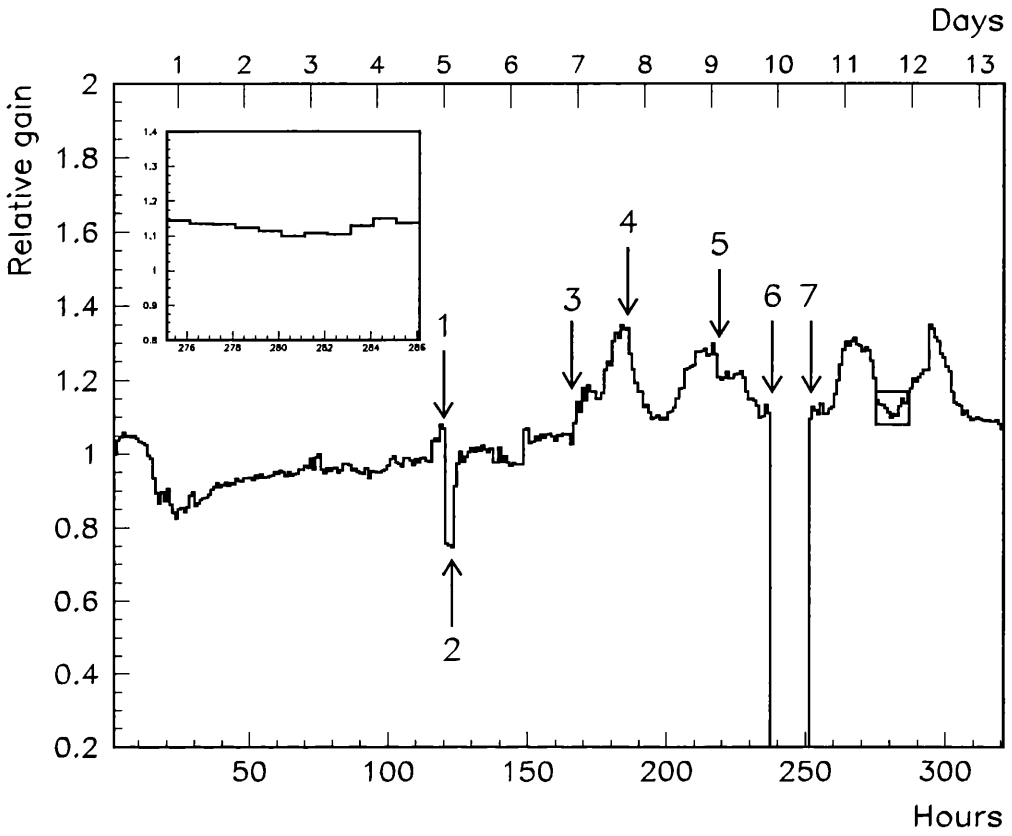

Figure 5.23: Gain fluctuations over a period of 13 days. The inset is a magnification of the small square from 275 to 286 hours.

2. The flow of isobutane was changed back to 0.4 lt/hour. The gain returned to a value close to the value before the first change was introduced. From these two actions it can be deduced that the small fluctuations in the isobutane flow that had been observed would have had a significant effect on the gain of the chamber.

3. The isobutane pressure was changed slightly. No immediate response was seen on the flow meter.

4. The isobutane flow had dropped to 0.3 lt/hour, probably due to the previous action. The pressure of the isobutane was increased slightly to compensate for that, and again no immediate response was seen on the flow meter.

Without changing the isobutane pressure regulator or flow-meter settings any further, the observed flow rate continue to oscillate, affecting the gain as can be seen in the graph.

5. The cathode voltage was reduced by 5 V resulting in a 5% change of gain.

6. The cathode voltage was reduced to 600 V.

7. The cathode voltage was restored to 670 V.

Looking at Figure 5.23 we see that there were significant changes in the gain of the detector over the period of 13 days. Comparing the variations in gain with the changes of the settings we can deduce that the main contribution was from the gas system. The small change in the flow meter settings at points 1 and 2 showed that the gain of the detector changes drastically with the amount of the isobutane quencher in the gas mixture. When small changes in the pressure regulator were introduced the system started to oscillate, affecting the gain of the chamber.

A system for digital mammography based on an MSGC would probably operate in a sealed box. This would save gas, as xenon is very expensive, and reduce the need for every-day maintenance. The MWPC of the SDRD operates in a closed box at 3 bar and a test image is taken at regular intervals to test whether the gas needs replacement.

The effect of fluctuations of the cathode voltage is investigated in item 5. The fluctuations were less than ± 1 V, so the contribution of the power supply to gain fluctuations was less than 1%. The time it takes the chamber to respond to a significant change of cathode voltage is examined in items 6 and 7. The chamber responds immediately (having a time scale of one hour) to a change of cathode voltage so it is expected to be in stable operation a few hours after powering up.

There was no prospect of acquiring a better stabilised gas system, but it

was observed that there were periods when the gain appeared to be sufficiently stable for good measurements. The inset in Figure 5.23 is a magnification of the small rectangle on the left side of the graph (time 275–286 hours). There are about 15000 events in this area with maximum change of gain ±1.5%. These events were used to produce all of the experimental results that were compared with the simulation.

5.2.4 Results

Every ADC channel contained a number proportional to the energy that was deposited in a strip 300 μm wide parallel to the anodes. Adding all the channels together gave the total energy that was deposited in the chamber per event. The only factor that had to be taken into account was cross-talk between the anodes. Every pulse on one of the anodes induced pulses of the opposite sign and the same size on the other anodes, with the result of lowering the signal. This not what would be expected from simple induction due to charge movements in the gas (the case for an MWPC). The opposite sign pulses apply equally to all the anodes within a single block of cathodes, which are connected to one another and to the high voltage through a common resistor. This effect is caused by the hit anode inducing a pulse in the neighbouring cathodes, which then induce pulses through the whole block of cathodes affecting all anodes in the group. With almost all the photons depositing most of their energy in the centre channel, the effect can be seen as the centre anode inducing pulses that lower the output on all the other anodes, as in Figure 5.20. This is the reason that the peaks of the histograms have slightly negative values. To compensate for this effect the values of every channel (except the centre one) were shifted until the main peak of the histogram would be at zero.

The ADC scale was converted to keV using the pedestal value for each channel as zero and the value of the ^{55}Fe peak as 5.9 keV. The energy spectra from

various anodes, and the multiplicity of hits (assuming a threshold of 1 keV) were simulated and compared with the experiment.

^{55}Fe source

The experimental results from the ^{55}Fe source are shown in Figure 5.24 together with the simulation results. The histograms on the left are the experimental measurements and the histograms on the right are calculated using our Monte-Carlo tools.

The energy resolution of the detector was measured by adding the values of channels 2–6 for every event and plotting the sum (Figure 5.24, top right). Adding 5 channels together proved sufficient to collect all the charge; adding more channels would only have added more noise. The FWHM measured from the full energy peak, was 19%, consistent with previous measurements (section 5.2.1).

As mentioned in the introduction, good energy resolution is not one of the main requirements for a detector for digital mammography. The energy resolution of the detector was measured and simulated purely for testing the accuracy of the simulation.

The initial result of the simulation for the energy resolution of the chamber was 12%. This value did not agree with our experimental results, but a literature search proved that it agreed well with published simulations and with other experiments. Bellazzini et al. [40], having fully simulated the electric field and the avalanche process in an MSGC, report an energy resolution of 12.7%. In experiments, the energy resolution of MSGCs appears to depend on the width of the anodes. An energy resolution of 11% was obtained by F. Angelini et al. [41] using a chamber with 3 μm anodes, while the resolution of chambers with 5 and 10 μm anodes has been worse. The most probable explanation for this effect is that the avalanche multiplication starts closer to the anode resulting in smaller

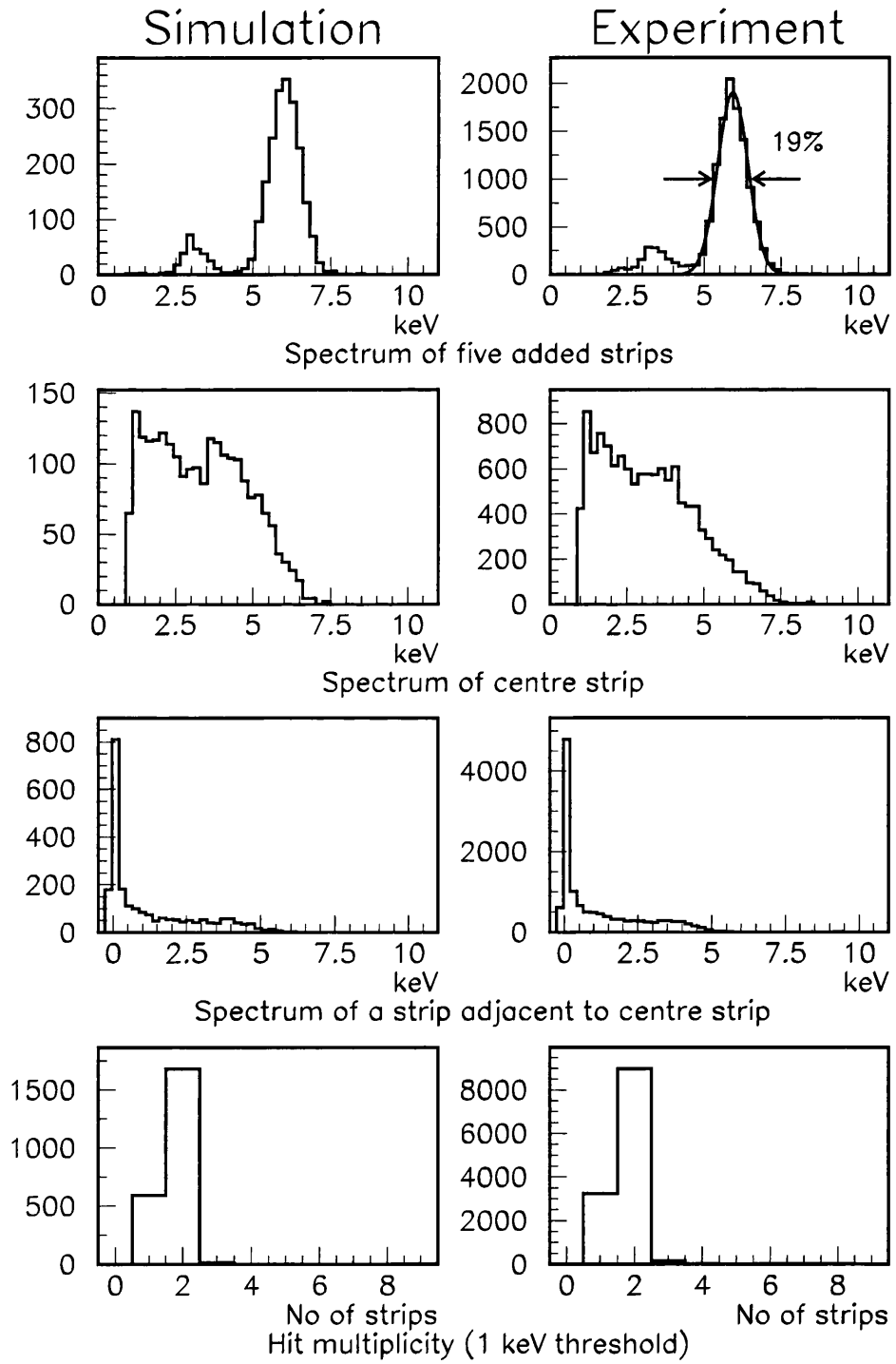

Figure 5.24: Comparison of experimental results and simulation for energy resolution, the spectrum of the centre anode, the spectrum of an anode adjacent to the centre and multiplicity of hits for 6 keV X-rays.

gain fluctuations.

In our simulation, there are two fundamental factors that degrade the energy resolution of the chamber, fluctuations of initial number of electron-ion pairs (section 2.2.3) and variation of gain according to the Polya distribution (section 3.3.2). However, the measured energy resolution of a chamber depends on many factors like the width of the anodes or imperfections introduced in the etching process. For these reasons, it was decided that the simulation was valid and that the particular detector has a rather poor energy resolution. To be able to compare the simulation with the experimental results extra gain variations were introduced. A simple, anode-width dependent adjustment, with Gaussian form, was added to the simulation of the gain fluctuations for each anode. It was set to give energy resolution of 19% for 10 μm anodes although it is not expected every chamber with the same anode width to have the same energy resolution. It is the only free parameter in the simulation of the Ar/isobutane filled MSGC.

The smaller peak at about 3 keV in the same histogram is the argon escape peak. Only 3 keV are deposited in the chamber because the emission of the photoelectron is followed by a fluorescence photon, which then escapes the chamber. The main peak corresponds to the more frequent process in which the primary photo-emission is followed by an Auger electron whose charge is also collected. The ratio of the number of events under the two peaks is the ratio of fluorescence to Auger emission. It has been simulated correctly by the ITS code without tuning.

The other histograms of Figure 5.24 allow us to compare the experimental data and the simulation of the spectrum from the centre anode, the spectrum from an anode adjacent to the centre, and the multiplicity of hits using a threshold of 1 keV (to be well above the noise levels). The width dependent correction to the gain fluctuations gives good simulation of the energy distributions on the single strips as well as the summed signal. The hit multiplicity was calculated

by counting how many adjacent anodes, including the centre anode, had energy content above 1 keV. The simulation results match the multiplicity of hits quite well.

X-ray tube

Pulse heights and hit multiplicities were also measured using the X-ray tube. The simulation of this experiment was slightly more difficult because the exact spectrum of the X-ray photons reaching the sensitive area of the detector was not known. The X-ray spectrum produced by the tube was measured (Figure 5.17)

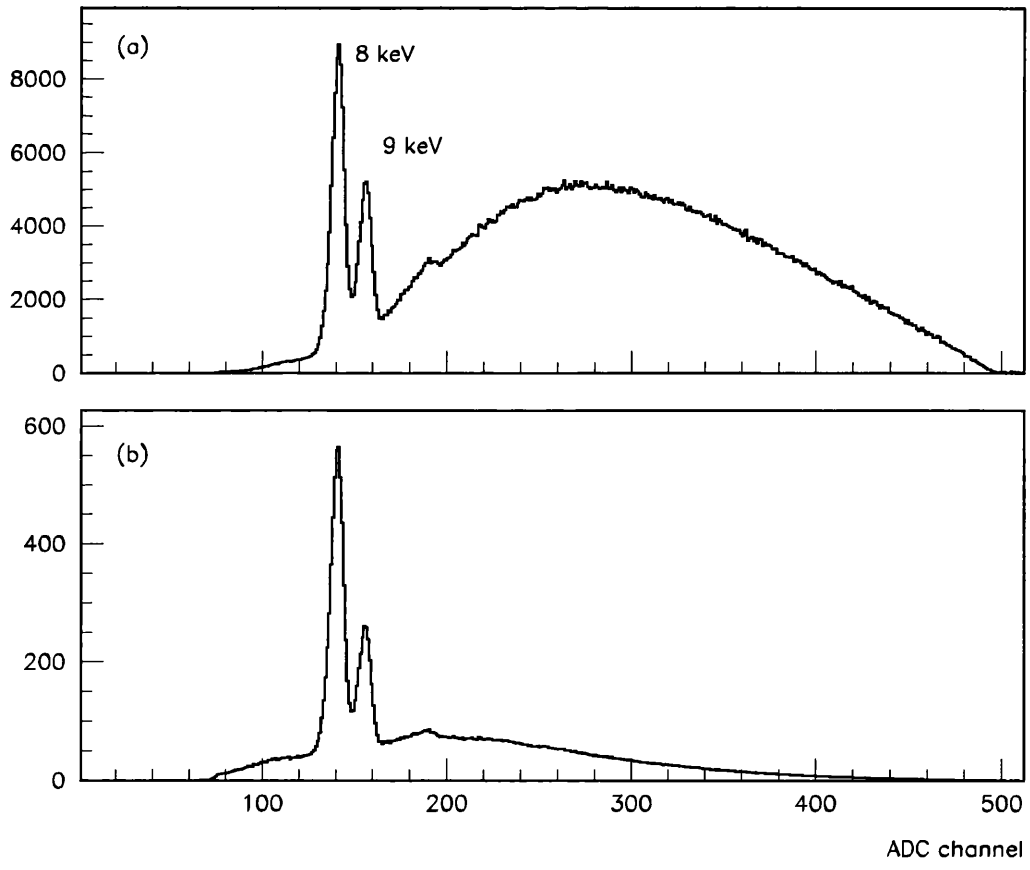

Figure 5.25: (a) Spectrum of X-rays reaching the sensitive area of the MSGC. (b) Calculated response from the MSGC, assuming an energy resolution similar to the germanium detector an full energy deposition in the chamber.

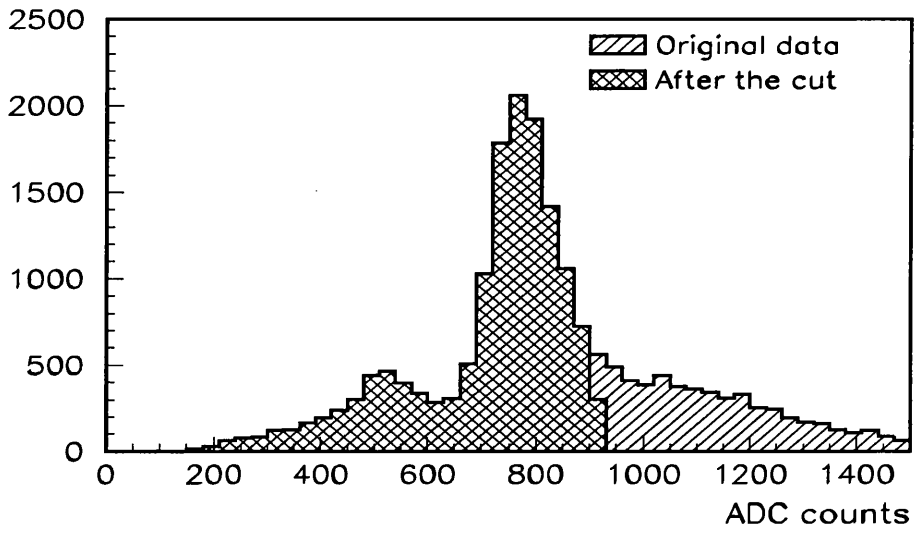

Figure 5.26: Full spectrum of X-rays from the X-ray tube (original data) and the part of the spectrum used for comparison with the simulation (after the cut).

but the photons had to pass through the 30 μm layer of mylar that sealed the chamber, and through the 250 μm aluminium drift cathode, so low energy X-rays were attenuated more. Figure 5.25a shows the calculated spectrum of X-rays that arrived at the sensitive area of the detector. The calculation was done using a simple convolution with energy dependent attenuation factors. Figure 5.25b shows the predicted spectrum from the MSGC if the energy resolution was equivalent to that of the germanium detector and the full photon energy was deposited. The calculation allows for the fact that the cross section for X-ray absorption in argon decreases with energy from 3 to 100 keV. Somewhat surprisingly, the attenuation of soft X-rays before they reach the chamber, together with the loss of hard X-rays which go through the chamber without converting, means that the broad spectrum of Figure 5.17 turns into a much narrower spectrum of Figure 5.25b with contributions almost entirely from the 8 and 9 keV peaks.

For that reason it was decided to use only 8 and 9 keV photons in the simulation (in different ratios), and correct the experimental data to match the simulation spectrum. A cut was applied to reject bremsstrahlung photons above 10 keV

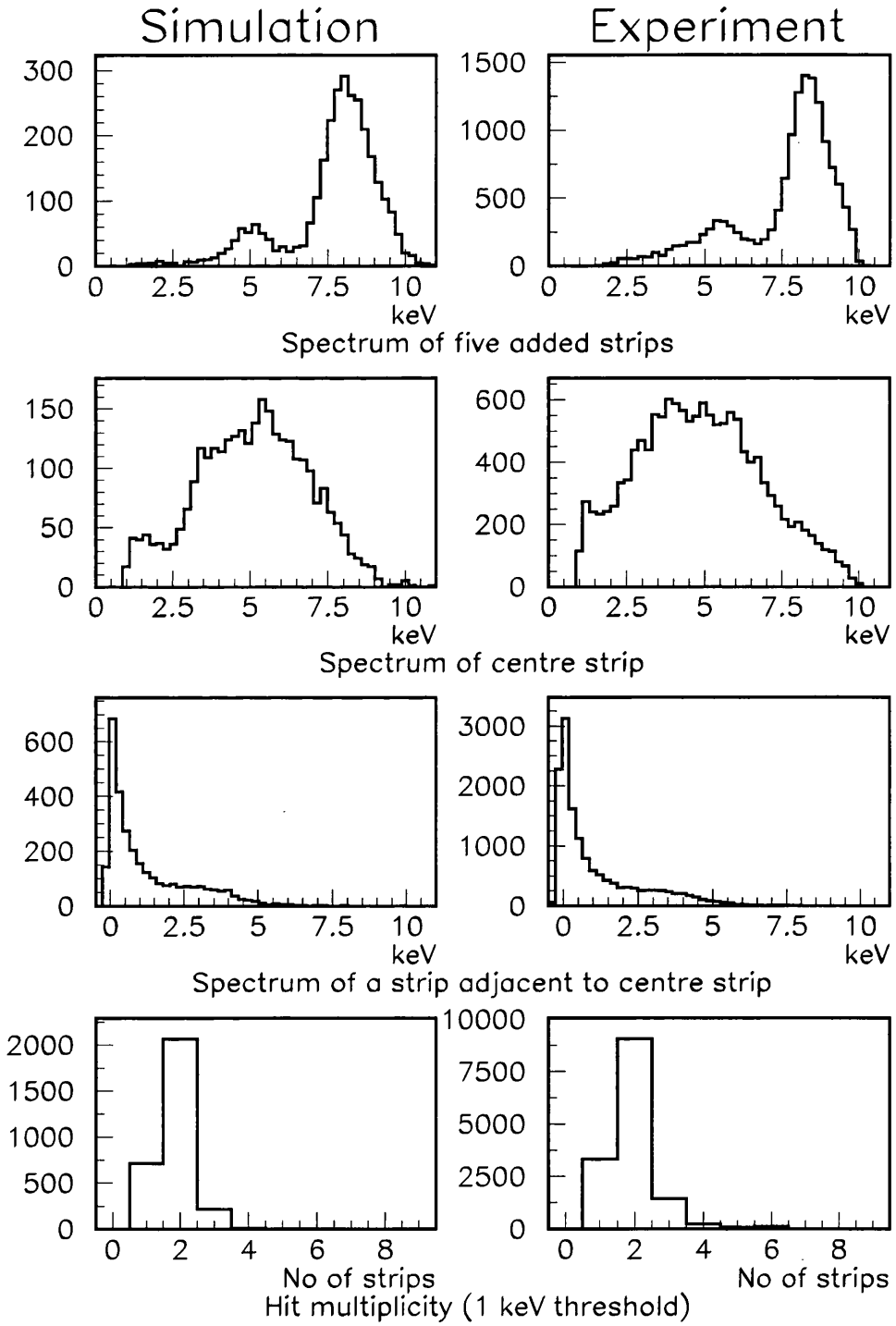

Figure 5.27: Comparison of experimental results and simulation for energy resolution, the spectrum of the centre anode, the spectrum of an anode adjacent to the middle and multiplicity of hits for X-rays from the X-ray tube.

(Figure 5.26) and only events passing the cut were used further in the analysis.

The experimental data and simulation results are shown in Figure 5.27. The reproduction of all the curves is very close, although there were no free parameters in the simulation. The energy resolution of the chamber was fixed from the measurements with the ^{55}Fe source (page 114). The curve showing the sum of five channels is now wider, since the energy resolution of the chamber is not sufficient to separate the 8 keV peak from the 9 keV peak.

The shape of the spectrum of the centre anode is different from that acquired with the ^{55}Fe source because of the slit collimator. The photons enter the detector very close to this anode and the probability of depositing most of their energy there is high, so the spectrum drops considerably below 2.5 keV. Due to the longer range of photoelectrons more energy is deposited in the strips adjacent to the centre compared with the ^{55}Fe data, and about 10% of the events give above 1 keV depositions in three anodes (bottom histogram).

5.3 Summary

A first series of experiments was performed at Novosibirsk for the evaluation of an MSGC as an X-ray detector. The results showed that resolution of 200 μm is possible at high pressure (5 bar or higher) and with a discriminator threshold above 6 keV.

The simulation model, described in the previous chapter, was used to simulate the experiments at Novosibirsk and gave similar results. Further experiments were done at UCL, using an Ar/iso-C_4H_{10} filled MSGC at atmospheric pressure, to provide more data that would be easily compared with the simulation. The model reproduced the experimental results well, having as the only free parameter the energy resolution of the chamber. These results are published in [42].

Chapter 6

Simulation of a Keystone MSGC

Although successful simulation of experiments implies good understanding of the physics involved, the power of the computer simulation does not stop there. Successful models can be used to predict results of future experiments with different parameters. In this chapter, the model described in Chapter 4 and tested in Chapter 5 is used to simulate the performance of a keystone MSGC in "tangential" geometry.

6.1 Description of the Planned System

A schematic diagram for the planned system can be seen in Figure 6.1. A slit collimator is used to make a very narrow, fan-shaped, X-ray beam. The X-rays go through the object to the detector, at about 1–2 mm above the microstrip tile. A second collimator can be used in front of the detector to reduce scattered radiation. Each anode is connected to an amplifier and a discriminator. Readout electronics as shown in Figure 1.5, would have to be used to either reject double hits or register them into separate channels. The device would operate in scanning mode, like the SDRD described in section 1.1.1.

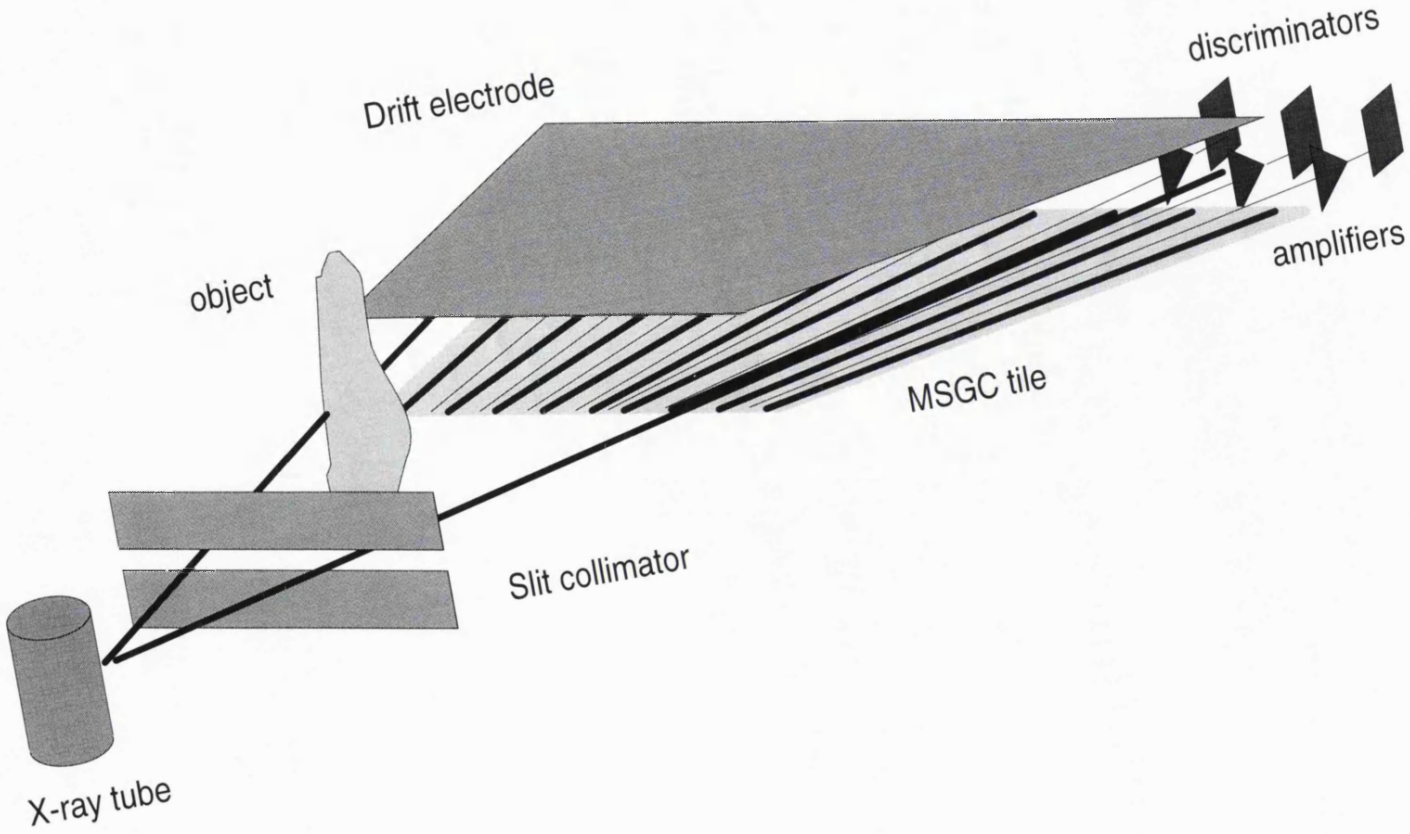

Figure 6.1: Schematic diagram of an imaging system based on a keystone MSGC.

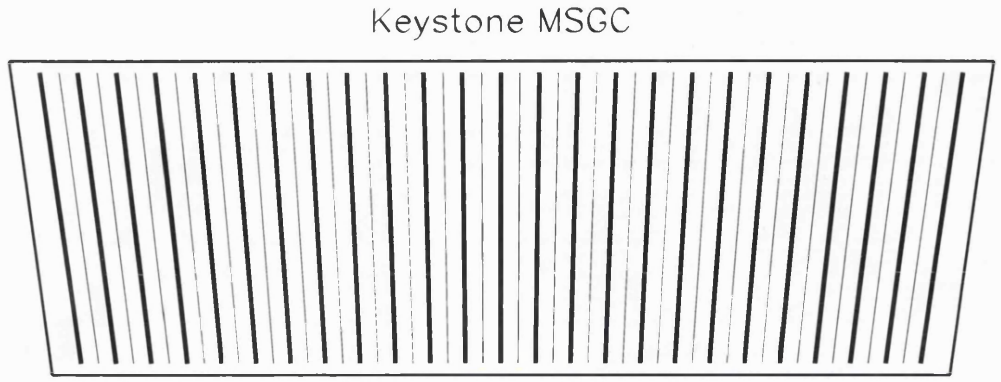

Figure 6.2: A keystone MSGC tile. The ratio of length to width is the same as it would be in the real detector, while the size of the strips as well as the distance between strips, has been exaggerated to make them visible. The real detector would have 825 anodes.

A prototype tile that would be suitable for mammography is shown in Figure 6.2. It is 5 cm long in the beam direction, 15 cm wide at the front and 16.5 cm at the back. The length of the strips is enough to stop 97% of 18 keV X-rays if the detector is filled with a xenon mixture at 5 bar. The angle of the strips is such that all the anodes point to a source 50 cm away. The pitch of the detector is 180 μm in the front and 200 μm in the back. If the detector is operated with coincidence logic the pixel size of the system would be 180 μm in the "standard" mode and 90 μm in the "high resolution" mode as defined for the SDRD (section 1.1.1).

An early problem associated with keystone tiles was non-uniformity of gain along the anodes due to the change of the anode-cathode distance. However the keystone geometry is important for many High Energy Physics applications so tiles of this type have already been studied. Snow et al. [43] have tested an MSGC prototype of keystone geometry with gain variations along the anodes of less than 3%. The length of the strips was 15 cm, all of them pointing to a source 85 cm away and the minimum detector pitch was 212.5 μm. The technique used to keep the gain constant was to change the cathode width from 68 to 85 μm.

6.2 Transfer Function Analysis

Transfer theory is commonly used to describe the relation between the input and output of a signal processing system. It has also been used successfully to describe imaging systems as a practical approach that predicts the degradation of an image for any given object [44]. Although what follows can be applied to any position sensitive detector, it has been written with an X-ray imaging detector in mind.

6.2.1 Definitions

An ideal position sensitive detector should image a point source of radiation as a single point. Such a detector of course does not exist and the intensity of an image of a point source at (x_1, y_1) is given by the Point Spread Function (PSF) $h(x, y)$, where (x, y) are detector coordinates [44]. Assuming that the detector is linear and space invariant, the PSF describes fully the properties of the detector. A linear detector is one for which, if there is more than one point source, each source will be imaged independently of the others. The resulting intensity distribution in the image will be the sum of all PSFs. This is the superposition principle of linear imaging systems. Space invariance implies that the shape of the PSF is the same, independent of the position of the source.

The PSF is usually not easy to determine directly, (though it can be easily simulated in a Monte-Carlo program because it is possible to generate large numbers of events at the same geometric point). The image intensity would have to be measured using a small aperture compared to the size of the PSF, which would result in a very small signal. Aligning the aperture with the centre of the distribution would also be very difficult. Some of these difficulties are avoided by measuring the Line Spread Function (LSF), which is the intensity distribution of an image of an infinitely long, infinitely narrow line.

There are cases when creating an approximation for an infinitely narrow line source—usually a very narrow slit collimator—is difficult. An equivalent method is to image a very sharp straight edge, by inserting an object like a block of a material with high absorption coefficient, in front of the detector. With this technique the detector is divided into an irradiated area and a non-irradiated area. The Edge Spread Function (ESF) is the detector response along a line which crosses the border of the two areas perpendicularly. The LSF can be calculated from the ESF by differentiation.

The FWHM of the LSF can be interpreted as the resolution of the detector since it represents the closest distance at which two parallel lines can be distinguished. It is a very useful number, but being a single number it does not give any information on the shape of the LSF. A more useful function that has been used to characterise the properties of detectors is the Modulation Transfer Function (MTF).

The MTF is defined as the modulus of the Fourier Transform of the LSF:

$$\mathrm{MTF}(\nu) = \left| \int_{-\infty}^{+\infty} \mathrm{LSF}(x) e^{-2\pi i \nu x} \, dx \right| \tag{6.1}$$

where ν is spatial frequency and x is distance. The LSF is a function in the space domain, while the MTF describes the response of the detector in the spatial frequency domain. The units most commonly used are mm^{-1} or the equivalent "line pairs per mm" (lp/mm). The higher the frequencies the detector can respond to, the higher its resolution. The frequency value of the MTF at 10% of its maximum is frequently used as a reference point. In Figure 6.3 there are some examples of analytical LSFs and their corresponding MTFs.

The MTF is usually normalised at 1 for spatial frequency 0 to allow easy comparison of different systems. For this reason, and because the Fourier transform is a linear operation, the MTF depends only on the shape of the LSF and not its exact values. Therefore, corrections on the pixel values that are done with a simple multiplication do not affect the MTF.

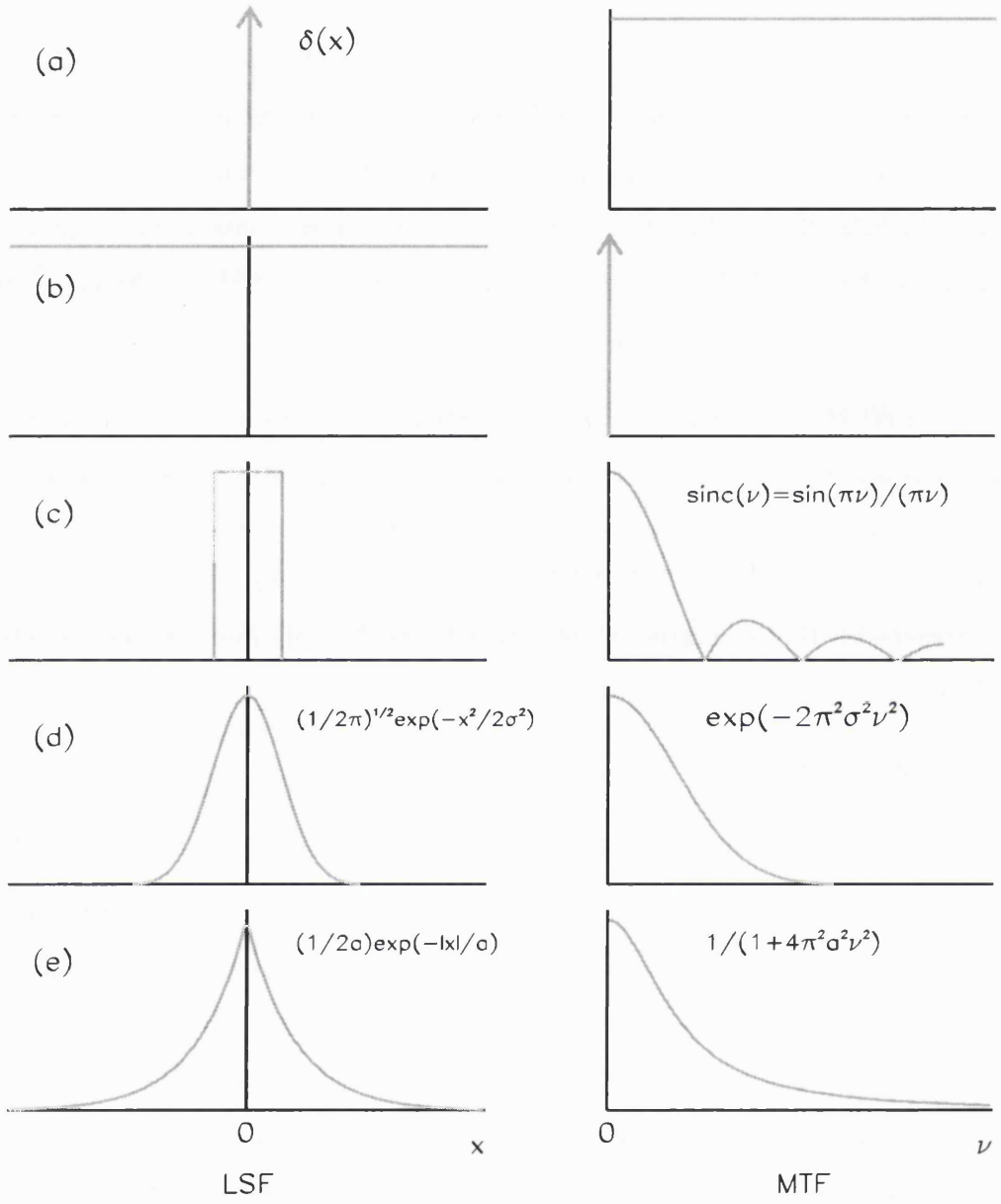

Figure 6.3: Some examples of analytical LSFs with the corresponding MTFs. Arrows represent δ-functions. If the LSF is a δ-function (a) then the MTF is 1 for all spatial frequencies, the perfect detector. On the other hand (b) if the LSF is flat the MTF is 0 for all frequencies except zero. The MTF of a square aperture (c) is given by the sinc function. More realistic examples are LSFs with Gaussian (d) or exponential form (e). For the Gaussian case the MTF is also Gaussian.

6.2.2 Numerical Methods

While the definition of the MTF is clear if the LSF is an analytic function, for real systems the LSF or ESF are *sampled* by measuring the detector signal at discrete intervals. In this case instead of a Fourier Transform (FT) a Discrete Fourier Transform (DFT) has to be performed [39]. The distance between the samples (Δ) is very important because according to the Nyquist theorem the maximum frequency that the transform can be calculated for is:

$$\nu_N = \frac{1}{2\Delta} \tag{6.2}$$

and is called the Nyquist frequency.

If a function is sampled at an interval Δ and does not contain frequencies higher than the Nyquist frequency ν_N, then the function is completely determined by its samples. But if the function contains frequencies higher than ν_N then the DFT will be inaccurate due to a phenomenon called *aliasing*. Any frequency component that is higher than ν_N is *aliased* (falsely translated) to frequencies lower than ν_N, by the very act of discrete sampling. In this case the function is *undersampled*, so care must be taken in the choice of the sampling interval Δ. If an MTF is not zero for frequencies higher than ν_N the function has been undersampled.

6.2.3 Digital Detectors

Digital detectors, by nature, are not spatially invariant devices because of the finite size of their pixels. Nevertheless, methods similar to the ones outlined above can be used to describe digital systems. They are also anisotropic because of the shape of the pixels. Pixels are usually square, so not all directions are equivalent. For that reason the analysis of their properties is done in two directions, horizontal and vertical, always perpendicular to the sides of the pixels.

Another interesting point is that the LSF or the ESF depends on the position of the line source or edge, specifically whether it is positioned in the middle of a pixel or between pixels. And because of the distance between pixels these functions are undersampled causing false estimates of the MTF due to aliasing.

A technique that is used to overcome the problem of undersampling is to position the slit or edge at a small angle ($> 2°$) to the direction perpendicular to the scanning direction used to derive the LSF or ESF [45, 46]. This provides a large number of different LSFs, one for every row of pixels. These LSFs can then be combined to form an LSF with much smaller sampling distance, known as the pre-sampling LSF.

An equivalent technique in case of one-dimensional detectors is a scan of a point source (or an edge) across the sensitive elements of the detector in uniform steps. A large number of LSFs is acquired for different positions of the source relative to the pixels (individual LSFs), which can then be averaged to give a pre-sampling LSF. Averaging the individual LSFs has to be done in a way that takes into account the source movement. This can be done by dividing each pixel into a number of sub-pixels equal to the number of samples taken per pixel. The average LSF can be calculated by first shifting each LSF to the direction opposite to the source movement by a number of sub-pixels, and then taking the average (Figure 6.4). In this way the sub-pixel that coincides with the position of the source is the same for all individual LSFs. The sampling distance is the step size of the source movement and may be made as small as needed. The LSFs presented in this chapter have all been averaged over relative positions.

Although taking the average seems a reasonable way of getting an oversampled LSF for the calculation of the MTF, the fact is that the resolution of a digital detector can be variable and it is generally worse when the point source is between pixels. This could affect the detectability of small details, especially if their size is smaller than the pixel size.

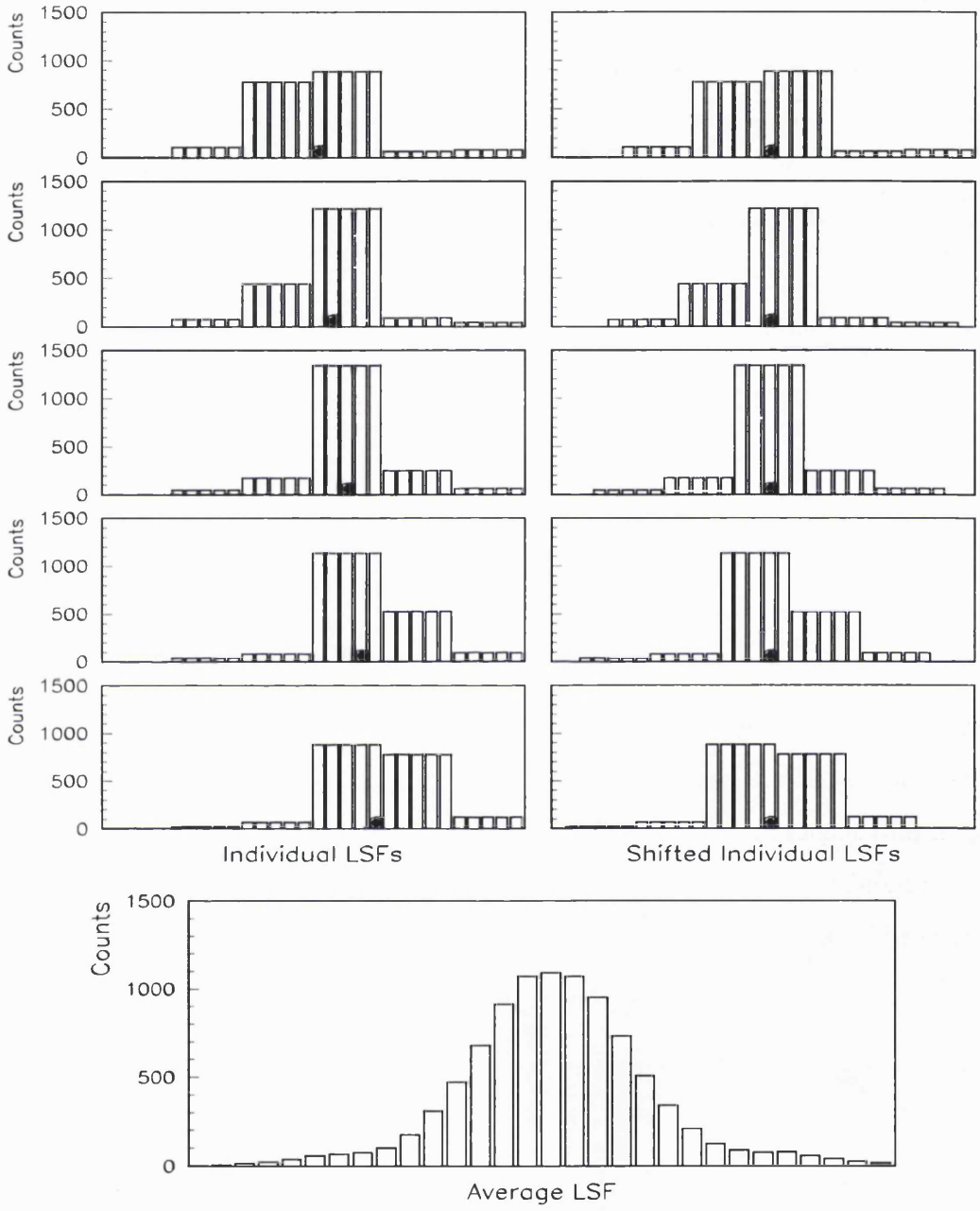

Figure 6.4: An example of taking the average of five LSFs taken at different positions of a point source relative to the pixels. The individual LSFs, divided into 5 sub-pixels per pixel, are shown on the left with the black circle marking the position of the source. The same individual LSFs are shown on the right after having been shifted to compensate for the source movement. The average LSF, shown at the bottom of the figure, has been calculated using the shifted LSFs.

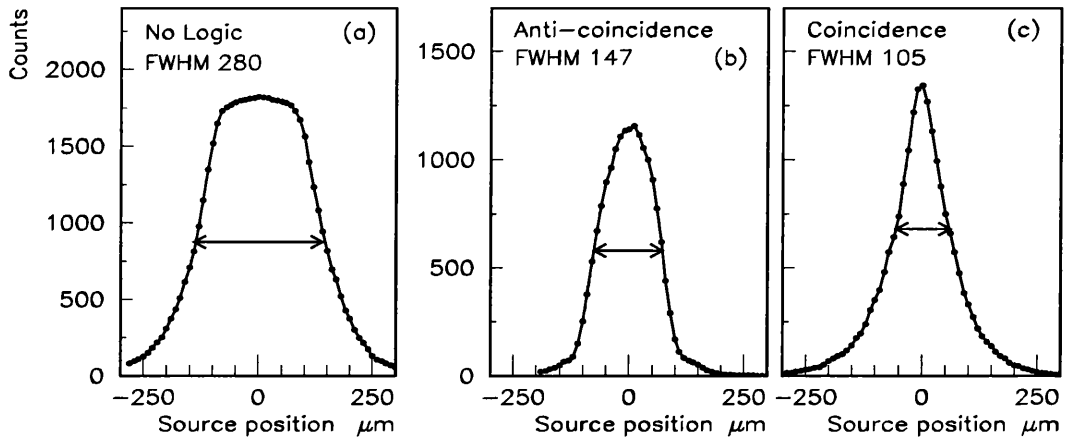

Figure 6.5: Channel response of a keystone MSGC with 200 μm pitch. From left to right: no logic used, anti-coincidence channel, coincidence channel.

6.3 Simulation Results

The resolution of an MSGC in "tangential" geometry was simulated for three modes of operation:

- No coincidence logic (Figure 6.5a).
- "Standard" (ST) mode; Coincidence logic with rejection of double hits (Figure 6.5b).
- "High resolution" (HR) mode; Coincidence logic with use of double hits in separate channels (Figure 6.5b and c).

The response of one channel while a point source is scanned across the detector is shown in Figure 6.5 for the three operation modes, detector pitch 200 μm and threshold 3 keV. The resolution of the detector in the mode without coincidence logic was not expected to be significantly different from the experimental results of section 5.1.3 since the conditions are almost identical. The response of the

channels in the two coincidence modes is much narrower as expected. These two modes will be examined in detail in the following section.

Figure 6.6 shows the response from three adjacent channels of the SDRD in HR operation mode [6]. The first and third channels are anti-coincidence channels and the channel in the middle is a coincidence channel. Although the detector is an MWPC with 1.2 mm pitch, there is a certain similarity in the shape of the curves for coincidence and anti-coincidence channels to the simulations in Figure 6.5. This reinforces our faith in the reliability of the simulation.

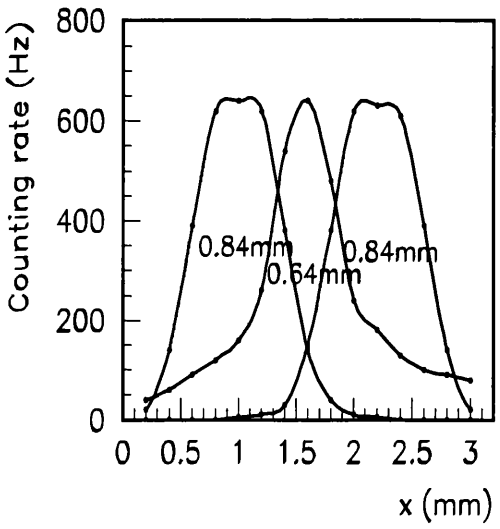

Figure 6.6: Resolution of the HR mode of the SDRD described in section 1.1.1. The first and third curves are from single hit channels. The middle curve is from the coincidence channel in between. The FWHM of the curves is shown [6].

Another reason that makes coincidence logic a more attractive option than simple discrimination is the ability of the detector to perform at lower pressure. High pressure is needed to prevent charge from spreading to more than one channels, but with coincidence logic events that trigger two anodes are as useful as single events.

6.3.1 Study of the Effect of Keystone Geometry

In the simulation of the "perpendicular" geometry, as mentioned in Chapter 3 the strips were parallel so the division of the volume of the detector in zones was necessary only in two dimensions. Only the distance between the conversion point of the X-ray photon and the anode is important and not the exact position

of the conversion along the anode.

In the "tangential" geometry with a keystone MSGC tile, the pitch of the detector changes along the anodes. A complete simulation of this geometry would include information about the exact position of the conversion in three-dimensions. But in order to simulate the energy deposition in three dimensions the detector volume would have to be divided in cubes with dimensions around 50 μm. This, even for a small detector volume, would have required inordinately large workstation memory.

However, the change in the pitch from front to back of a detector whose strips point to a source 50 cm away is quite small. If 200 μm is chosen to be the biggest distance between anodes at the back of the detector then the distance between the anodes at the front would be 180 μm. A test of the effect of the varying pitch on the resolution of the detector was done by comparing the LSF of detectors with parallel strips and a pitch of 180, 190 and 200 μm. The results can be seen in Figure 6.7. The gas pressure was 5 bar, the threshold 3 keV and the beam entered the detector 2 mm above the microstrip tile. The 3 keV threshold was chosen so that both channel types will count the same number of hits. If a different threshold is chosen then a weighting factor will have to be used to compensate for the difference in counts between the two channel types.

The FWHM of the LSF for a detector with pitch 190 μm in Figure 6.7 is the average of the FWHM of the LSFs of the other two detectors for both the HR and ST modes. This allows us to predict the resolution of any point along the anodes of a keystone tile by simple interpolation. Although more photons stop in the first half of the detector, for all practical purposes the resolution of a keystone MSGC with an increase of pitch of 10% between the front and the back can be approximated with the resolution of a detector with parallel strips and pitch equal to the average between the minimum and maximum pitch. For the rest of the analysis the curves that correspond to a detector pitch of 190 μm will be used as

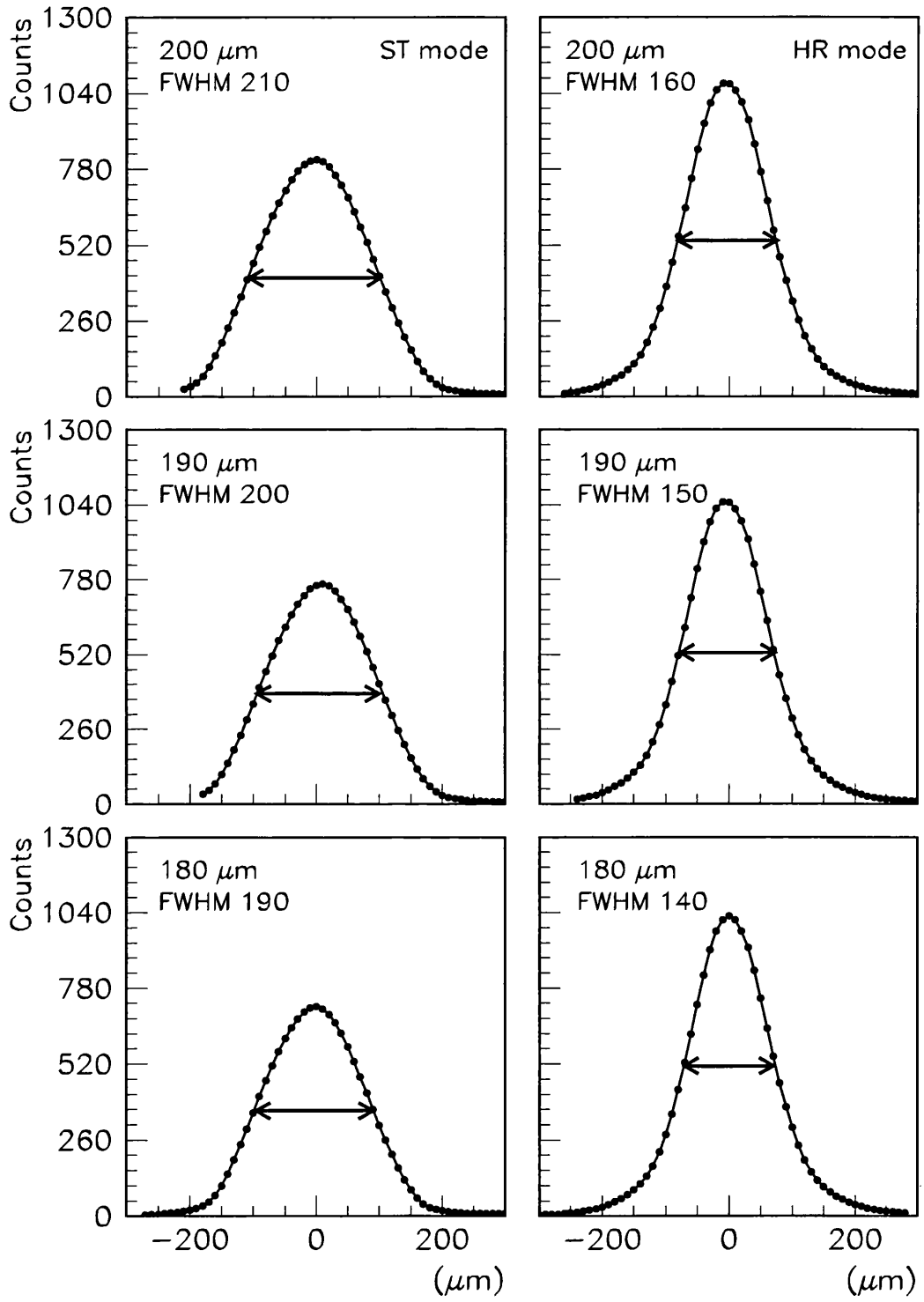

Figure 6.7: Simulation of the LSF of MSGCs with parallel strips in "tangential" geometry for detector pitch of 180, 190 and 200 μm.

the response of the whole keystone tile. The small reduction in efficiency (fewer photon counts), evident in the ST mode, is due to the increased probability of coincidence hits as the width of the channels gets smaller.

6.3.2 Calculation of the MTF

Having established that the resolution in the middle of the detector is a reasonable approximation to the resolution of the detector as a whole, we proceeded with the calculation of the Modulation Transfer Function. The curves in the middle of Figure 6.7 were used for the calculation. The DFT was performed using a subroutine of LabVIEW. The MTF for both the ST and HR modes can be seen in Figure 6.8. As expected from the shapes of the LSFs, the MTF for each mode is different. The HR mode. having smaller pixel size has a resolution of 6.5 mm^{-1} (at MTF = 0.1) while the resolution of the ST mode is 4.5 mm^{-1}. The distance between the samples of the LSF is 10 μm, so the Nyquist frequency for the MTF is 50 mm^{-1}. The MTF for both channels reaches zero before 15 mm^{-1}, so there are no errors due to aliasing.

The MTFs of detectors with LSFs of Gaussian form and FWHM 100 and 200 μm are also plotted in Figure 6.8. Comparison between the differences of the MTFs of the ST mode and the Gaussian 200 μm case shows how misleading the FWHM of the LSF can be, if the shape of the curve is not taken into consideration as well. Although both LSFs have the same FWHM, the MTF of the ST mode is clearly superior because the curve of the LSF does not have the extended tails of a Gaussian. The HR mode, with 100 μm pixels, has clearly worse resolution than a typical detector with resolution 100 μm.

Another major difference between the two modes is their efficiency. Figure 6.9 shows how the efficiency of the detector for photons converted in its active area varies across the strips for the two modes. In the HR mode the efficiency is

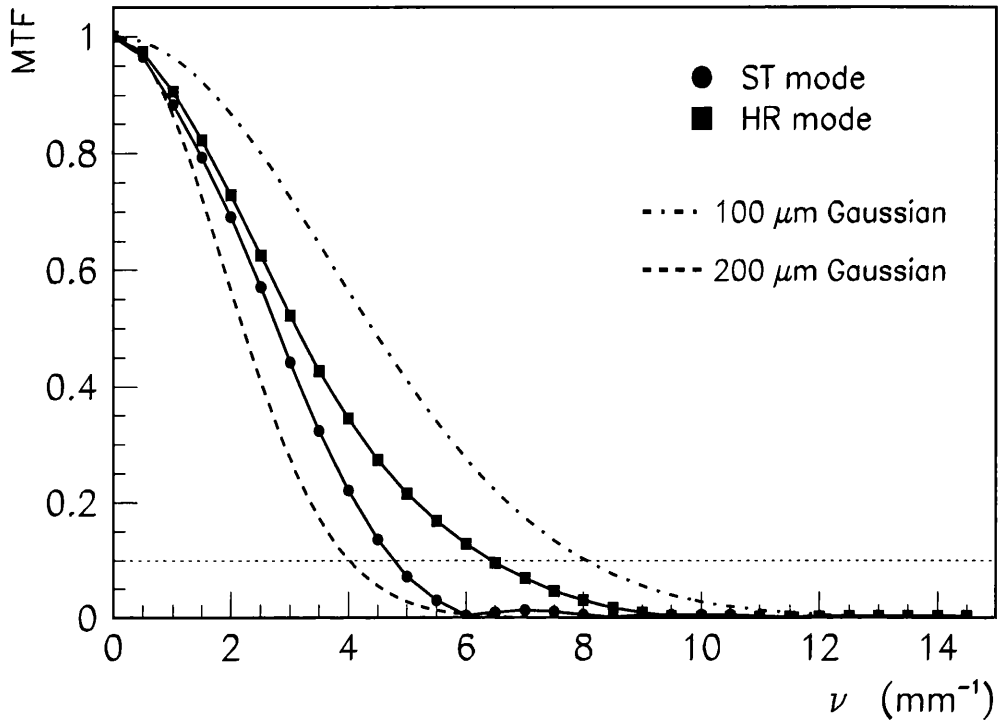

Figure 6.8: The MTF of a 190 μm MSGC operating in ST or HR mode compared with the MTF of detectors with Gaussian LSF with FWHM of 100 or 200 m.

essentially uniform and equal to 100%. (It appears from Figure 6.9 that the HR mode can sometimes exceed very slightly 100% efficiency. This is due to the few events in which 3 channels are hit giving two apparent hits from a single event. There is no significant effect on the argument given here.) In the ST mode it is significantly below 100% and very non-uniform.

Figure 6.10 gives a simple illustration of the different performance of the two modes. It shows the simulation of the response of the MSGC in "tangential" geometry to uniform irradiation from a parallel X-ray beam. In front of the detector there are three small high contrast objects—actually three 30μm gaps in the beam—at different positions with respect to the strips. The first object (from left to right) is half way between strips, the second in the middle of a strip

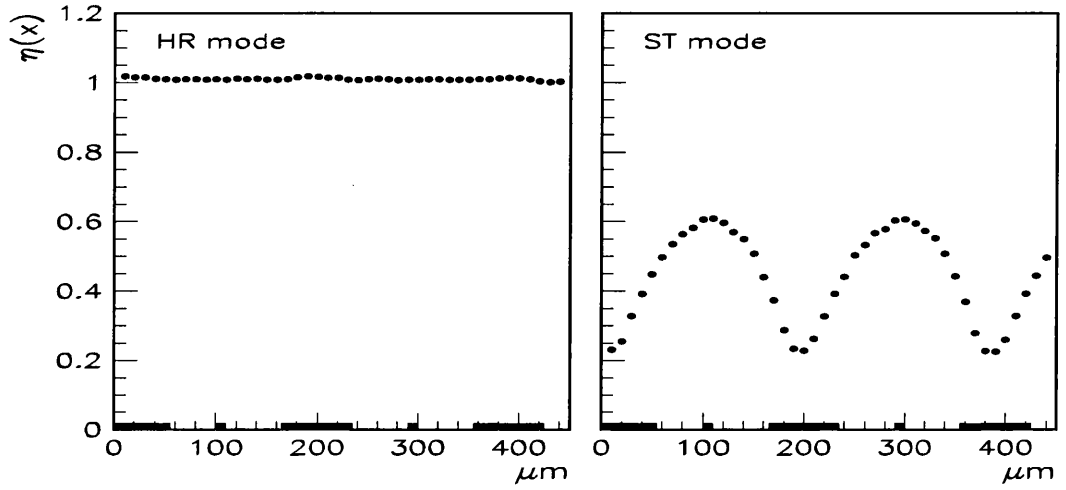

Figure 6.9: Efficiency of MSGC for the two modes that use coincidence logic. The strip pitch is 190 μm in both cases.

and the third at an intermediate position. The first object can be seen clearly in the HR mode, but is almost invisible in the ST mode. This is because half way between strips the efficiency of the detector is smaller, so the contribution of this point to the formation of the image is not so significant. In the HR mode, where the efficiency is constant, the object is visible. The middle object is visible in both modes because at the middle of a strip the efficiency of the ST mode is maximum. Between these two cases is the third object. It can be seen, but not as clearly as the second since it is at a point with lower than maximum efficiency.

6.3.3 Summary of Results

In a keystone MSGC the pitch of the detector varies along the strips. This effect was studied by comparing the simulated resolution of detectors with 180, 190 and 200 μm. The results show that for strips pointing to a source more than 50 cm away the detector performance is equivalent to the performance of a detector with parallel strips and a pitch equal to the anode pitch half way between the front

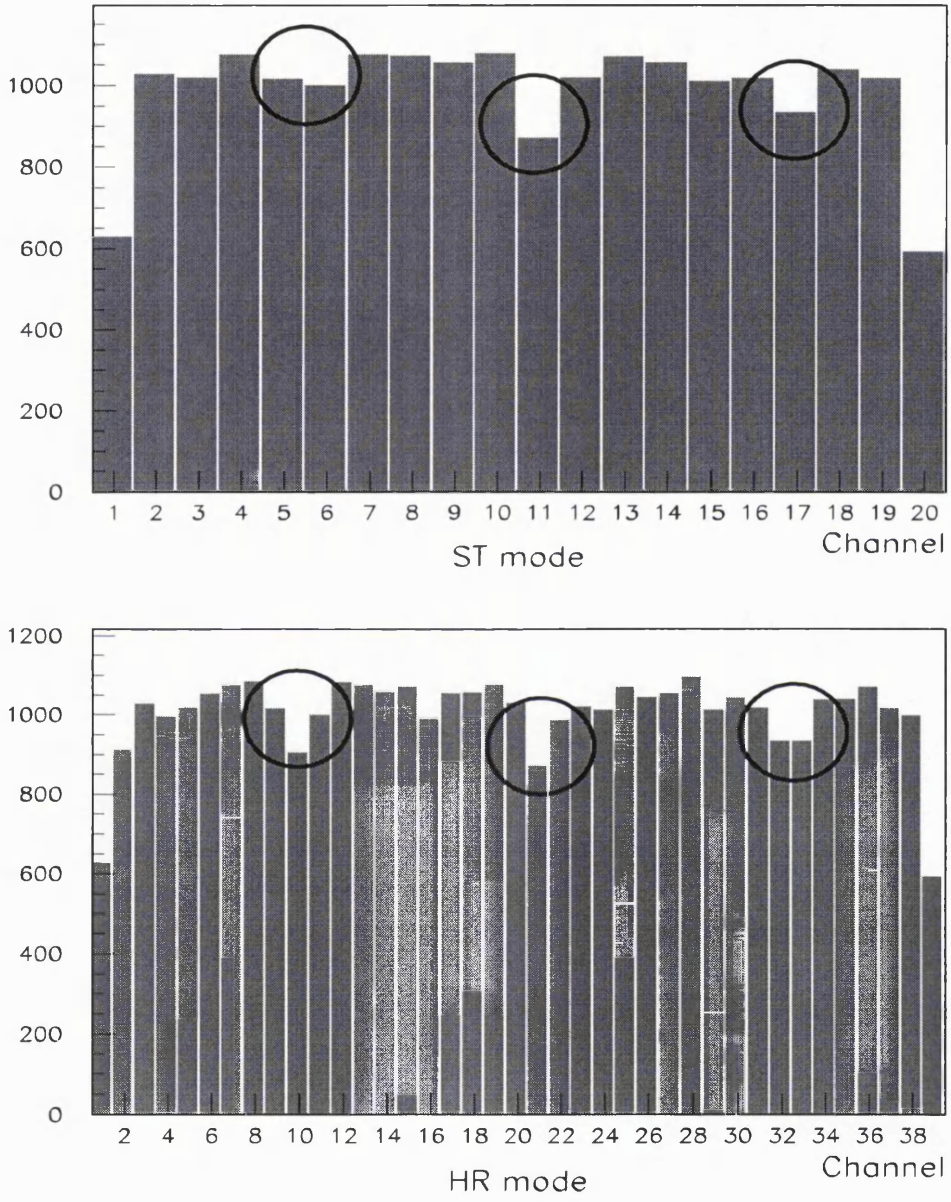

Figure 6.10: Simulated detection of three small objects in either ST or HR mode at different positions with respect to the detector strips. Although the objects have the same size, they appear with different intensities (or not at all) in the ST mode because of the non-uniform efficiency of the detector across the strips.

and the back of the keystone tile.

The use of coincidence logic can improve the resolution of the detector significantly. Simulations and experiments (Chapter 5) have shown that with simple discrimination the resolution of a 190 μm pitch MSGC is around 280 μm (3 keV threshold). Simulations of the same detector using coincidence logic showed that resolution can be below 150 μm (HR mode).

There are two different modes of coincidence logic, rejection (ST mode) or use of double hits (HR mode). The pixel size for the HR mode is half of that of the ST mode. The MTF was simulated for both modes and was found to be (at MTF = 0.1) 4.5 mm^{-1} for the ST mode and 6.5 mm^{-1} for the HR mode. A major difference in the efficiency was also evident in the simulation, with the ST mode having much lower and non-uniform efficiency compared with the HR mode.

6.4 Possible Problems in the Realisation of the System

There are two easily identifiable problems in the construction of a system based on an MSGC for digital mammography: insufficient X-ray flux and decrease of the quantum efficiency due to dead areas in the gas at the detector entrance.

The problem of the insufficient X-ray flux arises because of the slit. Only a very small part of the solid angle and of the X-ray flux is used. If the area covered is 15 $\times$ 15 cm^2 and the pixel size 100 $\times$ 100 μm^2 1500 line scans are needed. In order to limit the time for scanning the whole image to below 5 s, the integration time for each line must be 3 ms. Experience from the SDRD has shown that about 5000 counts per pixel are necessary to get sufficient picture quality. This leads to a total flux of 1.66×10^8 photons/mm/s at 50 cm. This X-ray flux corresponds to a count rate of about 2.5 MHz/channel. Keeping in mind that the current rate

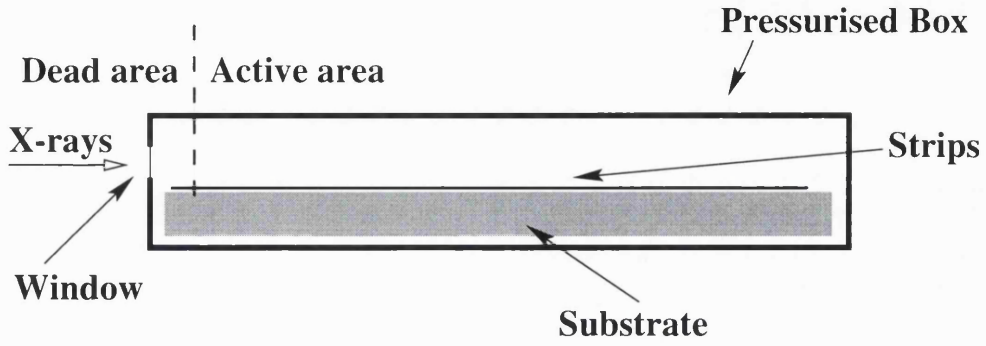

Figure 6.11: Schematic layout of the arrangement of an MSGC tile inside a pressure box.

limit of MSGCs is about 1 MHz/mm^2, a rate of 2.5 MHz/anode should not create a problem.

A molybdenum tube, in order to provide the necessary X-ray flux, would have to operate at 50 kV and 40 mA for 5 s. This is within the maximum load of the very latest molybdenum tubes [47]. Some R & D would be required to match such a tube to the needs of a low cost MSGC based system.

If more than one detector was integrated onto a rigid gantry, each one with its own slit and each one scanning only part of the total area, the load for the X-ray tube would be smaller or less time would be necessary for the acquisition of the image data. The image would then be made using the information from all the detectors. If the images were slightly overlapping, a software algorithm would have to be developed to integrate them into one image. By using 3 detectors the necessary flux or time would go down by a factor of 3.

The second problem arises from the fact that is very difficult to position the tile in the pressure box in such a way that the sensitive area of the strips starts just inside the window, while keeping the vertical distance between the window and the tile about 1–2 mm. The vertical distance has to be small, so that the resolution is not significantly affected by diffusion. Figure 6.11 shows an arrangement of the tile in a high pressure box. Even if the glass tile touches

the metal box, the layout of the strips at the end of tile is such that the sensitive area begins about 1 cm inside the window (see Figure 3.4). This is to avoid discharges at the ends of the strips. If the dead area of the gas extends to 1 cm, assuming xenon at 5 bar, we can calculate the absorbed fraction in this area using Equation 2.2. The absorption coefficient of xenon for 18 keV X-rays is about 28 cm^2/g. That means that 1 cm of xenon at 5 bat would absorb 56% of the X-ray photons limiting the quantum efficiency of the system to a maximum of 44%.

A possible way to reduce the X-ray absorption in the entrance of the detector would be to make the material which constitutes the entrance window thick enough to reach almost above the sensitive area of the microstrip tile (Figure 6.12). If the window is made from a material with a lower absorption coefficient than xenon at 5 bar, the absorption in the detector entrance will be lower and the quantum efficiency of the detector will be higher. Beryllium is a good candidate for window material, and 1 cm of beryllium will absorb only 30% of the X-ray photons. In this case care must be taken to keep the window at the right potential, because it will be very close to the strips and might cause discharges.

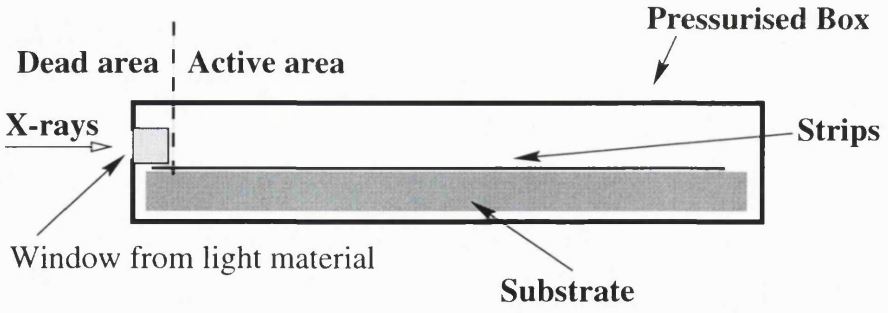

Figure 6.12: Schematic layout of the arrangement of an MSGC tile inside a pressure box with a thick window made of light material.

Chapter 7

Summary and Conclusions

Digital Radiography has advantages over conventional radiography, the most important being digital image processing, which can reveal details invisible in a single radiogram. Although it is possible to digitize film and then process the images, this approach is time consuming and restricted by the limitations of film as a detector. The use of detectors that provide digital image capture and have wide dynamic range is essential.

Experience with the Siberian Digital Radiographic Device has shown that gas detectors, MWPCs in particular, are suitable for digital radiology. It has also been shown that by using such a detector in counting mode, it is possible to produce images of high signal to noise ratio and reduce the dose needed for the examinations. Tests performed by the Department of Medical Physics and the High Energy Physics group (UCL) showed a dose reduction between 30 and 100 times compared to standard film/screen systems, depending on the clinical examination. The main disadvantage of the device is its spatial resolution of $\sim$0.5 mm, the limit for an MWPC, whereas film/screen systems achieve resolutions of 0.1–0.2 mm.

An MSGC is a detector that operates with the same principles as the MWPC

but offers five times better spatial resolution. It was developed as an improvement on the MWPC, it is being used on a number of current experiments including the HERMES experiment at HERA, and it is going to be used in the next generation of Particle Physics experiments (CMS).

Experiments at Novosibirsk showed that an Xe/CO_2 MSGC, at pressure of 5 bar or higher, has a resolution around 200 μm for 18 keV X-rays. This is the photon energy used for mammographic examinations. The fact that the breast image size is well within the current detector sizes and that mammography is a field where dose reduction is important made the detector an interesting candidate for breast imaging.

A Monte-Carlo simulation model, based on ITS 3.0, was developed to simulate the performance of MSGCs for X-ray detection. The model compared well with the results of the Novosibirsk experiments as well as with further tests done with an $Ar/iso\text{-}C_4H_{10}$ MSGC at atmospheric pressure. It was then used to predict the performance of a keystone MSGC as a prototype for mammography. The simulated tile had a pitch of 190 μm and parallel strips giving an equivalent resolution of a tapered tile with a pitch varying from 200 μm to 180 μm over 5 cm.

The results show that if the MSGC is filled with Xe/CO_2 at 5 bar the FWHM of the channel response, as a point source is scanned across it, is 280 μm if simple binary mode is used. If coincidence logic is used, and double hits are registered in separate channels, the FWHM of the channel response is below 150 μm. The pre-sampled LSF was calculated for the ST and HR modes and showed a FWHM of 190 and 150 μm respectively. The MTF was also calculated and showed a resolution of 4.5 and 6.5 mm^{-1} (at MTF = 0.1). Although the minimum requirement for a detector for mammography at the moment is 10 mm^{-1}, it is not out of the question that this could be achieved by future optimisation of gas pressure and strip pitch.

The potential advantages of a system based on an MSGC are high quantum efficiency, high signal to noise ratio and wide dynamic range. A system with these characteristics can make the best use of the available X-ray photons, reducing the necessary dose to the patient. Although the spatial resolution of such a system is slightly worse than the resolution of film/screen systems or possibly worse than systems based on CCDs, a system based on an MSGC could offer the same diagnostic value using lower doses than the other systems.

Appendix A

Input files for UPDATE and ITS

A.1 Input file for the UPDATE program

```
*IDENT,DEFINE
*DEFINE,VAX
*DEFINE,ACCEPT
*DEFINE,PCODES
*/ DEFINE,PLOTS
*DEFINE,RNG1
*/ THE FOLLOWING EXAMPLES OF PARAMETER MODIFICATION ARE USUALLY
*/ OPTIONAL, BUT MAY SIGNIFICANTLY REDUCE COMPUTER COSTS BY
*/ REDUCING MEMORY REQUIREMENTS.
*IDENT,PMOD
*/D,PARAMS.9
*/      PARAMETER ( INMT=2,     INEM=1,    INMAX=64,   NSURV=2775,
*/ INMAX UPDATE FOR USING CROSS SECTION SET WITH EXPANDED ELECTRON
*/ ENERGY GRID: THE PARAMETER INMAX IN THE MONTE CARLO CODE MUST BE
*/ EQUAL TO OR GREATER THAN THE VALUE OF NMAX IN THE UNIT IOUT
*/ OUTPUT OF THE CROSS SECTION GENERATOR.  EXPANDED ELECTRON ENERGY
*/ GRID IS NOT NEEDED IN THIS EXAMPLE WHERE THE SOURCE ELECTRON
*/ ENERGY IS 1.0 MeV AND THE GLOBAL ELECTRON CUTOFF ENERGY
*/ IS 0.05 MeV.
*D,PARAMS.9
       PARAMETER ( INMT=4,     INEM=4,    INMAX=60,   NSURV=2775,
*D,PARAMS.11,PARAMS.14
     $          INRANG=34,  INTANG=INMAX/4+1, INEEL=13,   INPEL=21,
     $          INEPS=9,         INGAS=1000,  INLAN=5000, INPPS=21,
     $          INLAMB=1591,     JAHSUB=51,   IJSPEC=5,  JATPR=698,
     $          JATAN=799,   INTAB=10,   IMTAX=150  )
*D,PARAMS.28,PARAMS.30
      PARAMETER ( IKMAX  =  7,   IJMAX  =  7,
```

```
     $            IKPMAX =  7,   IJPMAX =  7,
     $            INIZON  = 8,   INSZON =  11000)
*D,PARAMS.37
      PARAMETER ( IJSMAX = 1, IJFMAX =2,
*D,PARAMS.39,PARAMS.42
     $            IJFMXP = 2,          IJFMP1 = IJFMXP+1,
     $            IKFMAX = 2,          IKFMXP = 2,
     $            IKFMX1 = IKFMAX+1,   IKFMP1 = IKFMXP+1,
     $            INLF   = 55,          INLFP  = 55)
*D,PARAMS.81,PARAMS.82
     $  IFPD = 150,   INUMR = 7,   ITMA   = 300,   NAZ    =  7,
     $  IJTY =  7,   IARB  = 1,   NVIEWS =  7,   NCZONE = 50,
*/
*/ VOLUME DATA. ALL VOLUMES ARE THE SAME
*D,JOGEN.833,JOGEN.834
       DO I=1,10000
         VNOR(I)=1D-4
*B,JOGEN.835
       ENDDO
*D,PARAMS.21
       PARAMETER ( KPTMAX=15,             INSTAT=15,
*/
*/ DEFINE NEW OUTPUT FILE
*I,ITS.165
       OPEN(18,FILE='SCR$WEEK:XECO2_5BAR_mo_KEY.SIM',
     +STATUS='NEW')
*I,ITS.343
       CLOSE (18)
*/
*/ MODIFICATION OF THE OUTPUT SUBROUTINE. ZONES WITH NON-ZERO
*/ ENERGY ARE WRITTEN TO THE OUTPUT FILE. A FLAG IS INSERTED AT
*/ THE END OF EVERY EVENT
*I,OUTPUT.318
       NEXTEVENT=2999999
       DUMENERGY=0.0
       ICHECK=0
       DO I=1,10000
         XMYDUMMY=SNGL((DUMP(I,1)+DUMP(I,2)+DUMP(I,3))*1.0E6)
         IF (XMYDUMMY.NE.0.0) THEN
           WRITE(18,*)I,XMYDUMMY
           ICHECK=1
         ENDIF
       ENDDO
       IF (ICHECK.EQ.1) THEN
          WRITE(18,*)NEXTEVENT,DUMENERGY
       ENDIF
*/
```

```
*/ MODIFICATION OF THE POSITION OF THE SOURCE TO CREATE
*/ A PLANE OR A  SQUARE OF PHOTONS. SMALL GAPS CAN SIMULATED
*/ HIGH CONTRAST OBJECTS
*/D,HIST.209
*/ 1989      X = XSR-0.19+RAN(IRAN)*0.36
*/           IF ((X.GT.0.0945.AND.X.LT.0.0975).OR.(X.GT.0.199.AND.
*/     + X.LT.0.202).OR.(X.GT.0.307.AND.X.LT.0.310)) GOTO 1989
*/D,HIST.210
*/           Y = YSR+RAN(IRAN)*0.02
*/
*/
*/ STOP SOME OF THE DEFAULT OUTPUT
*D,JOGEN.849
C **    WRITE(IOUT,'(''   ZONE'', 10(3X,I5,4X))') (J,J=JS,JF)
*D,JOGEN.850
C **    WRITE(IOUT,'('' VOLUME'',10(1X,1PE10.3,1X))')
C **                                          (VNOR(J),J=JS,JF)
*D,OUTPUT.223
C **    CALL STATS(TEMP,ISIG,1)
*D,OUTPUT.338
C **    CALL STATS(TEMP,ISIG,1)
*D,OUTPUT.351
C **    CALL STATS(XONE,ISIG,NSH)
*D,OUTPUT.361
C **    CALL STATS(XONE,ISIG,NSH)
*D,OUTPUT.375
C **    CALL STATS(TEMP,ISIG,2)
*D,OUTPUT.406
C **    CALL STATS(TEMP,ISIG,NPUT)
*D,OUTPUT.437
C **    CALL STATS(TEMP,ISIG,4)
*/D,OUTPUT.514
*/C **  CALL STATS(TEMP,ISIG,NPUT)
*D,OUTPUT.566
C **    CALL STATS(TEMP,ISIG,NPUT)
*D,OUTPUT.622
C **    CALL STATS(TEMP,ISIG,1)
*D,FLUXO.111
C **    CALL STATS(TEMP,ISIG,NPUT)
*D,TABLE.56
C **    CALL STATS(TEMP,ISIG,NPUT)
*D,TABLIN.66
C **    CALL STATS(TEMP,ISIG,NPUT)
*D,TABLIN,89
C **    CALL STATS(TEMP,ISIG,NPUT)
*/D,OUTPUT.555
*/C **  WRITE(NPRT,2539) L,MAT(LBC),(TEMP(I),ISIG(I),I=1,NPUT)
```

```
*D,OUTPUT.478,OUTPUT.556
```

A.2 Input file for ITS

```
ECHO 1
TITLE
...20 KEV  XE/CO2  AT 5 BAR KEYSTONE
************************ GEOMETRY ***************************
GEOMETRY 2
* DON'T FORGET TO CHANGE THE VOLUMES IF YOU CHANGE ANY OF
*       THE FOLLOWING NUMBERS
  RPP   0.0  0.4  0.0  0.5  0.0  5.0
  RPP  -1.0  1.0  -1.0  1.0  -1.0  10.0
  END
 ZSUB001   +1
  100 100 1
 Z002   +2 -1
  END
* MATERIAL CUTOFF STRETCHING
 1
 0
************************ SOURCE ****************************
RANDOM-NUMBER
   0.188873598D+13
PHOTONS
SPECTRUM  4
   1.0 0.87 0.86 0.0
   0.0191 0.0189 0.0181 0.0179
CUTOFFS 0.001 0.001
POSITION 0.2  0.2  0.0001
* DEFAULT DIRECTION
DIRECTION 0.0 0.0
************************ OUTPUT OPTIONS ********************
*
************************ OTHER OPTIONS *********************
HISTORIES 10000
BATCHES 10000
*
```

Bibliography

[1] A.Oed *Nucl. Instr. Meth.* **A263** (1988) 351

[2] D.R. Dance *Medical Radiation Detectors* Institute of Physics Publishing, edited by N.F. Kember (1994) p. 57

[3] G. Charpak *CERN Courier* March 1997, p.15

[4] S.E. Baru, A.G. Khabakhpashev, I.R. Makarov, G.A. Savinov, L.I. Shekhtman and V.A. Sidorov *Nucl. Instr. and Meth.* **A238** (1985) 165

[5] S.E. Baru, A.G. Khabakhpashev and L.I. Shekhtman *Nucl. Instr. Meth.* **A283** (1989) 431

[6] E.A. Babichev, S.E. Baru, A.G. Khabakhpashev, G.M. Kolachev, G.A. Savinov, L.I. Shekhtman, V.A. Sidorov and A.I Volobuev *Nucl. Instr. Meth.* **A310** (1991) 449

[7] A. Martínez-Dávalos, R.D. Speller, J.A. Horrocks, D.J. Miller, S.E. Baru, A.G. Khabakhpashev, O.A. Ponomarev and L.I. Shekhtman *Phys. Med. Biol.* **38** (1993) pp 1419–1432

[8] A. Ahmed *J. Path.* **117** (1975) 247

[9] H.P. Chan, L.T. Niklason, D.M. Ikeda, K.L. Lam and D.D. Alder *Med. Phys.* **21** (1994) pp 1203–1211

[10] M. Freedman, D. Steller, H. Jafroudi, S.C. Benedict, R.A. Zuurbier, R. Katial, W. Hayes, Y.C. Wu, J.S. Liu, R. Steinman, W. Tohne and S.K. Mun *Proc. SPIE* **2432** (1995) pp 114–125

[11] N. Karssemeijer, J. Frieling and J. Hendricks *Investigative Radiology* **28** No 5 (1993) pp 413–419

[12] R. Birch, M. Marshall and G.M. Ardran *Catalogue of spectral data for diagnostic X-rays* (The Hospital Physicists Association: London) 1979

[13] H. Semat and J.R. Albright *Introduction to Atomic and Nuclear Physics* Chapman and Hall, London 1972

[14] F. Sauli *Principles of Operation of Multiwire Proportional and Drift Chambers* CERN Yellow Report 77-09.

[15] D.R. Lide *Handbook of Chemistry and Physics* CRC Press 1991

[16] C.D. Brogles, D.A. Thomas and S.K. Haynes *Phys. Rev.* **89** (1953) 715

[17] K. Kleinknecht *Detectors for particle radiation* Cambridge University Press 1990 p. 12

[18] E.J. Kobetich and R. Katz *Phys. Rev.* **170** (1968) 391

[19] K.H. Weber *Nucl. Intr. Meth.* **25** (1964) 261

[20] J.W. Haffner *Radiation and Shielding in Space* Academic Press, New York 1967

[21] R. Gilmore *Single Particle Detection and Measurement* Taylor & Francis London 1992

[22] W. van Roosbroeck *Phys. Rev.* **139** (1965) A1702

[23] P. Horowitz and W. Hill *The Art of Electronics* Cambridge University Press, 1980 p296

[24] W. Price *Nuclear Radiation Detection* McGraw-Hill, New York 1958

[25] G. Charpak, R. Bouclier, T. Bressani, J. Favier and Č. Zupančič *Nucl. Instr. Meth.* **62** (1968) 235

[26] L.I. Shekhtman *Nucl. Instr. Meth.* **A379** (1996) 380

[27] CMS Technical Proposal CERN/LHCC 94-38

[28] W. Blum and L. Rolandi *Particle Detection with Drift Chambers* Springer-Verlag 1993

[29] by Archana Sharma (CERN), personal communication.

[30] S. Biagi *Nucl. Instr. Meth.* **A283** (1989) 716

[31] G.D. Alkhazov, *Nucl. Instr. and Meth.* **89** (1970) 155

[32] W.R. Nelson, H. Hirayama and D.W.O. Rogers *The EGS4 Code System* Stanford Linear Accelerator Center Report SLAC-265 (1985)

[33] J.A. Halbleib, R.P. Kensek, T.A. Melhorn, G.D. Valdez, S.M. Seltzer and S.J. Berger *ITS Version 3.0: The Integrated TIGER Series of Coupled Electron/Photon Monte Carlo Transport Codes* SAND91-1634 (March 1992)

[34] J.A. Halbleib and R.P. Kensek *IEEE Transactions on Nuclear Science* **Vol 39, No 4** (1992) 1025

[35] W. Guber, J. Nagel, R. Goldstein, P.S. Mettelman and M.H. Kalos, MAGI-6701, Mathematical Applications Group, Inc., 1967

[36] S.M. Seltzer *Appl. Radiat. Isot.* Vol. 42, No. 10, (1991) pp 917-941

[37] Using the NORRAN subroutine from the CERN program library.

[38] S.E. Baru, V.V. Neustroev, A. Papanestis, G.A. Savinov and L.I. Shekhtman, *Proc. Inter. Workshop on Microstrip Gas Chambers* Lyon 1995, p 27

[39] W.H. Press and S.A. Teukolsky *Numerical Recipes in C*, second edition. Cambridge, 1994.

[40] R. Bellazzini and M.A. Spezziga *La Rivista del Nuovo Cimento* vol. 17, No 12 (1994) p 1

[41] F. Angelini, R. Bellazzini, T. Lomtadze, M.M. Massai, G. Spandre and M.R. Torquati, *Proc ECFA workshop for LHC* Aachen 1990, CERN 90-10 vol III p 222

[42] A. Papanestis, L.I. Shekhtman and D.J. Miller *Nucl. Instr. Meth.* **A392** (1997) p 120

[43] S.W. Snow, J.T. Baines, G.J. Crone, I.P Duerdoth, T.R. Edgecock, M. Edwards, M.J. Esten, R.L. English, M. Ibbotson, N. Lumb, T. McMahon, B.T. Payne, R.J. Thomson and J.A. Wilson *Proceedings of the International Workshop on Microstrip Gas Chambers* pp 127–134, Lyon 1995

[44] A Li Evans *The Evaluation of Medical Images* Adam Hilger 1981

[45] H. Fujita, D. Tsai, T. Itoh, K. Doi, J. Morishita, K. Ueda and A. Ohtsuka, *IEEE Transactions on Medical Imaging*, Vol. 11, No 1, (1992) p 34

[46] S.E. Reichenbach, S.K. Park and R. Narayanswamy, *Opt. Eng.* **30** (1991) 170

[47] Telephone communication with Siemens